Master thesis and internship[BR]- Master's Thesis : Robustness and Maintenance of Quasi-Satellite Orbits around Phobos[BR]- Internship (linked to master's thesis)

Auteur : García Mateas, Jose Carlos
Promoteur(s) : Kerschen, Gaetan
Faculté : Faculté des Sciences appliquées
Diplôme : Master en ingénieur civil en aérospatiale, à finalité spécialisée en "aerospace engineering"
Année académique : 2019-2020
URI/URL : http://hdl.handle.net/2268.2/8785

Robustness and Maintenance of Quasi-Satellite Orbits around Phobos

By

José Carlos García Mateas

Department of Aerospace and Mechanical Engineering

UNIVERSITÉ DE LIÈGE - FACULTÉ DES SCIENCES APPLIQUÉES

Graduation Studies conducted for obtaining the Master's degree in Aerospace Engineering by JOSÉ CARLOS GARCÍA MATEAS.

JUNE 2020

ABSTRACT

The Martian moons pose one of the many unanswered questions regarding the bodies found in the Solar System. In particular, the currently available data does not enable a complete understanding of the origin and composition of the moons. As a result, the Martian Moons eXploration mission (MMX) is currently being developed by the Japanese Space Agency *JAXA*, with the objective of landing in Phobos to retrieve a sample and bring it back to Earth. This would then provide scientists with information regarding the composition of the body and hence enable to determine whether Phobos is a captured asteroid or whether it formed through an accretion process.

In order for a probe to land, the spacecraft must first orbit the moon so as to determine the best landing location. Doing so presents a complicated problem due to the rich dynamical environment found, where gravitational perturbations from Mars, the irregular shape of Phobos or the Sun are found among others. Preliminary studies have been already performed to determine possible orbits suitable for the mission and, in particular, Quasi-Satellite Orbits (QSO's) have been found.

As a result, the objective of this thesis is to carry out an analysis of the effect that the perturbations would have on the evolution of these orbits. To that end, a high fidelity propagator has been developed for the Phobos environment, and the following perturbations have been taken into account: a complete spherical harmonic model (GMM3) for the Martian gravity, a polyhedral model for Phobos, solar radiation pressure and solar gravitational attraction.

In this thesis the reader will find the coordinate systems, equations of motion and perturbation models used to simulate the MMX orbit around Phobos. The results will show the effect that each of the perturbations considered has on a selected QSO.

DEDICATION AND ACKNOWLEDGEMENTS

This thesis is the last step in the journey that I started two years ago when I decided to study the master in Aerospace Engineering at Université de Liège. It has been a long time out of home but I am grateful for everything I have learned.

I would like to thank Dr.Gaëtan Kerschen for allowing me to do this thesis and the internship associated to it. Also, for his comprehension with me when my situation complicated. My gratitude also to Dr.Lamberto Dell'Elce, who not only proposed me the topic but most importantly helped me throughout the project. He has dedicated many hours to guiding the thesis while working in the McTAO team. Also, big thanks to Dr.Nicola Baresi for providing me with various data and MATLAB routines for the propagator developed.

As those close to me know, the last year has been specially hard and I would not have been able to reach this point without their help and support. I want to therefore express my huge gratitude to them, and even with these words I know it is not enough. To my friends Ana, Andrea, Bryan, Elias and Jorge for all your time, help, encouragement and good moments. Thank you Guzmán for always being there and willing to help me with whatever. Thank you Juan Manuel for being a brother, my second family here in Liège. You are all incredible people and I am very grateful to have you.

I cannot end up this dedication without mentioning the two most important people in my life. Thank you Mum and Dad for being an example for life. Thank you for your endless love, support and energy. You have made it possible. This work is for you.

TABLE OF CONTENTS

Part I

THE MARTIAN MOONS

INTRODUCTION

Context

Space has, since the appearance of the first civilizations in Mesopotamia, Persia and Greece, fascinated and intrigued mankind. This has caused that, throughout history, a large number of people have dedicated their lives to the study of the apparently inert sea that laid above their heads.

The beginners, with their basic equipment, first dedicated themselves to the study of what could be observed, that is, the stars, to discover new planets, to pose the first theories about planetary motion (Eratosthenes, Ptolemy), to calculate the Earth-Moon distance (Hipparcos) etc. Eventually, as the centuries passed, scientific progress was made and more sophisticated instruments were developed, with more and more discoveries about the Universe and its components being made.

However, it was not until approximately 75 years ago that the first technology to grant access to space was developed. In September 1944, the V2 rocket constructed by Germany became operative and started devastating London [12]. Although the objective was to destroy the enemy, it would later become the precursor of the launchers that enabled access to space. Since then, many missions have been conducted, and humans have been able to not only place hundreds of satellites into orbit but also to step on the Moon.

Despite the huge progress made, not only in discovering celestial bodies and their characteristics but also in understanding the physics that moves the Universe, plenty of unanswered questions still remain. One of them is posed by Phobos and Deimos, the two martian moons, since the current data available about these two bodies does not enable a complete understanding of their origin and characteristics.

As a result, the Japanese Space Agency, *JAXA*, is developing the so-called Martian Moons eXploration (*MMX*) mission, with the objective of sending a spacecraft to the martian system, so as to study the bodies and land on Phobos to perform in-situ experiments and collect samples to bring back to Earth.

1.1 The Martian System

Considering that the focus of this thesis is placed on Phobos and on the *MMX* mission, a brief review of the Martian system must be performed to provide some historical background as well as information regarding the characteristics of the three bodies that form part of it.

1.1.1 Mars

Mars is the fourth planet of the Solar System, as well as the furthest of the so-called telluric planets. Its name comes from the ancient Romans, who decided to call the planet after their god of war due to the reddish colour that the surface exhibits, which reminded them of the blood found on the battlefield [13]. No exact date is known for the discovery of this planet, although there are proofs which show that the Egyptians already kept track of it around 4000 years ago [13].

Apart from Earth, no other planet in the Solar System has been as intensely studied as Mars. Since humanity gained access to space, a fleet of orbiters and landers have been sent to the "Red Planet" with the objective of discovering its properties and characteristics, as well as with the idea of answering the question regarding life. The interest in Mars is such that, nowadays, up to six spacecraft from different space agencies are orbiting the planet, while two rovers are on the surface.

As a consequence of the present and past missions, most of the characteristics which define Mars are known. For instance, its axis of rotation is tilted approximately 25 ° with respect to its orbital plane, having therefore seasons just like on Earth. The structure and composition have also been studied, and hence it is now known that Mars has a core at its

center or that it is mainly made of nickel, sulfur and iron, being the oxidation of this last element the reason behind the red coloured surface that it has [13].

Other characteristics include an interesting topography, with many craters, channels and volcanoes, as well as "weather" conditions such as dust storms [13]. It is also known that temperature variations are severe, with values ranging from +20°C down to -153 °C. The planet also has a very thin atmosphere, in which carbon dioxide, argon and nitrogen are the main components [13]. A summary of the main Martian properties used in this thesis is found in Table 1.1 below.

R [km]	M [kg]	T_{rot} [days]	T_{orb} [years]
3389.50	6.4185 $\times 10^{23}$	1.02595675	1.8808476

Table 1.1: Physical data of Mars, where R represents the mean equatorial radius, T_{rot} is the sidereal rotation period and T_{orb} corresponds to the sidereal orbital period. Data taken from reference [1]

.

1.1.2   **Phobos** & **Deimos**

By the beginning of the 19th century, the Copernican model for the Solar System had been accepted, the so-called Galilean moons of Jupiter were known and the recently discovered planet Uranus had been found to have two moons [14]. By 1870, not only new satellites for Uranus and Saturn had been identified, but another planet (Neptune) had been discovered [14]. However, Mars continued to apparently have no satellites orbiting around it.

This fact was indeed in contradiction with the predictions carried out by the German astronomer Johannes Kepler in the 17th century, who had suggested that Mars would have two satellites [4]. As a result, astronomers and scientists of the time such as William Herschel or Heinrich Louis d'Arrest started searching [14]. However, it was not until August 12,1877 that Deimos was found by Asaph Hall, an American astronomer who worked at the U.S Naval Observatory. Six days later, Phobos was discovered.

The difficulty in finding the moons was due to the fact that both are located close to Mars, and hence had been hidden by the Martian glare [4]. The names for both moons were defined according to Greek mythology, in which Phobos and Deimos were two twin sons of Ares, the Greek counterpart for the Roman god of war Mars [14]. Images of these bodies can be seen in Figure 1.1 below.
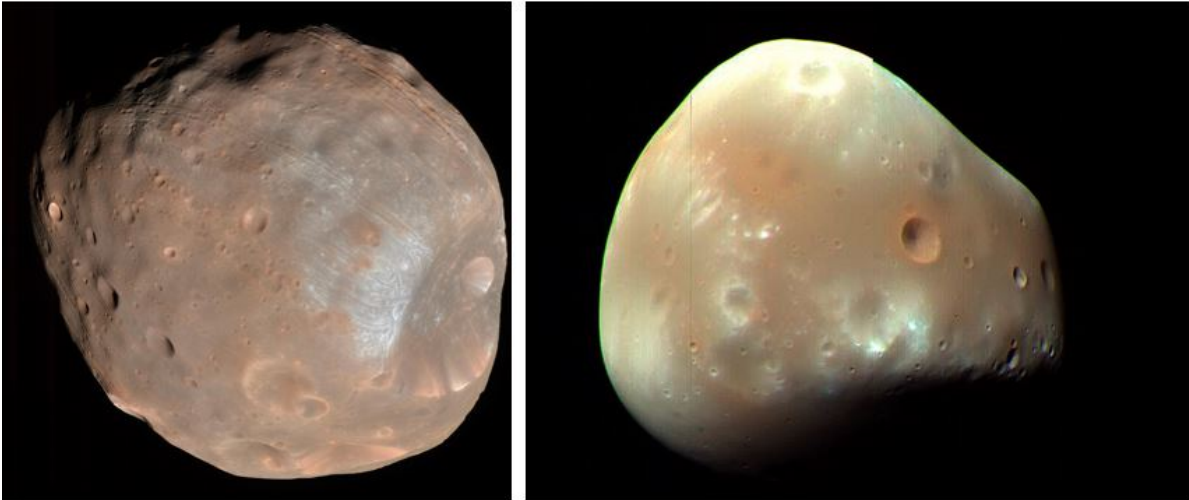
Figure 1.1: Images of Phobos (left) and Deimos (right) taken by the High Resolution Imaging Science Experiment (HiRISE) camera found in NASA's Mars Reconnaissance Orbiter [7].

As can be appreciated, both bodies are characterized by an irregular shape and by a highly cratered surface, specially in the case of Phobos. In Figure 1.1 the reader can observe, in the bottom-right corner of the image corresponding to Phobos, the so-called Stickney crater, a 9.7 km diameter feature whose debris is believed to be responsible for many of the smaller impacts that can be observed on the surface [15]. In the case of Deimos, the surface appears to be less cratered because it is thought that there is a dust/regolith layer covering it and hence filling the impacts [13].

With respect to the dimensions, both moons are amongst the smallest of the ones known in the Solar System, with Phobos being 7.24 times more massive than Deimos [4]. Furthermore, Phobos is the one closest to Mars and it is approximating the surface at a rate of 1.8 meters every century, implying that in 50 million years the moon will either impact Mars or disintegrate and form a ring due to the tidal forces [15]. Table 1.2 below presents the main characteristics of Phobos, which is the subject of the study conducted in this thesis. Values for Deimos are also provided as a comparison.

Parameter	Phobos	Deimos
Largest semi-major axis [km]	13.4	7.5
Intermediate semi-major axis [km]	11.2	6.1
Smallest semi-major axis [km]	9.2	5.2
Density [g/cm^3]	1.872	1.471
Mass [kg]	1.0659×10^{16}	1.4762×10^{15}
Orbital Period [hours]	7.650	30.298
Spin State	s	s

Table 1.2: Physical properties of the Martian moons. A spin s corresponds to a synchronous state, so that the rotational and orbital periods are the same. Data from [2] and [3].

1.1.3   Why are we interested in the Martian Moons?

As already mentioned, Phobos is the body in which the *MMX* mission will land to retrieve a sample which will then come back to Earth. Hence, it is also the subject of this thesis, since this is the moon around which orbits will be later analyzed. Nevertheless, the *MMX* mission will also study Deimos.

With this in mind, the reader may now wonder what are the reasons for scientists to be so interested in the Martian moons while there exist plenty of other celestial bodies to study. The justification behind is simple: the origin of the Martian moons is unclear. As will be seen in more detail in Chapter 2, there are different theories which try to explain the particularities of Phobos and Deimos, although all of the ideas revolve about two main concepts: either Phobos and Deimos are captured asteroids/bodies or were formed by accretion of particles from a disk.

Determining the origin of the moons as well as their evolution is important because this can provide information and answers to some of the questions posed in the *Planetary Science Decadal Survey*, which include [14]:

- What were the initial conditions, processes and stages involved in the formation of the Solar System?

- How did terrestrial planets receive a water supply?

- What were the first sources of organic matter that these planets received?

- What is the explanation behind the evolution of the surfaces of the small bodies?

For instance. if Phobos and Deimos are captured asteroids with compositions which include carbon and water, then both would be representative examples of the bodies that provided this two components to the planets during their formation processes, hence answering the second and third questions [14]. If, on the other hand, these bodies were two captured asteroids which did not have a rich carbon composition but rather were ordinary chondrites, then valuable information about the effects of space weathering on the surface would be obtained, since there is a current mismatch between known meteorites and the available D-type asteroid spectroscopy of Phobos [14].

Finally, the first question would be addressed if it is found that the moons were formed through an accretion process. Indeed, there is also the possibility that the origin and evolution of the two Martian moons is different and independent with respect to each other, in which case even more information would be obtained to answer the questions listed previously.

1.2   Previous missions to Phobos

The interest in the Martian moons, and in particular in Phobos, is not new. Prior to the *MMX* mission, other spacecraft have performed studies of the bodies or have failed while trying to do so. In this section, a brief review of some of these missions is presented.

In 1970, almost 93 years after the discovery of Phobos, the *Mariner 7* spacecraft took the first image of this moon. However, due to its poor quality, it was not until *Mariner 9* that the first surface features of the two Martian moons could be observed. Later in the decade, lower-altitude flybys were performed by the *Viking 1* and *Viking 2* spacecrafts, enabling the acquisition of valuable data which led to the discovery of the grooves in Phobos, the first mass estimations, the first spectroscopy studies and the first digital terrain model [16].

This exploration phase ended up with the decade, and it was not until 1988 that another spacecraft was sent to the Martian moons. In this case, it was the Soviet *Phobos 1* and *Phobos 2* missions the ones involved, which were planned to orbit Mars and deposit a lander on the moon. However, this project faced many problems, since *Phobos 1* was lost during its journey to the "Red Planet" and the second spacecraft failed three months after entering into its Martian orbit [16]. Despite its short lifetime, this second orbiter was able to perform three encounters with Phobos, and the data retrieved would yield the most accurate estimate of the density up to that date [14].

After 1988, several attempts were made to reach Mars and its moons with missions such as NASA's *Mars Observer* or the Russian *Mars 94*, although both failed. Eventually, in 1996 NASA's *Mars Pathfinder* was able to perform new measurements and confirm several spectral characteristics of the moons [14]. In any case, it would not be until the missions *Mars Express* from ESA (2004) and *Mars Reconnaissance Orbiter* (2005) from NASA that the knowledge about the Martian moons, and in particular Phobos, was revolutionized, with values from these orbiters defining the currently known composition data [14].

The most recent attempt to deepen the understanding of the Martian moons has been the so-called *Phobos-Grunt* mission, a project which formed part of the Russian Federal Space Program and in which China also collaborated. The objectives of the mission were almost identical to the ones pursued by the previous *Phobos 2*, being the return of a sample to Earth the ultimate one [17]. The mission was launched in November 2011 but failed to enter its interplanetary trajectory, re-entering Earth on January 2012 [18]. A summary of the missions and their main outputs is presented in Table 1.3 below.

Mission	Agency & Launch Date	Output	Status
Mariner's 7 & 9	NASA 1970 & 71	Surface features observed	Deactivated
Viking's 1 & 2	NASA 1976	Grooves, mass, spectroscopy	Deactivated
Phobos 1 & 2	Rosaviakosmos 1988	Density	Failed
Mars Observer	NASA 1992	-	Failed
Mars 94	Roscosmos 1996	-	Failed
Mars Express	ESA 2003	High resolution images, spectroscopy	Active
Mars Reconaissance Orbiter	NASA 2005	High resolution images	Active
Phobos - Grunt	Roscosmos 2011	-	Failed

Table 1.3: Summary of the missions which have studied the Martian moons, including main discoveries and current status [4].

1.3 Current Initiative: MMX

After having reviewed the past missions to the Martian moons two things have become clear: the data available has been provided by Martian orbiters or by flyby missions and all of the spacecraft which specifically targeted Phobos have failed. With this preamble, the future of the exploration of the Martian moons relies on the *MMX* mission. This section will therefore provide a brief review of the objectives and spacecraft characteristics.

1.3.1 Objectives & Timeline

The *MMX* mission has different scientific and engineering objectives. With respect to the former, the mission aims to perform the studies which would provide sufficient data to answer the questions presented previously in Section 1.1.3. A sample analysis would indeed determine the origin of the moon, which in turn could explain the transport of water and organic compounds, the primordial composition of Mars, the evolution of the surfaces of the moons or the atmospheric processes in Mars [19].

On the other hand, from the engineering point of view, the mission aims to develop and test new technologies which will shape the future exploration missions conducted by the Japanese Space Agency, JAXA. For instance, *MMX* will use one of the most complicated and advanced chemical propulsion system ever designed. Similarly, the complete sample retrieval technology will be redesigned, since the objective of achieving a 10 kg sample requires a system with a higher performance than the one used in previous missions such as *Hayabusa* and *Hayabusa II* [19].

With respect to the mission timeline, launch is planned for 2024, followed by a one year outbound flight to Mars, with insertion into quasi-satellites orbits around the moon occurring in 2025. Observations will then be performed for an estimated 3 year period, although the actual duration of this phase will depend on the on-going measurements. During this period, the sample will be retrieved. Finally, the inbound flight to Earth would take place, with arrival being expected by 2029 [5]. An schematic representation of the *MMX* timeline is shown in Figure 1.2 below.

MMX MISSION TIMELINE

September 2024	August 2025	2025 - 2028	August 2028	July 2029
Earth Launch	Mars Orbit Insertion	Quasi Satellite Orbits around Phobos	Departure from Martian system	Earth Arrival
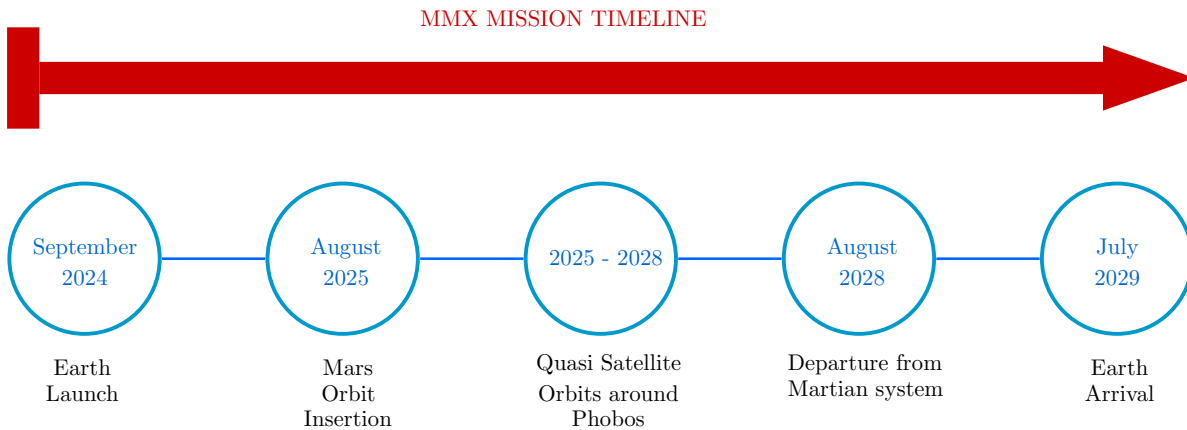
Figure 1.2: Schematic representation of the different mission phases and the corresponding planned dates.

1.3.2 Spacecraft characteristics

Although the *MMX* spacecraft is still being designed and hence undergoes modifications with each iteration of the design process, the overall structure, mass properties and characteristics are already bounded and known. This section will therefore provide a brief review of these values.

To begin with, the *MMX* probe consists of two major components: the propulsion module and the so-called return module. The prior corresponds to the one responsible for the acceleration/deceleration of the spacecraft as well as for attitude control, while the later is the part of the spacecraft in which the main subsystems such as the sampler, the AOCS [1] or the instruments are located.

Although the type of engine has not been yet determined, it has been decided that the spacecraft will use chemical propulsion, with the propellant being a mixture of a fuel (to be defined) and oxygen. Since the propellant tanks are heavy and the *MMX* mission will carry the greatest amount of propellant of the Japanese missions up to date, spherical tanks have been selected and placed around a conical main frame [8].

With respect to the return module, it will be equipped with a rigid structure and a landing gear to withstand the impact with the surface of Phobos, which is estimated to produce a force of up to 0.3 G [2] [8]. As for the instruments on-board, the spacecraft will have the

---

[1] Attitude and Orbit Control Subsystem
[2] 1 G corresponds to Earth's gravity at its surface

following [20]:

- TENGOO, which stands for "TElescopic Nadir imager for GeOmOrphology" and is a camera intended to take images of the Phobos surface.

- OROCHI, which corresponds to "Optical RadiOmeter composed of CHromatic Imagers" and is a camera to observe the topography and composition of the surface.

- LIDAR, that stands for "Light Detection And Ranging" and which aims to studying the shape of Phobos.

- MacrOmega, which stands for "Macroscopique Observatoire pour la Minéralogie, l'Eau, le Glaces et l'Activité (Observatory for Mineralogy, Water, Ice and Activity)", a near infrared observation instrument developed by the French CNES.

- MEGANE, which stands for "Mars-moon Exploration with GAmma rays and NEutrons" and aims to determine the elements forming the moon.

- CMDM, the "Circum-Martian Dust Monitor", that aims at studying the environment around Phobos.

- MSA, a "Mass Spectrum Analyzer" to study the ion environment around Phobos.

With respect to the mass properties, the reader can find in Table 1.4 the distribution between the two modules. Finally, Figure 1.3 presents the design of the *MMX* spacecraft as it is nowadays, with some of the components mentioned previously identified.

Launch Mass [kg]	Return Module [kg]	Propulsion Module [kg]
3400	1500	1900

Table 1.4: Mass properties for the *MMX* spacecraft [5].
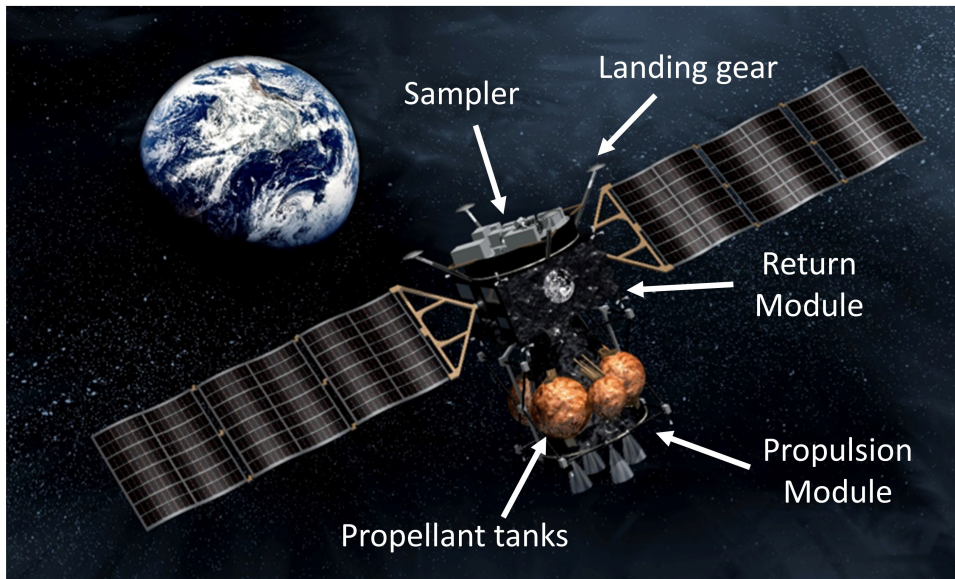
Figure 1.3: CAD model of the actual design of *MMX*, with several components labelled. Original image from [8].

PHOBOS

As has been mentioned in Chapter 1, the Martian moons present several unanswered questions which the mission *MMX* will try to address by performing observations of both moons and retrieving a sample from Phobos. This chapter therefore aims to deepen the understanding of the reader in the "why" behind the Martian Moons eXploration mission by presenting and explaining the mysteries surrounding the formation and evolution of Phobos, being the ideas also applicable to Deimos.

2.1 The capture scenario

While the Earth's moon has a rounded shape, Phobos is characterized by having an irregular morphology. In addition, the albedo, that is, the amount of radiation that the surface reflects with respect to the radiation it receives, is only of a few percent. As was mentioned in Chapter 1 the surface is heavily cratered and has grooves and, according to the crater counter technique, Phobos would be at least 1 billion years old, although this estimate is believed to not be precise since many of the craters on the surface appear to have been caused by ejected parts resulting from the impact that originated the Stickney crater [9].

With respect to the composition of Phobos, observations were performed by the spacecrafts mentioned in Table 1.3 in the visible and near-infrared wavelengths, and contradictory results were achieved. On the one hand, the reflectance spectra measured by *Viking-1* was found to resemble that of a C-type carbonaceous asteroid such as the ones found in the

main asteroid belt [9]. On the other hand, measurements from *Phobos 2* and *Hubble Space Telescope* present greater accordance with the spectra of carbonaceous D or T-type asteroids, which are found in the outer belt and in the Trojans around Jupiter respectively [9].

As a consequence of this characteristics, scientists have proposed that Phobos and Deimos are asteroids which were captured by Mars. Determining which type of asteroid (either C,D or T) is of importance since the last two represent asteroids which are believed to have been formed in the outer region of the Solar System and then moved inwards. If this was the case, Phobos would indeed provide valuable information for dynamical models of the primitive Solar System.

2.1.1 The ambiguities of the capture scenario

Although there are reasons to believe that Phobos is a captured asteroid, this scenario also presents some characteristics which have not yet been explained. To begin with, although the reflectance spectra from *Viking 1* partially matches the one obtained from C-type asteroids, the truth is that there is no coincidence with any low-albedo carbonaceous meteoritic samples available on Earth [9]. In addition, a similar problem appears with the Tagish Lake meteorite, which is believed to be an example of a D-type asteroid. A comparison between the spectra of Phobos and of this sample matches almost perfectly except for the existence of a 3 μm absorption band [9].

With the objective of explaining these differences, scientists have proposed that the surface of Phobos has undergone significant space weathering effects, which, if true, would provide valuable information to understand this phenomena. On the other hand, another possibility is that there are no current meteoritic samples of the type of material that forms the moon.

A similar situation is found when analyzing the density and the internal composition of Phobos. Measurements from the *Mars Express* spacecraft have improved the density estimations of the moon, but, as can be appreciated in Figure 2.1 below, the mismatch with the meteoritic analogs is still existing. In addition, a considerable amount of porosity is expected to be present, since this is the only reasonable explanation to account for the low density presented by Phobos. Nevertheless, such porosity also introduces an uncertainty, since a low density value would better correspond to material that has undergone an accretion process rather than to a solid monolithic body [9].
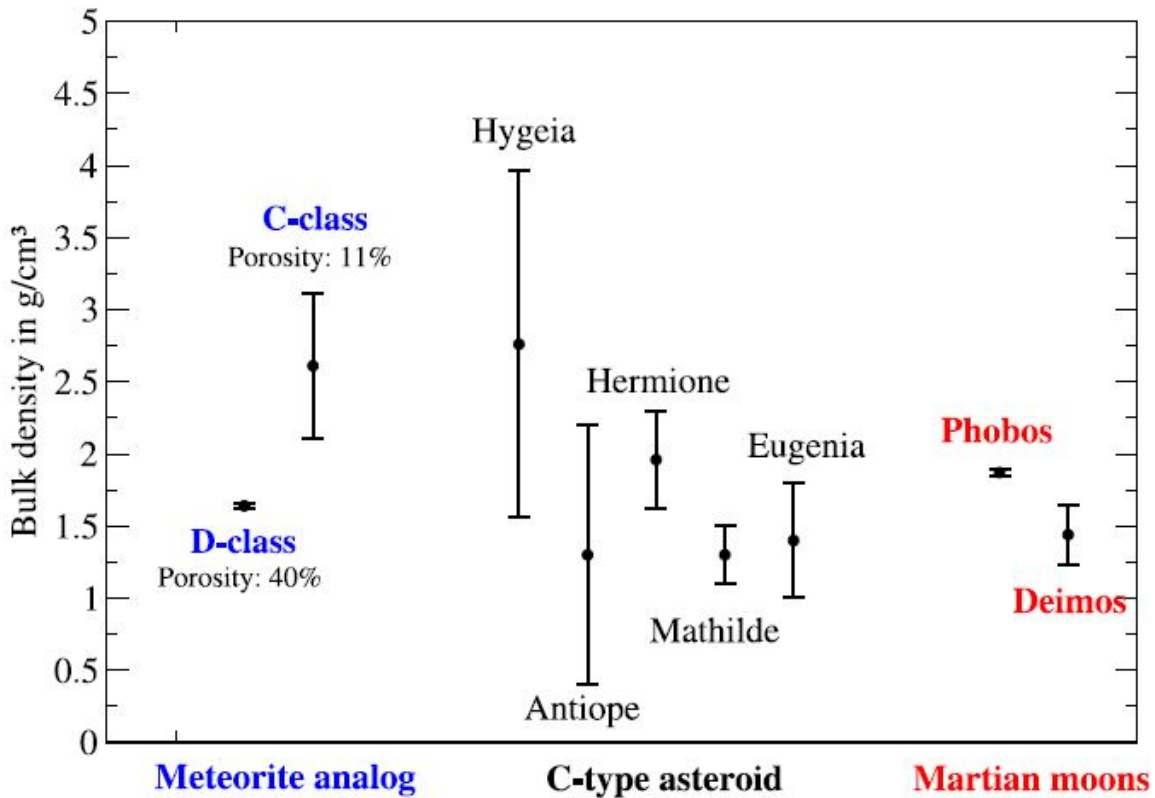
Figure 2.1: Comparison of the density of Phobos and Deimos with several asteroids and meteoritic samples. Graph from [9].

Further doubts in the capture scenario are raised by the orbital characteristics. In particular, Phobos exhibits a near-circular and near-equatorial orbit as well as a secular acceleration which causes the moon to drift towards the Martian surface at an approximate rate of 20 cm per year [9]. This raises controversy because a captured asteroid would initially have an orbit with a high eccentricity in an almost heliocentric plane, meaning that Phobos would have had to experience a circularization and change of inclination process which current models struggle to explain.

2.2 The in-situ formation scenario

As a consequence of the ambiguities presented by the capture scenario, several studies have presented models suggesting that Phobos was formed in orbit around Mars.

In particular, one model suggests that Phobos and Deimos are the remains of a larger moon which disintegrated when it entered into the Roche limit (found at 2.5 Martian radiuses). This would explain the orbital characteristics, since the circularization and change of inclination process would be easier in the case of a large captured body, and the carbonaceous composition can be explained if it is assumed that the "parent" moon had it. In any case, a challenge is raised in this model by the current position of Deimos, which is too far away (4 Martian radiuses) from the Roche limit [1] and makes it difficult to explain how could remains from the larger moon reach that current position [9].

On the other hand, a second model proposes that Phobos was formed by the accretion of debris resulting from an impact between Mars and another body of approximately the size of Ceres or Vesta. Such impact would have generated a disk around Mars from which the moon would have been born. With this theory, the near-equatorial and near-circular orbit of Phobos would be explained, and the carbonaceous composition of the moon would be justified if it is assumed that the impactor body was of this same composition [21]. The challenge raised in this scenario is once again the formation of Deimos, which would imply that the disk extended outwards a long distance.

Finally, some authors have suggested that Phobos formed from debris left after the formation of Mars. Such idea does indeed explain the orbital characteristics of the Martian moons, but it implies that the composition of the moons would be similar to that of Mars, and this is something which does not agree with the carbonaceous compositions that the moons have [9].

---

[1]The Roche limit is the distance at which a body, held up together by its own gravitational force, would disintegrate due to gravity forces exerted by a second body.

3

PROJECT DESCRIPTION

3.1 Project Objectives

In the previous chapters the reader has been able to gain insight into the characteristics of the Martian moons. As has been explained, understanding the origin and evolution of Phobos presents an interesting challenge and the only way in which the uncertainties can be solved is by means of a robotic mission. To that end, the Japanese Space Agency is developing the Martian Moons eXploration mission (*MMX*), which is planned to be launched in 2024.

The objective of this project is therefore to develop a high fidelity propagator for the *MMX* spacecraft. In particular, the aim is placed on studying the effect that perturbations have on the Quasi-Satellite Orbits (QSO) which have already been selected from the preliminary design phase of the mission. Previous work by Zamaro showed, as can be seen in Figure 3.1, that the main perturbations in the vicinity of Phobos are the gravity harmonics of Mars and Phobos, the eccentricity of the moon's orbit and its angular velocity, with radiation pressures and third body gravities playing a less relevant role.
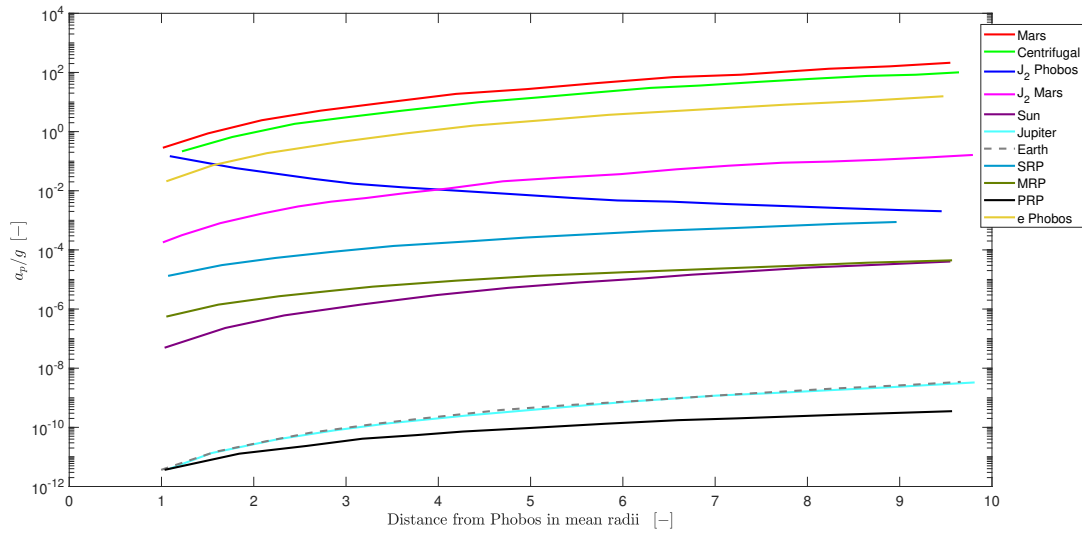
Figure 3.1: Differential analysis of the perturbations being found in the Phobos environment, where a_p is the magnitude of the perturbing acceleration and is shown divided by g, which is the magnitude of Phobos's keplerian gravity acceleration at that point. Graph reproduced from the study conducted by Zamaro, found in reference [10].

Therefore, to study the motion of the MMX spacecraft the propagator is developed so as to consider the perturbations due to the non-uniform gravity of Mars and Phobos, the solar radiation pressure and the third body attraction of the Sun. An analysis is performed with the objective of determining the effect of these accelerations on the spacecraft orbit and special focus is placed in the implementation of precise models for the gravities caused by the two bodies. In particular, Martian gravity is modeled using spherical harmonics by means of NASA's Goddard Mars Model 3 (*GMM3*) and the gravity of Phobos is introduced by considering a constant density polyhedron.

3.2 Thesis Structure

To fulfill the objectives described in the previous section this thesis has been structured into three different parts: an introduction to the Martian moons, methodology and description of the propagator and, finally, results and conclusion.

The first part, which finishes with this chapter, has been devoted to presenting the Martian system particularities and history, the mysteries and challenges raised by both moons and the objectives and characteristics of the *MMX* mission.

The second part of this thesis will be focused on explaining coordinate systems, equations of motion and models used in the propagator for the analysis of the MMX trajectory. In particular, reference frames are defined, equations of relative motion are derived for the perturbed case being considered and all the perturbation models are explained. The second part ends up with a thorough validation of the propagator developed, which uses several test cases such as the circular and elliptical three body problems to verify its correct implementation.

Finally, the last section of this thesis will present the results obtained. A detailed analysis will be made of the impact of the perturbations in a low-altitude Quasi-Satellite Orbit and this will be followed by the concluding remarks of the project.

Part II

METHODOLOGY AND SOFTWARE DESCRIPTION

COORDINATE SYSTEMS

As has been explained in Chapter 3, the aim of this thesis is to develop an orbital propagator for Phobos and the *MMX* spacecraft so as to study the effect that several perturbations would have on the Quasi-Satellite Orbits. Solving the problem presented requires the use of coordinate systems with respect to which the positions, velocities and accelerations will be defined. In particular, the topic on coordinate systems for Astrodynamics is complex, since there exists a wide variety of options that can be used and selecting the most appropriate ones is not always simple.

The situation is further complicated when taking into account the perturbations defined later in Chapter 6 since, for instance, solar radiation pressure and solar third body attraction are caused by a body which does not belong to the Martian system. In addition, in the case of the gravity acceleration caused by Phobos, the polyhedron model requires the position vector to be expressed in the principal axes directions, complicating the problem further. As a result, this chapter will first present the basic information regarding coordinate systems so as to then define the reference frames and the rotation matrices being used in the propagator.

Please note that for this chapter and the ones that follow, vectors will be denoted with a superscript arrow ($\vec{a}$), vector norms will be written as $||\vec{a}||$ and unit vectors will be specified by means of a superscript hat ($\hat{x}$). In addition, a rotation matrix from frame A to frame B will be expressed as $[R]_A^B$.

4.1 Basic Definitions

In general, a coordinate system is just a way of expressing the position and motion of bodies in three dimensional space. For these systems to be defined, three characteristics have to be specified: the frame, the center and the type of coordinates. The information explained below is based on the notation and concepts used in reference [22].

4.1.1 Frames

Coordinate frames refer to a set of Cartesian axes that are specified by four other characteristics, which are:

- Reference Body
  It can be any body in the solar system. Furthermore, the definition of the reference body does not necessarily imply that the center of the frame is also found in that body. For instance, as will be seen later, one can have an Earth equator frame that is centered at the Sun.

- Reference Plane
  The reference plane defines the X-Y plane of the frame. In general, such plane will be defined by the Z-axis, since it is perpendicular to it. Hence, if the reference plane is considered to be the equator plane of the body, then the Z-axis will correspond with the axis of rotation of the body. If, on the other hand, the reference plane is considered to be the orbital plane, then the Z-axis will be parallel to the vector of the orbital angular momentum.

- Reference Direction
  It is the direction in which the X-axis of the coordinate frame points. In general, two main cases are considered: either the X-axis points in the direction of the line of nodes produced by the intersection of two orbital planes, or, if the frame has a body-fixed X-axis that rotates with the body, then it points in the direction of the intersection between the Prime Meridian of the body and its equator plane.

- Reference Time
  Specifying a reference time is required since, in general, the reference planes experience motion conditions due to the existence of perturbations. Similarly to what happens with Earth, the Mars orbital plane is affected by the gravity perturbations

23

of other bodies in the solar system, leading to what is known as *planetary precession*. In addition, the equator of Mars experiences what is known as *lunisolar precession* due to the effect of the torque generated by the Sun and the Martian satellites on the equatorial bulge [23]. The addition of *planetary precession* and *lunisolar precession* yields what is known as *general precession*, which is a long period motion. On the other hand, the pole of Mars also undergoes a short period oscillation known as *nutation*. As a result, when both precession and nutation are taken into account, the *true* motion of the reference plane is represented. On the other hand, if only precession is considered then the *mean* motion of the plane is described.

To define an inertial reference frame, what is usually done is to consider a mean reference plane and take a snapshot at a particular time, being this time known as the *epoch*. The standard epoch corresponds to the 1st of January of 2000 at 12:00:00 ET, and is commonly referred to as the J2000 epoch. For the case of non-inertial frames, the reference time that is considered for the definition of the axes is the time at which the position, velocities and accelerations are defined. When this is the case, the notation *of date* is used [22].

4.1.2   Center and Type of Coordinates

The second element that defines a coordinate system is the center, that is, the location of the origin. There is a wide variety of possible locations, including any body in the solar system, planet system barycenters, locations at the surface of a body or even at the spacecraft itself.

Finally, the last variable that has to be defined in order to fully characterize a coordinate system is the type of coordinates that it employs to express the state vectors of the bodies and spacecrafts. In general, the most frequently used are Cartesian coordinates, characterized by the typical X,Y,Z axes and which are very useful for the numerical integration of the trajectories, or Spherical coordinates, in which the position is given by means of a distance and two angles, typically known as right ascension and declination or as latitude and longitude [22].

4.2   Heliocentric Coordinate Systems

Having defined the basic concepts related to the definition of coordinate systems and reference frames, it is now turn to explain which ones are used in the MMX High Fidelity

propagator. To begin with, the two heliocentric frames and the rotation matrices used to transform vectors between them are presented.

4.2.1 Sun Centered Earth Mean Equator and Equinox of J2000

The Sun Centered Earth Mean Equator and Equinox of the J2000 epoch, commonly denoted as EME2000, is an inertial reference system based on a right-handed X,Y,Z Cartesian set of vectors. In particular, the X-axis (X_{EME}) points in the direction of the vernal equinox of the mean orbit of Earth at J2000, the Z-axis (Z_{EME}) is normal to the mean equator of the Earth at J2000 and the Y-axis completes the triad [22].

In the propagator, this coordinate system is used in order to obtain the direction of the Mars pole and of the IAU vector, since the equations provided by the International Astronomical Union are expressed with respect to the EME2000 reference frame.

4.2.2 Sun Centered Ecliptic and Mean Equinox of J2000

The Sun Centered Ecliptic and Mean Equinox of Epoch J2000 is another inertial coordinate system used in the propagator. As indicated by its name, it is a right-handed Cartesian set of vectors centered at the Sun and oriented such that the X-axis (X_I) points in the direction of the vernal equinox of the Earth's mean orbit at J2000, the Z-axis (Z_I) is perpendicular to the ecliptic plane and the Y-axis (Y_I) completes the triad [22].

This coordinate system is used in the MMX High Fidelity propagator to describe the orbit that Mars has around the Sun, as this is required in order to be able to model the solar radiation pressure and the third body gravitational attraction exerted by the Sun on the MMX spacecraft. Taking into account that this system and the EME2000 frame share the same X-axis, the transformation of coordinates from one frame to another can be carried out by means of a simple rotation through the obliquity ϵ of the ecliptic. Hence, the transformation from coordinates in this frame to coordinates in the EME2000 is given by

$$[R]_I^{EME} = \begin{bmatrix} 1 & 0 & 0 \\ 0 & \cos\epsilon & -\sin\epsilon \\ 0 & \sin\epsilon & \cos\epsilon \end{bmatrix} \tag{4.1}$$

where the obliquity of the ecliptic at the J2000 epoch is equal to $\epsilon = 23.4392794444444°$ according to the *Astronomical Almanac* [24].

4.2.3   Heliocentric Perifocal frame

Describing the orbit of Mars around the Sun can be easily done by means of the so-called heliocentric perifocal frame, which is no other than a Cartesian frame centered at the focus of the orbit and with the X-Y plane corresponding to the orbital plane. The X-axis (X_P) is directed along the apse line, that is, from the focus to the periapsis of the orbit, while the Z-axis (Z_P) is perpendicular to the orbital angular momentum vector and the Y-axis (Y_P) forms a 90° true anomaly angle with the X-axis.

The main functionality of this frame is to enable a rapid computation of the Mars-Sun distance, since this can be done using the orbit equation. The transformation from the heliocentric perifocal frame P to the Sun centered ecliptic and Mean Equinox of J2000 can be done using the following matrix, where i, Ω and ω are the heliocentric inclination, right ascension of the ascending node and argument of perigee of Mars, respectively.

$$[R]_P^I = \begin{bmatrix} -\sin\Omega\cos i\sin\omega + \cos\Omega\cos\omega & -\sin\Omega\cos i\cos\omega - \cos\Omega\sin\omega & \sin\Omega\sin i \\ \cos\Omega\cos i\sin\omega + \sin\Omega\cos\omega & \cos\Omega\cos i\cos\omega - \sin\Omega\sin\omega & -\cos\Omega\sin i \\ \sin i\sin\omega & \sin i\cos\omega & \cos i \end{bmatrix} \tag{4.2}$$

4.3   Coordinate Systems for the Mars-Phobos environment

After having introduced the coordinate systems being used to describe the orbit of Mars around the Sun, it is now time to characterize the coordinate systems used for the orbit of Phobos around Mars and for the orbit of the spacecraft around Phobos.

4.3.1   Mars-Centered Mars Mean Equator and IAU-vector of Date

The Mars-centered Mars Mean Equator and IAU-vector of Date is a coordinate system centered in Mars in which the reference plane is the Mars mean equator of date and the reference direction is the IAU vector of date. Under a strict definition, this frame is not inertial since it accounts for the precession of Mars. However, since precession is a long period motion, it is considered as a pseudo-inertial frame, being this the reason why it is commonly known as the Mars Centered Inertial (MCI) frame.

26

In this frame, the X-axis (X_{MCI}) points in the direction of the IAU vector, which is defined as the intersection of the Mars Mean Equator of Date and the Earth Mean Equator of J2000, being positive in the direction of the ascending node. The Z-axis points in the direction of the Martian North pole (hence perpendicular to the equator plane) and the Y-axis completes the right-handed system [22]. It is the reference frame in which the orbit of Phobos is propagated, and is therefore used to express the Cartesian position and velocity of the moon.

This frame can be related to the EME2000 reference frame (*EME*) by means of the right ascension α_0 and declination δ_0 of the north pole, which can be obtained using the equations provided by the IAU in reference [25], which are

$$
\begin{aligned}
\alpha_0 &= 317.68143 - 0.1061\,T \\
\delta_0 &= 52.88650 - 0.0609\,T
\end{aligned}
\tag{4.3}
$$

where T represents the interval in Julian centuries (of 365.25 days) from the standard epoch (J2000). The rotation matrix from *EME* to *MCI* can then be defined as:

$$
[R]_{EME}^{MCI} =
\begin{bmatrix}
-\sin\alpha_0 & \cos\alpha_0 & 0 \\
-\cos\alpha_0\sin\delta_0 & -\sin\alpha_0\sin\delta_0 & \cos\delta_0 \\
\cos\alpha_0\cos\delta_0 & \sin\alpha_0\cos\delta_0 & \sin\delta_0
\end{bmatrix}
\tag{4.4}
$$

4.3.2 Mars-Centered Mars Mean Equator and Prime Meridian of Date

This is a rotating (hence non-inertial) coordinate system that is centered in and fixed with Mars. In particular, the reference plane is the Mars mean equator, while the reference direction in which the X-axis points corresponds to the direction of the Martian Prime Meridian, which is defined to be the Airy-0 crater. The Z-axis is parallel to the Martian rotation axis and the Y-axis completes the right-handed set [22].

It is also known as the Mars Centered Mars Fixed (MCMF) frame and in the propagator it is used to compute the gravity accelerations caused by Mars on both Phobos and *MMX*. Since the Z-axis is parallel to that of the MCI frame, the orientation of the X-Y axes is specified by a rotation defined by the angle W, which is the angle measured along the equator from the IAU-vector to the point where the Prime Meridian intersects the equator. A graphical representation of the relation between both frames can be seen in Figure 4.1.
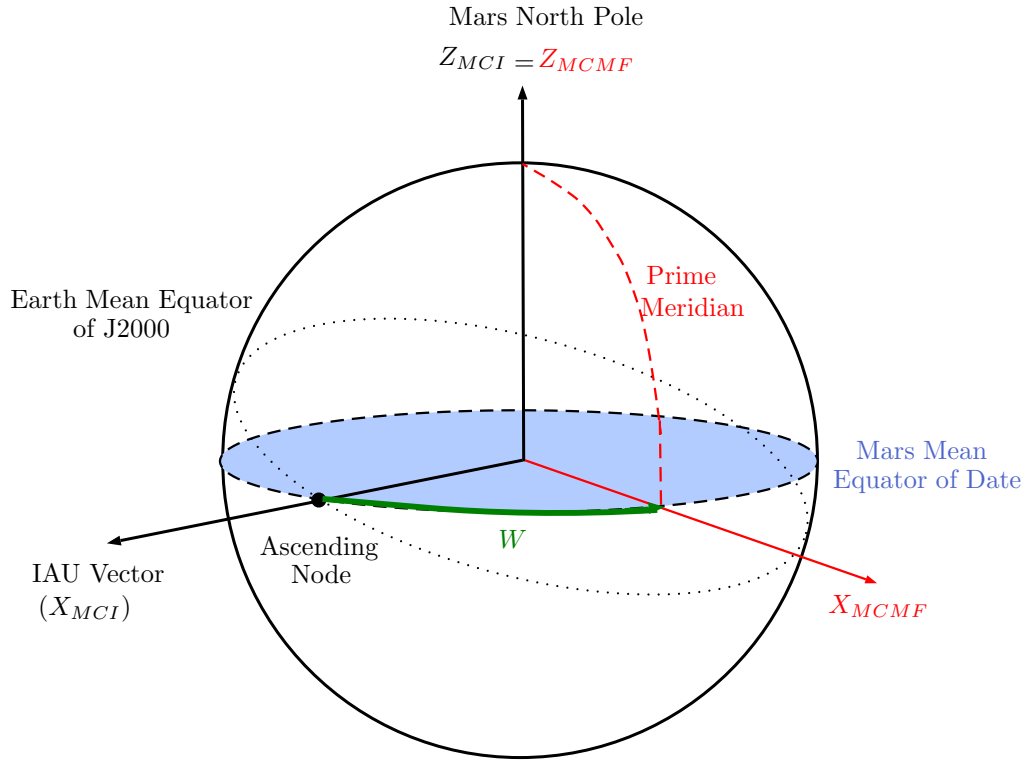
Figure 4.1: Representation of the Mars Centered Inertial (in black) and Mars Centered Mars Fixed frames (in red). The angle W is shown in green.

Computing the value of W can be done by means of Equation 4.5 below, where d represents the time interval in days from the standard epoch, which corresponds to 2000 January 1, 12 hours Barycentric Dynamical Time (TDB). In Equation 4.5, the first term to the right of the equal corresponds to the angle at the reference epoch while 350.89198226 is the angular velocity of Mars in degrees per day.

$$W = 176.630 + 350.89198226\, d \qquad (4.5)$$

Once the angle has been defined, the rotation matrix which enables the transformation from MCI to MCMF is given by Equation 4.6, being the transformation from MCMF to MCI performed with the transpose:

$$R_{MCI}^{MCMF} = \begin{bmatrix} \cos W & \sin W & 0 \\ -\sin W & \cos W & 0 \\ 0 & 0 & 1 \end{bmatrix} \tag{4.6}$$

4.3.3 Phobos Centered Phobos Fixed

The Phobos Centered Phobos Fixed coordinate system (PCPF) is similar to the previously described MCMF, but in this case defined for Phobos following the IAU convention. As a result, it is characterized by having the origin at the barycenter of Phobos, the Z-axis parallel to the spin axis of the moon, the X-axis pointing in the direction of its Prime Meridian and the Y-axis completing the righ-handed system. According to the IAU criteria, the Prime Meridian of Phobos is defined as the point which always points towards Mars on the moon's equator. As will be explained in Chapter 6, it is used as the substitute of the Principal Axes frame, which is required in order to retrieve the gravitational acceleration caused by the moon using the polyhedron model.

4.4 Local Vertical Local Horizontal frame

As the reader will see in Chapter 5, the equations of relative motion are usually expressed in the so-called Local Vertical Local Horizontal (LVLH) frame, also known as the Hill frame. In the case of this thesis, since the trajectory being propagated is that of the MMX spacecraft around Phobos, the frame is characterized by having the origin at the barycenter of Phobos with the X-axis pointing away from Mars in the line joining the centers of Mars and Phobos. The Z-axis is parallel to the angular momentum vector (hence perpendicular to the orbital plane) and the Y-axis completes the right-handed triad. In vector notation these axes are defined as shown below, where $\vec{r}_p$ is the position vector of Phobos and $\dot{\vec{r}}_p$ is the velocity vector of the moon. As mentioned, the LVLH frame is used to express the Cartesian position and velocity of the *MMX* spacecraft and a graphical representation can be found in Figure 4.2.

$$\hat{x} = \frac{\vec{r}_p}{||\vec{r}_p||} \quad ; \quad \hat{z} = \frac{\vec{r}_p \times \dot{\vec{r}}_p}{||\vec{r}_p \times \dot{\vec{r}}_p||} = \frac{\vec{h}}{||\vec{h}||} \quad ; \quad \hat{y} = \hat{z} \times \hat{x} \tag{4.7}$$
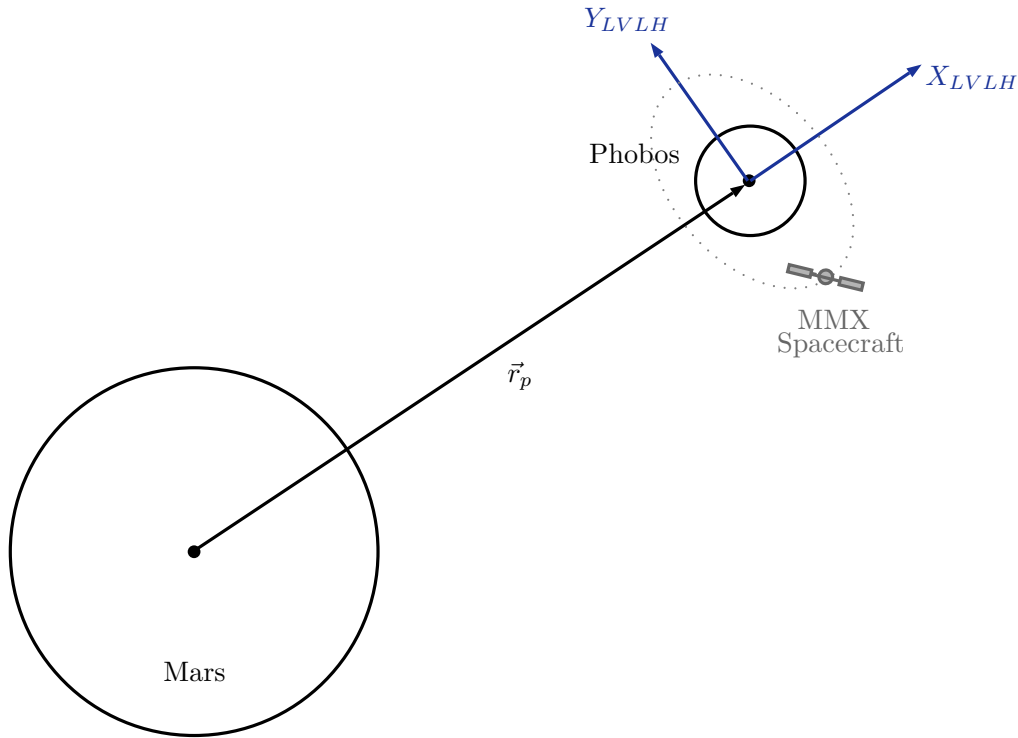
Figure 4.2: Schematic representation of the Local Vertical Local Horizontal frame as seen from its Z-axis, which points outwards of the paper. Diagram not to scale.

Since the LVLH frame is used to integrate the trajectory of MMX, it is necessary to express all the accelerations that the spacecraft experiences in this frame, which implies defining the corresponding rotation matrices. In particular, the following two rotations involving the LVLH frame have to be defined:

MCI - LVLH Transformation

Carrying out the transformation of vectors from the MCI to the LVLH frame and vice-versa is a straightforward operation. In general, the rotation matrix enabling the transformation from a frame A to a frame B corresponds to the matrix whose columns are the vectors defining frame A expressed in frame B.

As a result, the rotation matrix characterizing the transformation from LVLH to MCI, denoted as R_{LVLH}^{MCI} and given in Equation 4.8 below, can be constructed using the definitions given in Equation 4.7, provided that the vectors $\vec{r}_p$ and $\dot{\vec{r}}_p$ are expressed in the MCI frame. Similarly, passing from MCI to LVLH can be achieved by means of the transpose of R_{LVLH}^{MCI}.

$$R_{LVLH}^{MCI} = \begin{bmatrix} \hat{x} \; ; \; \hat{y} \; ; \; \hat{z} \end{bmatrix} \tag{4.8}$$

<u>LVLH - PCPF Transformation</u>

As was mentioned in Section 4.3.3, the Phobos Centered Phobos Fixed reference frame is used as an approximation to the Principal Axis frame of the moon, which is used to retrieve the gravity acceleration caused by the Phobos polyhedron model. The reader will find the details and justification involving this approximation later in Chapter 6, while this sub-section will explain how to perform the LVLH - PCPF transformations.

From the definitions provided in Section 4.3.3 it is known that both PCPF and LVLH have their origin at the Phobos barycenter. Further insight into the transformation is gained when taking into account that Phobos is tidally locked, meaning that it exhibits a synchronous rotation, so that the time period required for one orbit around Mars coincides with the time period required by the moon to rotate once about its spin axis [26].

Such property not only implies that Phobos always shows the same face to Mars, but, most importantly, that the Z-axis of the LVLH and PCPF frames are coincident, with the X-axis differing just by the definition of the moon's Prime Meridian, which, in turn, corresponds to the point that constantly points towards Mars in the moon's equator. As a result, the PCPF and LVLH frames difference is found in the fact that their X and Y axis are rotated 180 degrees. In reality, an oscillation ranging between 0.3 and 1.9 degrees is also present, but the 2.26 terrestrial years period characterizing this libration is considerably longer than the time for which the *MMX* mission will be propagated in this thesis [26]. Therefore, it is not taken into consideration and the rotation matrix enabling the transformation of vectors from PCPF to LVLH and vice-versa is given by:

$$R_{PCPF}^{LVLH} = \begin{bmatrix} -1 & 0 & 0 \\ 0 & -1 & 0 \\ 0 & 0 & 1 \end{bmatrix} \tag{4.9}$$

RELATIVE PERTURBED MOTION IN THE MARS - PHOBOS SYSTEM

Having defined the coordinate systems in Chapter 4, the next step is to present the Equations of Motion (EoMs) that the MMX High Fidelity Propagator integrates to obtain the orbit of Phobos around Mars as well as the spacecraft trajectory. As a result, the reader will find in this chapter all the information regarding the equations of relative motion for the case being considered, together with the derivations of the expressions for the angular velocity, angular acceleration and dynamical perturbation. Details regarding the initial conditions of both Phobos and MMX will also be provided in the last section.

Finally, in addition to the notation convention defined at the beginning of Chapter 4, please consider also that vector components will be written without a superscript arrow but with a subscript indicating which component it is (for example, the Z-component of $\vec{h}$ is written as h_z), and that time derivatives of the vectors or of their components will have a superscript dot or double dot.

5.1 Perturbed General Equations of Relative Motion

In general, to model relative motion dynamics two approaches can be followed: either Cartesian states are considered or either orbital elements are used. There is a extensive literature with derivations of these two models but, in most of the cases, the equations are

obtained under the assumption that there is only one primary body. This is however not the case in the Mars-Phobos system, where the gravitational attraction of both bodies must be taken into account. As a result, the well-known relative motion models such as the *Clohessy - Wiltshire* or *Tschauner - Hempel* equations cannot be used for the problem at hand.

Therefore, a new set of equations of relative motion has to be derived. For this thesis, the approach using Cartesian states has been followed and relative motion equations have been obtained in the Local Vertical Local Horizontal frame (presented previously in Section 4.4) following the reasoning found in reference [27]. In this frame, motion along the $\hat{x}$ and $\hat{y}$ directions is known as in-plane motion, while motion in the $\hat{z}$ direction is out-of-plane motion. As shown in Figure 5.1 below, lets denote the position and velocity vectors of MMX with respect to Phobos as $\vec{\rho}$ and $\dot{\vec{\rho}}$, while the position and velocity vectors of Phobos with respect to Mars will be $\vec{r}_p$ and $\dot{\vec{r}}_p$. Also, denote by $\vec{\omega}$ and $\dot{\vec{\omega}}$ the angular velocity and acceleration of the LVLH frame with respect to the Mars Centered Inertial frame.
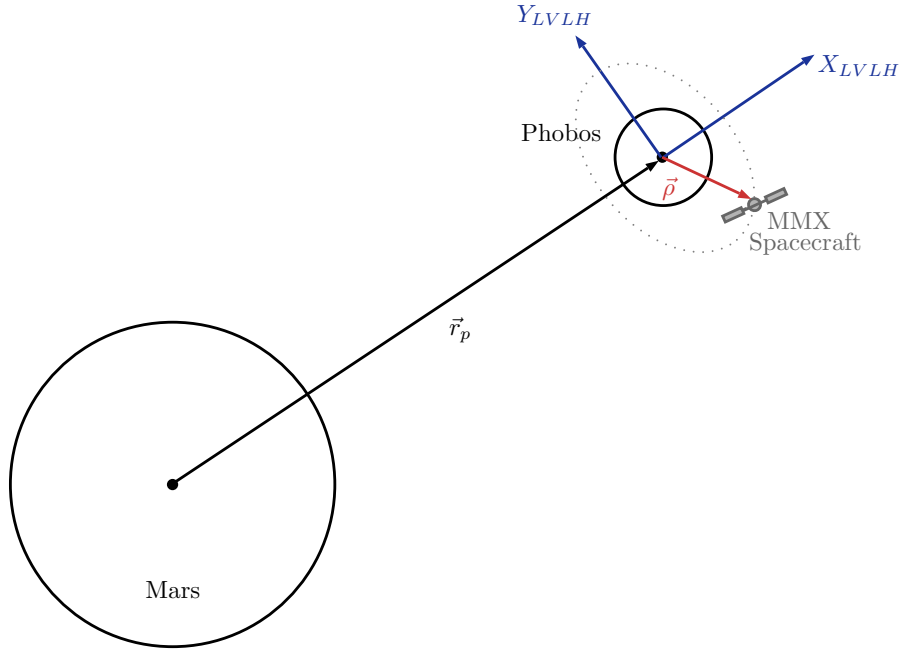
Figure 5.1: Graphical representation of the relative motion problem being considered.

As can be inferred from Figure 5.1, the absolute position of the spacecraft with respect to Mars can be defined as

$$\vec{r}_{tot} = \vec{r}_p + \vec{\rho} \tag{5.1}$$

from where the derivative with respect to time can be taken. Using $\frac{d}{dt}$ to denote the time derivative of a vector with respect to the inertial frame (MCI), and applying the Coriolis theorem yields:

$$\frac{d}{dt}\vec{r}_{tot} = \frac{d}{dt}\vec{r}_p + \frac{d}{dt}\vec{\rho} = \frac{d}{dt}\vec{r}_p + \dot{\vec{\rho}} + \vec{\omega} \times \vec{\rho} \tag{5.2}$$

Differentiating Equation 5.2 and operating gives the equations of motion of the MMX spacecraft as follows:

$$\begin{aligned}
\frac{d^2}{dt^2}\vec{r}_{tot} &= \frac{d^2}{dt^2}\vec{r}_p + \frac{d}{dt}\left(\dot{\vec{\rho}} + \vec{\omega} \times \vec{\rho}\right) = \frac{d^2}{dt^2}\vec{r}_p + \frac{d}{dt}\dot{\vec{\rho}} + \frac{d}{dt}\vec{\omega} \times \vec{\rho} + \vec{\omega} \times \frac{d}{dt}\vec{\rho} \\
&= \frac{d^2}{dt^2}\vec{r}_p + \ddot{\vec{\rho}} + \vec{\omega} \times \dot{\vec{\rho}} + \dot{\vec{\omega}} \times \vec{\rho} + \vec{\omega} \times \left(\dot{\vec{\rho}} + \vec{\omega} \times \vec{\rho}\right) \\
&= \frac{d^2}{dt^2}\vec{r}_p + \ddot{\vec{\rho}} + 2\vec{\omega} \times \dot{\vec{\rho}} + \dot{\vec{\omega}} \times \vec{\rho} + \vec{\omega} \times \left(\vec{\omega} \times \vec{\rho}\right)
\end{aligned} \tag{5.3}$$

In Equation 5.3, there are still two terms that can be operated further. In particular, $\frac{d^2}{dt^2}\vec{r}_{tot}$ and $\frac{d^2}{dt^2}\vec{r}_p$ represent the absolute acceleration of the spacecraft and of Phobos in the inertial frame (MCI). Introducing the assumption that the mass of the spacecraft is very small compared to the mass of the primaries (hence we are now considering the *restricted three body problem*), allows the aforementioned terms to be written as

$$\frac{d^2}{dt^2}\vec{r}_{tot} = -\frac{\mu_M}{||\vec{r}_{tot}||^3}\vec{r}_{tot} - \frac{\mu_P}{||\vec{\rho}||^3}\vec{\rho} + \vec{P}_{mmx} \tag{5.4}$$

$$\frac{d^2}{dt^2}\vec{r}_p = -\frac{\mu_M}{||\vec{r}_p||^3}\vec{r}_p + \vec{P}_p \tag{5.5}$$

where μ_M and μ_P are the gravitational parameters of Mars and Phobos respectively and the vectors $\vec{P}_{mmx}$ and $\vec{P}_p$ represent the generic perturbing accelerations experienced by the spacecraft and Phobos. Substituting Equations 5.4 and 5.5 into Equation 5.3 gives the general nonlinear equations of perturbed relative motion in the LVLH frame.

$$\ddot{\vec{\rho}} = -\frac{\mu_M}{||\vec{r}_{tot}||^3}\vec{r}_{tot} - \frac{\mu_P}{||\vec{\rho}||^3}\vec{\rho} + \frac{\mu_M}{||\vec{r}_p||^3}\vec{r}_p - 2\vec{\omega} \times \dot{\vec{\rho}} - \dot{\vec{\omega}} \times \vec{\rho} - \vec{\omega} \times \left(\vec{\omega} \times \vec{\rho}\right) + \Delta\vec{P} \tag{5.6}$$

In order to apply Equation 5.6, several terms such as the angular velocity, angular acceleration and the perturbation difference vector $\Delta \vec{P}$ have to be defined. Similarly, the type of orbit of Phobos around Mars has to be specified, as it can be circular (*circular restricted three body problem*), elliptical (*elliptic restricted three body problem*) or non-keplerian.

In this thesis, the perturbations being considered for the spacecraft are: spherical harmonics for the gravity of Mars, a polyhedron model for the gravity of Phobos, solar radiation pressure and solar third body gravitational attraction. On the other hand, non-keplerian motion will be considered for Phobos, since the spherical harmonics of Mars will be taken into account. The reader will find the equations for the angular velocity and acceleration of the LVLH frame in the upcoming sections. Finally, it must be noted that the MMX High Fidelity propagator integrates the equations of motion using the MATLAB solver *ode113* and that dimensionless quantities are used in the propagator, with lengths being normalized with the semi-major axis of Phobos and time with the inverse of the mean motion n. Table 5.1 below shows the values for the length and time units being used.

	Magnitude
Length Unit [m]	9377200
Time Unit [s]	4387.77138693593

Table 5.1: Values for the length and time units used to normalize variables in the MMX High Fidelity Propagator.

5.2   Time derivatives of the LVLH frame unit vectors

In order to derive the expressions for $\vec{\omega}$ and $\dot{\vec{\omega}}$, it is necessary to obtain first the time derivatives of the unit vectors of the Local Vertical Local Horizontal frame.

Time derivative of the unit vector $\hat{x}$

Starting with the X-direction and applying the corresponding derivation rule to the definition of vector $\hat{x}$ gives the following:

$$\hat{x} = \frac{\vec{r}_p}{||\vec{r}_p||} \longrightarrow \dot{\hat{x}} = \frac{\dot{\vec{r}}_p}{||\vec{r}_p||} - \frac{\frac{d}{dt}\left(||\vec{r}_p||\right)\vec{r}_p}{||\vec{r}_p||^2} \tag{5.7}$$

The term $\frac{d}{dt}\left(||\vec{r}_p||\right)$ can be expressed in a more convenient way by making use of the relation for the time derivative of a modulus, which characterized for the X-direction yields the following:

$$\frac{d}{dt}\left(||\vec{r}_p||\right) = \frac{\vec{r}_p}{||\vec{r}_p||} \cdot \frac{d\vec{r}_p}{dt} = \hat{x} \cdot \dot{\vec{r}}_p \tag{5.8}$$

Substituting the above expression into Equation 5.7 and taking into account that the position vector can be expressed as $\vec{r}_p = ||\vec{r}_p|| \, \hat{x}$ yields:

$$\dot{\hat{x}} = \frac{\dot{\vec{r}}_p}{||\vec{r}_p||} - \frac{\left(\dot{\vec{r}}_p \cdot \hat{x}\right)\vec{r}_p}{||\vec{r}_p||^2} = \frac{\dot{\vec{r}}_p}{||\vec{r}_p||} - \frac{\left(\dot{\vec{r}}_p \cdot \hat{x}\right)\hat{x}}{||\vec{r}_p||} \tag{5.9}$$

The numerator of the last term of Equation 5.9 can be simplified by transposing the vectors and making use of the associative property of matrices, with the term becoming $\left(\hat{x}\hat{x}^T\right)\dot{\vec{r}}_p$. Therefore, the final expression, where I is the identity matrix, is:

$$\dot{\hat{x}} = \frac{\dot{\vec{r}}_p}{||\vec{r}_p||} - \frac{\left(\hat{x}\hat{x}^T\right)\dot{\vec{r}}_p}{||\vec{r}_p||} \quad \longrightarrow \quad \dot{\hat{x}} = \frac{1}{||\vec{r}_p||}\left(I - \hat{x}\hat{x}^T\right)\dot{\vec{r}}_p \tag{5.10}$$

Time derivative of the unit vector $\hat{z}$

Similarly, one can also compute the time derivative of the $\hat{z}$ unit vector. Starting from the definition of $\hat{z}$ given in Section 4.4 and following a similar procedure to the one described above yields the following:

$$\hat{z} = \frac{\vec{r}_p \times \vec{v}_p}{||\vec{r}_p \times \vec{v}_p||} = \frac{\vec{h}}{||\vec{h}||} \quad \longrightarrow \quad \dot{\hat{z}} = \frac{1}{||\vec{h}||}\left(I - \hat{z}\hat{z}^T\right)\dot{\vec{h}} \tag{5.11}$$

Equation 5.11 can be modified by recalling the definition of the angular momentum and computing its corresponding time derivative, in which an acceleration term denoted as $\vec{f}$ appears, so that $\dot{\vec{h}} = \vec{r}_p \times \ddot{\vec{r}}_p = \vec{r}_p \times \vec{f}$. Hence, the final expression for the time derivative of the $\hat{z}$ vector is:

$$\dot{\hat{z}} = \frac{1}{||\vec{h}||}\left(I - \hat{z}\hat{z}^T\right)\left(\vec{r}_p \times \vec{f}\right) \tag{5.12}$$

Time derivative of the unit vector $\hat{y}$

Finally, the time derivative of the $\hat{y}$ vector can be obtained by deriving its definition and then substituting the expressions for $\dot{\hat{x}}$ and $\dot{\hat{z}}$, found in Equations 5.10 and 5.12 respectively. This gives:

$$\dot{\hat{y}} = = \frac{1}{||\vec{h}||}\left(\left(\vec{r}_p \times \vec{f}\right) \times \hat{x} - \hat{z}\hat{z}^T\left(\vec{r}_p \times \vec{f}\right) \times \hat{x}\right) + \hat{z} \times \frac{\dot{\vec{r}}_p}{||\vec{r}_p||} + \hat{z} \times \frac{1}{||\vec{r}_p||}\left(-\hat{x}\hat{x}^T\right)\dot{\vec{r}}_p \tag{5.13}$$

The obtained equation contains the term $\hat{z}\hat{z}^T\left(\vec{r}_p \times \vec{f}\right)$, which is the component of the vector resulting from the cross-product in the Z-direction. The associative property can be applied to the last term of Equation 5.13, retrieving that $\hat{x}^T\dot{\vec{r}}_p = \dot{r}_{p_x}$. Substituting and using the triple product rule yields:

$$\dot{\hat{y}} = \frac{1}{||\vec{h}||}\left(\left(\vec{r}_p \cdot \hat{x}\right)\vec{f} - \left(\vec{r}_p \cdot \vec{f}\right)\hat{x} - \left(\hat{z}^T \cdot \left(\vec{r}_p \times \vec{f}\right)\right)\hat{y}\right) + \hat{z} \times \frac{\dot{\vec{r}}_p}{||\vec{r}_p||} - \left(\frac{\dot{r}_{p_x}}{||\vec{r}_p||}\right)\hat{y} \tag{5.14}$$

Equation 5.14 can be further simplified using that $\vec{r}_p = ||\vec{r}_p||\hat{x}$. Hence, the term $\left(\vec{r}_p \cdot \hat{x}\right)$ simplifies to $||\vec{r}_p||$, and the term $\left(\vec{r}_p \cdot \vec{f}\right)\hat{x}$ converts into an expression with the projection of the force in the X-direction, namely $\left(||\vec{r}_p|| f_x\right)\hat{x}$. Substituting these results and simplifying gives the final expression for $\dot{\hat{y}}$:

$$\dot{\hat{y}} = \frac{1}{||\vec{h}||}\left(||\vec{r}_p||\left(\vec{f} - f_x\hat{x}\right) - \left(\hat{z}^T \cdot \left(\vec{r}_p \times \vec{f}\right)\right)\hat{y}\right) + \hat{z} \times \frac{\dot{\vec{r}}_p}{||\vec{r}_p||} - \left(\frac{\dot{r}_{p_x}}{||\vec{r}_p||}\right)\hat{y} \tag{5.15}$$

5.3   Angular velocity of the LVLH Frame

To obtain the expression for the angular velocity of the Local Vertical Local Horizontal frame one can use the so-called Poisson formula, which is no other than:

$$\vec{\omega} = \frac{1}{2}\left[\hat{x} \times \dot{\hat{x}} + \hat{y} \times \dot{\hat{y}} + \hat{z} \times \dot{\hat{z}}\right] \tag{5.16}$$

To re-write it, consider the three terms of Equation 5.16. Starting with $\hat{x} \times \dot{\hat{x}}$, the position vector and the definition of angular momentum can be used, obtaining:

$$\hat{x} \times \dot{\hat{x}} = \frac{\hat{x} \times \dot{\vec{r}_p}}{||\vec{r}_p||} = \frac{\vec{h}}{||\vec{r}_p||^2} \tag{5.17}$$

With respect to the second term, $\hat{y} \times \dot{\hat{y}}$, the expression can be developed by substituting first the definition of $\dot{\hat{y}}$ and then using the vector triple product rule. Since the scalar product of two perpendicular vectors is zero, the result is:

$$\hat{y} \times \dot{\hat{y}} = \hat{y} \times \left(\hat{z} \times \dot{\hat{x}}\right) + \hat{y} \times \left(\dot{\hat{z}} \times \hat{x}\right) = \left(\dot{\hat{x}} \cdot \hat{y}\right)\hat{z} - \left(\dot{\hat{z}} \cdot \hat{y}\right)\hat{x} \tag{5.18}$$

The last two terms of Equation 5.18 can be further developed. In particular, $\left(\dot{\hat{x}} \cdot \hat{y}\right)\hat{z}$ can be simplified by substituting $\dot{\hat{x}}$ by the velocity vector. Also, the scalar product $\dot{\vec{r}_p} \cdot \hat{y}$ is equivalent to the cross product $\hat{x} \times \dot{\vec{r}_p}$ (because the angle between vectors $\dot{\vec{r}_p}$ and $\hat{y}$ and the angle between $\dot{\vec{r}_p}$ and $\hat{x}$ are complementary). Hence:

$$\left(\dot{\hat{x}} \cdot \hat{y}\right)\hat{z} = \frac{\dot{\vec{r}_p} \cdot \hat{y}}{||\vec{r}_p||}\hat{z} = \frac{\vec{h}}{||\vec{r}_p||^2} \tag{5.19}$$

On the other hand, the term $-\left(\dot{\hat{z}} \cdot \hat{y}\right)\hat{x}$ from Equation 5.18 can be re-written, since it represents the component of the time derivative of vector $\hat{z}$ on the direction of $\hat{y}$, so that $-\left(\dot{\hat{z}} \cdot \hat{y}\right)\hat{x} = -\dot{\hat{z}}_y\,\hat{x}$. Substituting the definition of $\dot{\hat{z}}$ (given by Equation 5.12) yields:

$$-\left(\dot{\hat{z}} \cdot \hat{y}\right)\hat{x} = -\left[\frac{1}{||\vec{h}||}\left(\left(\vec{r}_p \times \vec{f}\right) - \left(\hat{z}^T \cdot \left(\vec{r}_p \times \vec{f}\right)\right)\hat{z}\right) \cdot \hat{y}\right]\hat{x} \tag{5.20}$$

Since $\hat{z}$ is perpendicular to $\hat{y}$, the second term of Equation 5.20 cancels out when doing the dot product. To the remaining term, $(\vec{r}_p \times \vec{f}) \cdot \hat{y}$, the so-called circular shift property can be applied to express it in a more convenient way, giving:

$$-\left(\dot{\hat{z}} \cdot \hat{y}\right)\hat{x} = -\left(\frac{1}{||\vec{h}||}\left(\vec{r}_p \times \vec{f}\right) \cdot \hat{y}\right)\hat{x} = -\left(\frac{1}{||\vec{h}||}\left(\hat{y} \times \vec{r}_p\right) \cdot \vec{f}\right)\hat{x} \tag{5.21}$$

Introducing into Equation 5.21 the definition of $\vec{r}_p$, taking into account that the resulting cross product is $\hat{y} \times \hat{x} = -\hat{z}$ and that then $\hat{z} \cdot \vec{f}$ is the component of the force in the Z-direction (f_z), yields the final expression for the second term of Equation 5.18, which is:

$$-\left(\dot{\hat{z}} \cdot \hat{y}\right)\hat{x} = \left(\frac{||\vec{r}_p||}{||\vec{h}||}\,\hat{z} \cdot \vec{f}\right)\hat{x} = f_z\frac{||\vec{r}_p||}{||\vec{h}||}\hat{x} \tag{5.22}$$

Finally, the third term of Equation 5.16, that is, $\hat{z} \times \dot{\hat{z}}$, can also expressed more conveniently. Recalling the definition of $\dot{\hat{z}}$ and then using the triple product rule leaves only $\left(\hat{z} \cdot \vec{f}\right)\vec{r}_p$, which is no other than the projection of vector $\vec{f}$ on vector $\hat{z}$:

$$\hat{z} \times \dot{\hat{z}} = \hat{z} \times \frac{\left(\vec{r}_p \times \vec{f}\right)}{||\vec{h}||} = \frac{\left(\hat{z} \cdot \vec{f}\right)\vec{r}_p}{||\vec{h}||} = f_z\frac{||\vec{r}_p||}{||\vec{h}||}\hat{x} \tag{5.23}$$

Hence, one can now substitute back into Equation 5.16 the derived terms, given in Equations 5.17, 5.19, 5.22 and 5.23, yielding the following:

$$\vec{\omega} = \frac{1}{2}\left[\frac{\vec{h}}{||\vec{r}_p||^2} + \frac{\vec{h}}{||\vec{r}_p||^2} + f_z\frac{||\vec{r}_p||}{||\vec{h}||}\hat{x} + f_z\frac{||\vec{r}_p||}{||\vec{h}||}\hat{x}\right] \tag{5.24}$$

Simplifying, the expression for the angular velocity of the Local Vertical Local Horizontal frame finally is:

$$\vec{\omega} = \frac{\vec{h}}{||\vec{r}_p||^2} + \frac{f_z}{||\vec{h}||}\vec{r}_p \tag{5.25}$$

5.4   Angular Acceleration of the LVLH frame

With respect to the angular acceleration, the expression can be obtained by deriving Equation 5.25. This yields:

$$\dot{\vec{\omega}} = \frac{\dot{\vec{h}}}{||\vec{r}_p||^2} - \frac{2\,||\vec{r}_p||\left(\frac{d}{dt}||\vec{r}_p||\right)\vec{h}}{||\vec{r}_p||^4} + \frac{1}{||\vec{h}||}\left(\dot{f}_z\vec{r}_p + f_z\dot{\vec{r}}_p\right) - \frac{\left(\frac{d}{dt}||\vec{h}||\right)f_z\vec{r}_p}{||\vec{h}||^2} \tag{5.26}$$

The formula obtained above can be simplified by making use of the definition provided previously in Equation 5.8 for the time derivative of the modulus of a vector, so that $\frac{\partial}{\partial t}||\vec{r}_p|| = \hat{x}\cdot\dot{\vec{r}}_p$ and $\frac{\partial}{\partial t}||\vec{h}|| = \hat{z}\cdot\dot{\vec{h}}$. Hence, the time derivative of the angular velocity is:

$$\dot{\vec{\omega}} = \frac{\dot{\vec{h}}}{||\vec{r}_p||^2} - \frac{2\left(\vec{r}_p\cdot\dot{\vec{r}}_p\right)\vec{h}}{||\vec{r}_p||^4} + \frac{\dot{f}_z\vec{r}_p + f_z\dot{\vec{r}}_p}{||\vec{h}||} - \frac{\dot{h}_z f_z\vec{r}_p}{||\vec{h}||^2} \tag{5.27}$$

5.5   Dynamical Perturbation and its Time Derivative

In Section 5.2, a new term denoted as $\vec{f}$ was introduced, which then appears in the expressions for the angular velocity and acceleration given in Equations 5.25 and 5.27. Such term can be defined as the dynamical perturbation that the LVLH frame experiences, which, at the same time, corresponds to the perturbation affecting Phobos, since the LVLH frame is attached to the moon and its orientation depends on its orbit.

As was mentioned in Section 5.1, Phobos is affected by the spherical harmonic model considered for the gravity of Mars. As a result, the dynamical perturbation vector $\vec{f}$ can be defined as the difference that the Phobos acceleration experiences with respect to the Keplerian case. As will be explained later in Chapter 6, the dynamical perturbation is obtained in the MCMF frame. Hence, in order to substitute the vector into the expressions for $\vec{\omega}$ and $\dot{\vec{\omega}}$ it has to be transformed into the LVLH frame. This can be done as follows, where the rotation matrices used have already been defined in Chapter 4 and the reference frame in which the vectors are expressed is denoted with a superscript notation:

$$\vec{f}^{LVLH} = [R]_{MCI}^{LVLH}\ [R]_{MCMF}^{MCI}\ \vec{f}^{MCMF} \tag{5.28}$$

Computing the time derivative of the dynamical perturbation can then be done by differentiating Equation 5.28, which yields:

$$
\dot{\vec{f}}^{LVLH} = \left([\dot{R}]^{LVLH}_{MCI} \, [R]^{MCI}_{MCMF} + [R]^{LVLH}_{MCI} \, [\dot{R}]^{MCI}_{MCMF} \right) \vec{f}^{MCMF}
$$
$$
+ \, [R]^{LVLH}_{MCI} \, [R]^{MCI}_{MCMF} \, \dot{\vec{f}}^{MCMF}
$$

(5.29)

In the first term of Equation 5.29 there are derivatives with respect to time of two different rotation matrices, namely $[\dot{R}]^{LVLH}_{MCI}$ and $[\dot{R}]^{MCI}_{MCMF}$. To compute their value, one must recall that direction cosine matrices satisfy the following kinematic differential equation [28]

$$
[\dot{R}] = -[\tilde{\omega}][R]
$$

(5.30)

where $[\tilde{\omega}]$ represents the skew symmetric matrix tilde operator of the angular velocity. Hence, the first time derivative of the rotation matrix found in Equation 5.29 is given by

$$
[\dot{R}]^{LVLH}_{MCI} = -[\tilde{\omega}]^{LVLH} \, [R]^{LVLH}_{MCI}
$$

(5.31)

where $[\tilde{\omega}]^{LVLH}$ is the tilde matrix operator of the angular velocity vector of the LVLH frame with respect to the MCI expressed in the LVLH base vectors. Hence, recalling the definition of the angular velocity of the LVLH frame given in Equation 5.25, the term $[\tilde{\omega}]^{LVLH}$ is written as

$$
[\tilde{\omega}] = \begin{bmatrix} 0 & -\dfrac{\vec{h}^{LVLH}}{||\vec{r}_p||^2} & 0 \\[3mm] \dfrac{\vec{h}^{LVLH}}{||\vec{r}_p||^2} & 0 & -\dfrac{f_z \, \vec{r}_p^{LVLH}}{||\vec{h}||} \\[3mm] 0 & \dfrac{f_z \, \vec{r}_p^{LVLH}}{||\vec{h}||} & 0 \end{bmatrix}
$$

(5.32)

Similarly, for the other time derivative of the rotation matrix the expression is

$$
[\dot{R}]^{MCI}_{MCMF} = -[\tilde{\omega}]^{MCI} \, [R]^{MCI}_{MCMF}
$$

(5.33)

with $[\tilde{\omega}]^{MCI}$ being the tilde operator of the angular velocity vector between the MCMF and MCI frames expressed in the MCI base. This vector is characterized by the fact that it

only has one component in the Z direction, with the magnitude being equal to the time derivative of the angle W defined previously in Section 4.3.2. Hence, the component is simply the angular velocity of Mars (2π divided by the sidereal rotation period of the planet).

Finally, the term $\dot{\vec{f}}_{MCMF}$ in Equation 5.29 can be computed using the gradient of the perturbation, so that the resulting expression is

$$\dot{\vec{f}}^{MCMF} = \nabla f^{MCMF} \, \dot{\vec{r}}_p^{MCMF} \tag{5.34}$$

where $\dot{\vec{r}}_p^{MCMF}$ can be obtained in a similar way as the one described above with the following expression:

$$\dot{\vec{r}}_p^{MCMF} = [\dot{R}]_{MCI}^{MCMF} \, \vec{r}_p^{MCI} \; + \; [R]_{MCI}^{MCMF} \, \dot{\vec{r}}_p^{MCI} \tag{5.35}$$

5.6 Initial Conditions

Propagating the orbits of Phobos and of the *MMX* spacecraft using the equations defined in the previous section requires a set of initial conditions. For the problem being considered, twelve initial conditions have to be provided, since twelve states are being integrated. In the following subsections the reader will find a detailed explanation of how were these initial positions and velocities retrieved.

5.6.1 Phobos Initial Conditions

To obtain the initial conditions for the orbit of Phobos around Mars, the simplest approach is to use the Horizons System developed by the Jet Propulsion Laboratory, which is available through an online interface. To do so, two things have to be taken into account: on the one hand, there is the need to specify an epoch at which the state vector is retrieved and, on the other hand, the JPL Horizons system has to be configured so as to retrieve the resulting state vector in the Mars Centered Inertial frame, as this is where the Phobos orbit is propagated. With respect to specifying the initial epoch, two things are known:

- From the timeline shown in Figure 1.2, it is expected that MMX will enter the Quasi-Satellite Orbits around the 1st of August 2025, so the initial epoch should be close to that date.

- From the MMX initial conditions data provided by Nicola Baresi, it is known that the value of the true anomaly of Phobos at the epoch which corresponds with the initial conditions of the spacecraft is $\theta_0 = 5.67019161867426$ *rad*.

Hence, the objective is to define an initial epoch which is close to August 1, 2025 and at which the true anomaly of Phobos is the value given. This can be done by using

$$M = M_1 + n\left(t - t_1\right) \longrightarrow t = \frac{M - M_1}{n} + t_1 \tag{5.36}$$

where M is the mean anomaly that corresponds to θ_0 and which can be computed via the eccentric anomaly, M_1 is the Phobos mean anomaly at the reference epoch 01-Aug-2025 (with the value being obtained from JPL Horizons) and n is the mean angular motion. Equation 5.36 will therefore give the date at which the Phobos true anomaly is θ_0, which will then be the initial epoch that is considered in the propagator. This date is found to be July 31st, 2025 at 19:46:41 UT, which corresponds to the Julian Date $JD_0 = 2460888.32407819$. With this initial epoch, the JPL Horizons System can then be used to retrieve the state vector of the Martian moon in the MCI frame, with the values being given in Table 5.2 below.

State	Magnitude
X [km]	-1.115940288793653 $\times 10^3$
Y [km]	9.190589512217197 $\times 10^3$
Z []km]	1.085752281853547 $\times 10^2$
V_x [km/s]	-2.146065723009760
V_y [km/s]	-2.797005274171575 $\times 10^{-1}$
V_z [km/s]	3.102479521763912 $\times 10^{-2}$

Table 5.2: Phobos initial state vector expressed in the Mars Centered Inertial frame. Values with no rounding off, as retrieved from the Horizons system. The initial epoch corresponds to July 31st,2025 at 19:46:41 UT.

5.6.2   Initial Conditions for *MMX*

With respect to the initial conditions of the Quasi-Satellite Orbits of the *MMX* spacecraft, two different sets were provided by Nicola Baresi: one for a low-altitude 30 × 50 km orbit and another set for a mid-altitude 100 × 200 km orbit. Both had the particularity of being were expressed in a pulsating reference frame (denoted as S). As a result, a transformation from S to the LVLH frame had to be performed in order for these initial conditions to be used in the MMX propagator.

The synodic frame is characterized by being centered at Phobos, with the X-direction being defined by the separatrix between the Mars and Phobos barycenters, the Z-axis being parallel to the orbital angular momentum and the Y-axis completing the right-handed system [29]. Furthermore, in this frame the spacecraft position is scaled by the Mars - Phobos distance d, time is substituted by the true anomaly θ of the Martian moon and the constant $\zeta = \left(\frac{\mu_P}{\mu_M}\right)^{1/3}$ is used, where μ_P and μ_M are the Phobos and Mars mass parameters respectively. With these definitions, converting the initial conditions from the S frame to the Local Vertical Local Horizontal can be achieved by means of the expressions provided by reference [30], namely

$$
\begin{aligned}
\vec{r} &= \zeta \, d \, \vec{r}_S \\
\dot{\vec{r}} &= \zeta \, \dot{\theta} \left(d' \vec{r}_S + d \, \vec{r}_S' \right)
\end{aligned}
\tag{5.37}
$$

where $\vec{r}_S$ is the spacecraft position vector in the synodic frame, $\vec{r}_S'$ is the derivative of this vector with respect to the Phobos true anomaly, $\dot{\theta}$ is the rate of change of the true anomaly and d' is the derivative of d with respect to θ. Computing these parameters can be done using the following equations

$$
d = \frac{p}{1 + e \cos\theta}
\tag{5.38}
$$

$$
d' = \frac{d^2}{p} e \sin\theta
\tag{5.39}
$$

$$
\dot{\theta} = \frac{\sqrt{\mu_M p}}{d^2}
\tag{5.40}
$$

where $p = a\,(1 - e^2)$ is the moons orbital parameter or *semi-latus rectum*, being a the semi-major axis and e the eccentricity. Using the above expressions and the values for μ_P, μ_M, p and θ_0 provided by Nicola Baresi yielded the initial conditions for the MMX spacecraft expressed in the LVLH frame, found in Table 5.3 below.

State	30 × 50 km QSO	100 × 200 km QSO
X [km]	29.3237881750688	99.8014771706819
Y [km]	-9.01301842442985 $\times 10^{-2}$	-1.92352019971823
Z [km]	-9.52716782326782	-7.49367543330828
V_x [km/s]	2.79525006230658 $\times 10^{-6}$	-1.12847704407331 $\times 10^{-5}$
V_y [km/s]	-1.52183121555763 $\times 10^{-2}$	-4.65043626913888 $\times 10^{-2}$
V_z [km/s]	6.74255893460753 $\times 10^{-4}$	7.83657113033875 $\times 10^{-4}$

Table 5.3: Cartesian initial conditions expressed in the Local Vertical Local Horizontal frame for two Quasi-Satellite Orbits. Values have not been rounded up so as to provide highest possible accuracy.

6

PERTURBATIONS

The equations of motion defined previously in Chapter 5 contain terms which represent the different perturbations which are being considered in the propagation of the orbits. Therefore, this chapter will now explain the models used for these perturbations as well as the corresponding assumptions and simplifications followed for their implementation.

6.1 Mars Gravity

As was shown in Tables 1.1 and 1.2 of Chapter 1, Mars is by far the most massive body of the Martian system and, as a result, is responsible for the biggest gravitational acceleration. Hence, modelling this perturbation with a great accuracy is a must.

The gravity field generated by Mars is indeed non-uniform, since the body has an irregular shape. When this is the case, the actual discrepancy from the perfect spherical geometry can be taken into account by means of the spherical harmonic approach.

This approach is based on the fact that gravity is a conservative force and, as such, can be written as the gradient of a potential function V. The complete derivation of the expression for the gravitational potential can be found in reference [31], and only a brief summary will be provided here. Hence, considering the mass of the planet to be composed of infinitesimal masses, the potential at a point P due to the whole mass of Mars can be written as

$$\text{V} = G \int_M \frac{1}{|\vec{r} - \vec{s}|} \mathrm{d}M \tag{6.1}$$

where $|\vec{r} - \vec{s}|$ is the magnitude of the vector between a differential mass element $\mathrm{d}M$ and point P, G is the gravitational constant and M is the total mass of the planet, as is shown below in Figure 6.1.
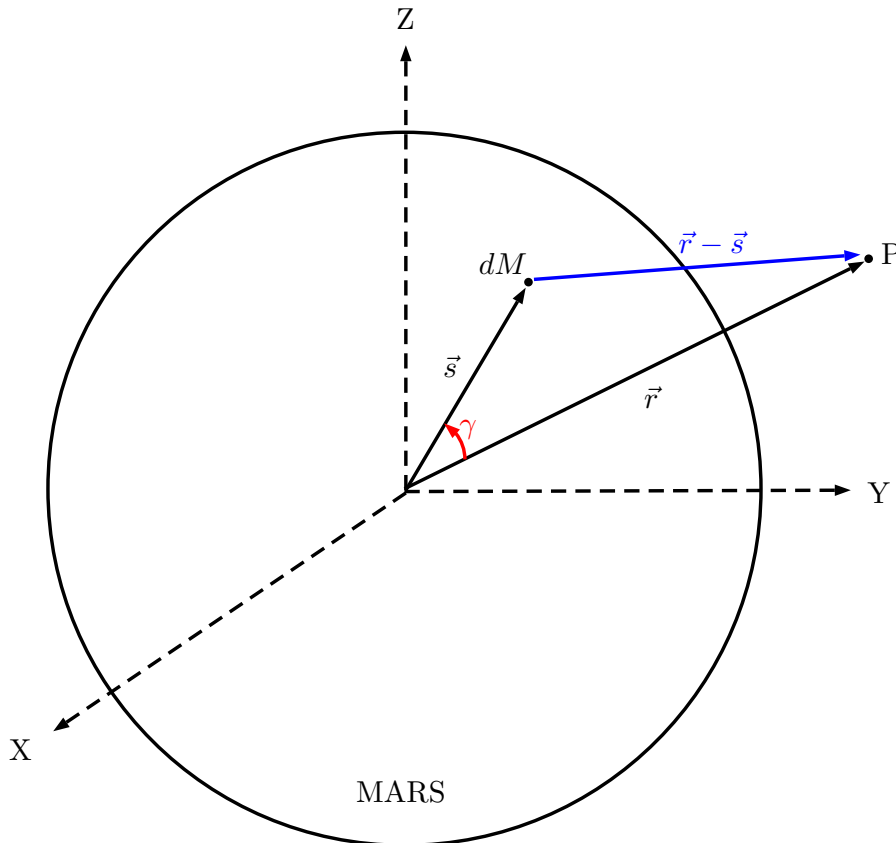
Figure 6.1: Schematic representation of a differential element of mass and the geometric parameters involved in the derivation of the gravitational potential at a point P.

Solving the expression above is simplified if the fraction $\frac{1}{|\vec{r} - \vec{s}|}$ is written in terms of a series of spherical harmonics, known as Legendre polynomials, so that the result is as follows, with P_i being the polynomial of degree i:

$$\frac{1}{|r - s|} = \frac{1}{r} \left[1 + \left(\frac{s}{r} \right)^2 - 2 \left(\frac{s}{r} \right) \cos \gamma \right]^{-\frac{1}{2}} = \frac{1}{r} \sum_{i=0}^{\infty} \left(\frac{s}{r} \right)^i P_i(\cos \gamma) \tag{6.2}$$

Substituting Equation 6.2 and integrating over the distribution of mass gives the expression for the gravity potential that a planet generates at point P, being the position of such point expressed in spherical coordinates r, λ and θ:

$$V(r,\lambda,\theta) = \left(\frac{\mu}{r}\right) \sum_{n=0}^{\infty} \sum_{m=0}^{n} \left(\frac{R_e}{r}\right)^n \left[C_{nm}\cos(m\lambda) + S_{nm}\sin(m\lambda)\right] P_{nm}(\cos\theta) \qquad (6.3)$$

In the above equation, μ is the gravitational parameter, P_{nm} are the Legendre functions of degree n and order m, R_e is the planet's mean equatorial radius and C_{nm} and S_{nm} are the so-called Stokes coefficients, whose values are determined from satellite measurements and terrestrial observations and which account for the irregular mass distribution of the planet. Whenever $m = 0$, the Stokes coefficients are denoted as zonal coefficients, while they are called tesseral coefficients when $m < n$ and sectorial if $m = n$.

As a result, modelling the gravity of a planet by means of the spherical harmonic approach requires having values for the Stokes coefficients, being this set of values the ones that define and distinguish one model from another. For instance, in the case of Mars, there are up to 10 different models, ranging from the first one developed in 1982 and available in reference [32] to the latest one, GMM3, published in 2016.

6.1.1 The GMM3 Model

The Goddard Mars Model 3, (GMM3), is a gravity model for Mars which provides a spherical harmonic solution of up to degree and order 120. As has been mentioned, it is the most recent one and has been created based on the data retrieved by three different NASA spacecraft over the last sixteen years: Mars Global Surveyor, Mars Odyssey and Mars Reconaissance Orbiter [11].

The measurements used to develop this model were acquired by observing the small perturbations that those spacecraft experienced as they orbited Mars, something which was achieved via the ground stations of NASA's Deep Space Network, and the GMM3 model was presented in the paper available in reference [33]. With respect to the data used in this thesis, it is publicly available on NASA's Planetary Data System, where the user can download the files which contain the normalized Stokes coefficients. These values provide the most

accurate model of the Martian gravity up to date and Figure 6.2 below shows a graphical representation of this gravity as defined by this model.
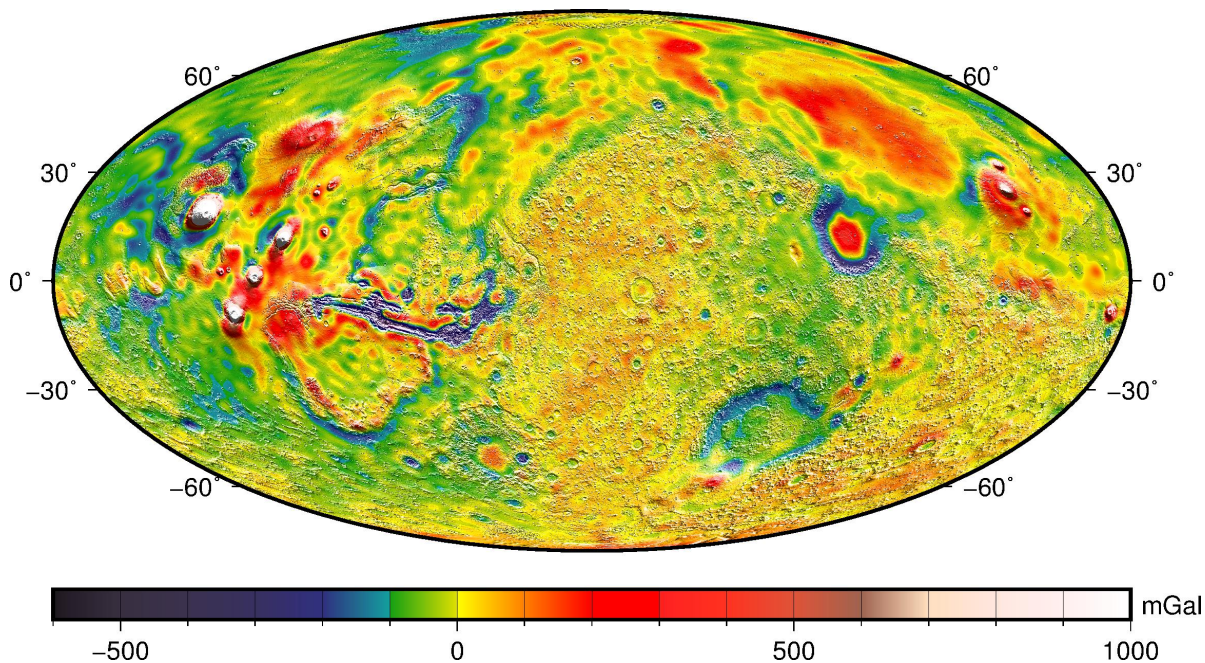
Figure 6.2: Free-air gravity map according to the GMM3 model. It shows the variations with respect to the mean gravity of Mars, measured in milligals. Red and white are the regions were the departure is greatest, while blue and purple represent the areas where the gravity is lower than average. Image taken from [11].

6.1.2 Implementation

Once the data had been retrieved, it had to be treated in order for it to be useful to the MATLAB function which computed the gravity acceleration as well as its gradient, which was required for Equation 5.27. In particular, these two values were obtained by applying the method developed by Leland E. Cunningham in 1969 and available in reference [34], and the MATLAB routine which implemented the aforementioned procedure was provided by Nicola Baresi.

As a result, after the coefficients have been organized into the corresponding matrix arrangements, it is necessary to perform an un-normalization process, since the method developed by Cunningham uses un-normalized coefficients. The relation between the normalized coefficients, denoted as $\overline{C}_{nm}$ and $\overline{S}_{nm}$, and the un-normalized values (without bar) is given by the following expression, where δ_{0m} is the Kronecker delta function, which gives a value of one if $m = 0$ or zero in the rest of cases:

$$\begin{pmatrix} C_{nm} \\ S_{nm} \end{pmatrix} = \left[\frac{(n-m)!(2n+1)\left(2-\delta_{0m}\right)}{(n+m)!} \right]^{1/2} \begin{pmatrix} \overline{C}_{nm} \\ \overline{S}_{nm} \end{pmatrix} \tag{6.4}$$

The usage of unnormalized coefficients presents a small drawback, which is caused by the fact that the normalization factor shown in Equation 6.4 gets smaller as the degree and order are increased due to the presence of the term $(n+m)!$ in the denominator. As a result, after degree and order 80, MATLAB rounds up the factor to zero, hence causing that the spherical harmonic solution to be considered in the propagator only reaches the mentioned order and degree. Indeed, this causes a loss of accuracy in comparison to the solution reaching degree and order 120 but, for the scope of this thesis, this is not a problem since the major effects of the Martian gravity are contained in the lower degrees and orders, being 80 more than sufficient for the accuracy desired.

The last practical remark that the reader must consider is that the Cunningham procedure requires the position vectors to be introduced in the Mars Centered Mars Fixed frame. Therefore, the position vectors of Phobos and of the MMX spacecraft have to undergo a transformation process in order to express them in the desired frame. Similarly, the resulting acceleration and gravity gradient are obtained in the MCMF frame.

6.2 Phobos Gravity

Having explained the details behind the gravitational model used for Mars, it is now turn to address the one used for Phobos. In the case of the Martian moon, modelling the gravity acceleration is more complicated, since the degree of inaccuracy is greater due to the fact that the available measurements concerning Phobos are scarce and, in some cases, old. Furthermore, the moon is characterized by a highly irregular shape and the mass and density estimates are still subject to modifications as new studies are performed.

Dealing with bodies which present these difficulties, such as asteroids and comets, is therefore not simple. However, good accuracy levels can be achieved by means of polyhedron models, as was the case for the *Rosetta* mission to the 67P/Churyumov-Gerasimenko comet [35]. This section will therefore present the polyhedron model being used for Phobos as well as some characteristics involving its implementation in the MATLAB propagator.

6.2.1 The Polyhedron Model

In the case of irregular bodies, a longitudinal dependence is normally found in the expression for the gravity potential, since there is no axisymmetric shape as in the case of planets [35]. Thus, obtaining an equation using a spherical harmonic model is complicated and not practical, as the convergence of the harmonic expansion is no longer guaranteed due to the mass distribution changes and also there is no information regarding whether a field point is inside or outside the body [36]. Overcoming the problems posed by a spherical harmonic model can be achieved by means of the polyhedron model, which obtains an expression for the gravity field by approximating the shape of the body with a constant density polyhedron.

This approach presents several advantages: on the one hand, the geometry of the body is divided into smaller pieces of polyhedral shape, thus permitting craters, peaks, grooves and other surface features to be considered. In addition, the gravity field obtained is exact, and errors are only produced by inaccuracies inherent to the shape determination, so there are no convergence issues. Finally, and although this will not be used in this thesis, such model enables to obtain the gravitational accelerations at the surface of the body, therefore being useful for further studies of the *MMX* mission [36]. This section will now provide a brief review of the equations and mathematics behind such model, with the reader being able to find the complete formulae and derivations in reference [36].

Constructing a polyhedron model implies dividing the body being characterized into polygons (usually triangles or parallelepipeds, although other configurations can be used). These polygons have surfaces (known as faces, subscript f) that will meet each other at either edges (subscript e) or vertices (V), and it is required to define the connective sequence so as to correctly build the model. Once this is done, each polyhedron face will have a vector normal to it and pointing outwards from the body ($\vec{n}_f$), and a face dyad $F_f = \vec{n}_f \vec{n}_f$, while each edge of each face will have another outward-pointing normal vector $\vec{n}_e^f$, which is perpendicular to both the edge and $\vec{n}_f$. For the edge connecting two vertices (for instance V_i and V_j, see Figure 6.3), an edge dyad also exists, given by $E_{ij} = \vec{n}_A \vec{n}_{ij}^A + \vec{n}_B \vec{n}_{ji}^B$, where $\vec{n}_A$ and $\vec{n}_B$ are the normal vectors of faces A and B, and $\vec{n}_{ij}^A$ and $\vec{n}_{ji}^B$ are the previously mentioned edge normal vectors.
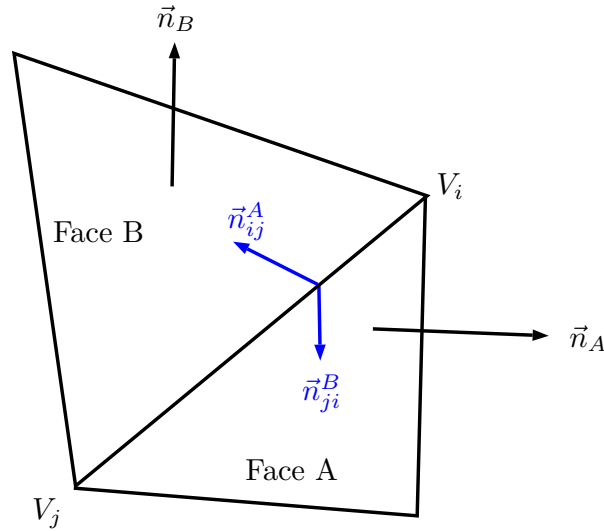
Figure 6.3: Graphical representation of the normal vectors associated to two faces which join at an edge defined by two vertices.

Consider now $\vec{r}_i$ to be the vector from a point from the field to vertex V_i and r_i to be its magnitude. Each edge connecting two vertices (such as V_i and V_j) will have associated a dimensionless factor L_e defined as

$$L_e = \ln \frac{r_i + r_j + e_{ij}}{r_i + r_j - e_{ij}} \tag{6.5}$$

where e_{ij} is the length of the edge. Similarly, for each face f defined by three vectices V_i, V_j and V_k, there exists a dimensionless face factor ω_f given by:

$$\omega_f = 2\arctan\left[\frac{\vec{r}_i \cdot \left(\vec{r}_j \times \vec{r}_k\right)}{r_i r_j r_k + r_i\left(\vec{r}_j \cdot \vec{r}_k\right) + r_j\left(\vec{r}_k \cdot \vec{r}_i\right) + r_k\left(\vec{r}_i \cdot \vec{r}_j\right)}\right] \tag{6.6}$$

With these definitions, and considering G and σ_p to be the gravitational constant and the polyhedrons constant density respectively, the gravitational potential can be expressed as

$$U = \frac{1}{2}G\sigma_p\left[\sum_{e\in\text{ edges}} \vec{r}_e E_e \vec{r}_e L_e - \sum_{f\in\text{ faces}} \vec{r}_f F_f \vec{r}_f \omega_f\right] \tag{6.7}$$

from where the expression for the gravity acceleration can be easily obtained recalling that $\vec{g} = -\nabla U$, so that

$$\vec{g} = -G\sigma_P \left[\sum_{e \in \text{edges}} E_e \, \vec{r}_e \, L_e \; - \sum_{f \in \text{faces}} F_f \, \vec{r}_f \, \omega_f \right] \tag{6.8}$$

where $\vec{r}_e$ is the position vector (relative) of the spacecraft with respect to the e-th edge and $\vec{r}_f$ is the relative position vector with respect to a point on the f-th face [36].

6.2.2 Implementation

The first step in the implementation of the polyhedron model for Phobos is to select which one to use. Currently, only two models are available to the public in NASA's Planetary Data System (PDS) Small Bodies Node, and both were developed by R. W. Gaskell in 2006 and 2012 respectively. Although these two models could be used without problem, this thesis has instead implemented one provided by Nicola Baresi, which is characterized by having 40962 vertices and 81920 triangular faces, connected between each other by means of 122880 edges. Figure 6.4 below shows a view of the mentioned model.
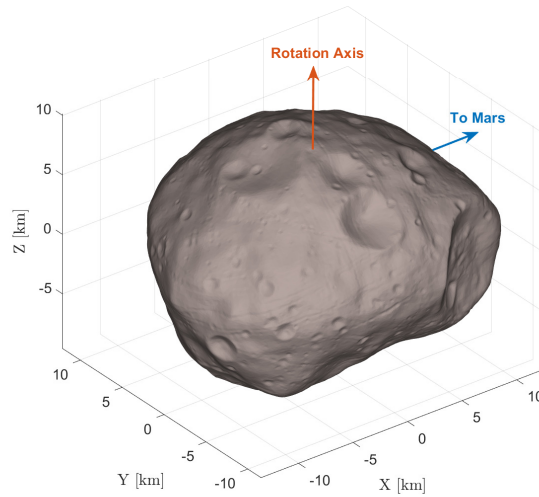
Figure 6.4: Three dimensional view of the polyhedral model used for Phobos.

In order to compute the gravitational acceleration caused by Phobos on the *MMX* spacecraft, the position vector has to be expressed in a body-fixed frame oriented such that the X,Y and Z axis correspond with the minimum, medium and maximum axes of inertia [37] [38]. As a result, the *MMX* position vector has to be transformed from the LVLH frame to the one just mentioned.

This can be simplified by taking into account that studies, such as the ones provided in reference [39] and [40], have shown that the misalignment between the principal axes of inertia frame and the body fixed frame defined according to the IAU convention (PCPF) is very small, of approximately 1.2 ° . Therefore, it can be considered that the Principal Axes frame and the PCPF frame are coincident. With this simplification, the transformation of the spacecraft position vector from the LVLH frame to the one required by the polyhedron model reduces to a rotation from LVLH to PCPF which, as explained before in Section 4.4, consists on a 180 °rotation of the X-Y axes. Looking at Figure 6.4, the reader can notice how the direction pointing to Mars is along the positive X-axis, while in the LVLH frame the positive X-axis points away from Mars.

6.3   Solar Radiation Pressure

Once the two main gravitational perturbations involved in the dynamical environment have been presented, it is turn for this section to address the first and only non-gravitational perturbation considered in the *MMX* High Fidelity propagator. In particular, the propagator takes into account the perturbing acceleration caused by the solar radiation pressure (commonly denoted as *SRP*) on the spacecraft. This force would also act on the small body (Phobos) through the Yarkosvky and YORP effects, but both are not taken into account since the spacecraft orbit time is much smaller than the time scale of the effects [41]. As a result, the reader will find in the subsequent sections information regarding the model used as well as details concerning its implementation in the propagator.

6.3.1   SRP Model

Solar radiation pressure is the force that results from the impact of particles emitted by the Sun on the surface of the spacecraft. In particular, one of the outer layers of the Sun, known as the *photosphere*, acts as a black-body and hence emits radiation that spans throughout most of the electromagnetic spectrum, from radiowaves to X-rays [6]. The emitted photons, which are massless particles, then travel at the speed of light and eventually impinge on the

spacecraft, which experiences a perturbing acceleration due to the fact that the energy and momemtum of the photons is not zero. For high-precision orbit propagation it is therefore necessary to include the SRP effect, which also depends on the ballistic properties of the spacecraft.

Several models of diverse complexity have been proposed in the past, from the simplest cannonball model, in which the spacecraft is considered to be a sphere, to box-wing models such as the one in reference [42] where solar panels and the main structure are considered separately, to others much more complex in which the satellite and its position with respect to the Sun are modelled by means of Fourier series, such as the one in reference [43].

For the scope of this thesis, it is sufficient to consider a cannonball model as the ones provided in references [41] and [44]. In such case, the perturbing acceleration that has to be included in the *MMX* equations of motion is given by

$$\vec{a}_{SRP} = -\eta\, C_{\mathrm{R}} \left(\frac{A_{sc}}{M_{sc}} \right) \left(\frac{S}{c} \right) \left(\frac{1\,AU}{||\vec{r}_{sun} - \vec{r}_o||} \right)^2 \frac{\vec{r}_{sun} - \vec{r}_o}{||\vec{r}_{sun} - \vec{r}_o||} \tag{6.9}$$

where the minus sign denotes that it is directed away from the Sun, η is the shadow function, which is 0 if the spacecraft is under eclipse conditions and 1 otherwise, *Cr* is the radiation pressure coefficient with values between 1 (the body behaves as a black body and absorbs all the incoming radiation) or 2 (the body reflects all the incident radiation), A_{sc} and M_{sc} are the area and mass of the spacecraft respectively, S is the radiation intensity, c is the speed of light, *AU* is the astronomical unit in meters and $\vec{r}_{sun}$ and $\vec{r}_o$ are the vectors from the body to the Sun and from the body to the spacecraft respectively. In addition, the third bracketed term comes from the modeling of the body's orbit around the Sun, which causes changes in the incident solar radiation. For instance, for the case of Earth, such changes are known as the *Milankovitch cycles* [45].

In order to apply Equation 6.9, it is necessary to determine the values of the radiation intensity S, of the shadow function η and of the position vector $\vec{r}_{sun}$. The former can be obtained by considering that electromagnetic radiation follows an inverse squared relation with distance [6]. Hence,

$$S = S_0 \left(\frac{R_{ph}}{||\vec{r}_{sun}||} \right)^2 \tag{6.10}$$

where $S_0 = \sigma T^4$ is the Sun's radiated power intensity at its surface and is computed following the Stefan-Boltzmann law, R_{ph} is the radius of the photosphere and $||\vec{r}_{sun}||$ is the distance between the Sun and the body. The values used to determine the radiation intensity S are provided in Table 6.1 below.

Constant	Magnitude	Units
σ	5.67×10^{-8}	$W/m^2\,K^4$
T	5777	K
R_{ph}	696000	km

Table 6.1: Magnitude of the different constants involved in the computation of the radiated power intensity at a certain distance. Values taken from reference [6].

On the other hand, determining the value of the shadow function can be done by considering a simple eclipse model such as the one proposed in references [6] and [46], which is mainly based on geometrical relationships. In particular, consider Figure 6.5 below, where the Sun and the spacecraft are located at two different points and their corresponding position vectors define the plane shown. The central body (Mars) is assumed to be circular. In that case, the angle between the two vectors can be obtained as:

$$\psi = \cos^{-1}\left(\frac{\vec{r}_{sun} \cdot \vec{r}_o}{||\vec{r}_{sun}||\,||\vec{r}_o||}\right) \tag{6.11}$$

To determine whether the spacecraft is in shadow or not, it is then necessary to compute the angles ψ_{sun} and ψ_o, which are no other than the angles between the vectors $\vec{r}_{sun}$ and $\vec{r}_o$ with the tangent points T_1 and T_2 respectively. Both angles can be obtained using the following expressions, where R_e is the mean radius of Mars:

$$\psi_{sun} = \cos^{-1}\left(\frac{R_e}{||\vec{r}_{sun}||}\right) \qquad and \qquad \psi_o = \cos^{-1}\left(\frac{R_e}{||\vec{r}_o||}\right) \tag{6.12}$$

Once this values are obtained, it is straightforward to determine if the spacecraft is in eclipse or not. If $\psi_{sun} + \psi_o < \psi$, then the spacecraft is in eclipse conditions since there is no line of sight with the Sun and the shadow function η is zero. If, on the other hand, $\psi_{sun} + \psi_o \geq \psi$, then the spacecraft is in full illumination and $\eta = 1$. It must be noted that this model neglects the existence of the so-called penumbra region, where the shadow function would have a value between 0 and 1, and therefore overestimates the eclipse duration.
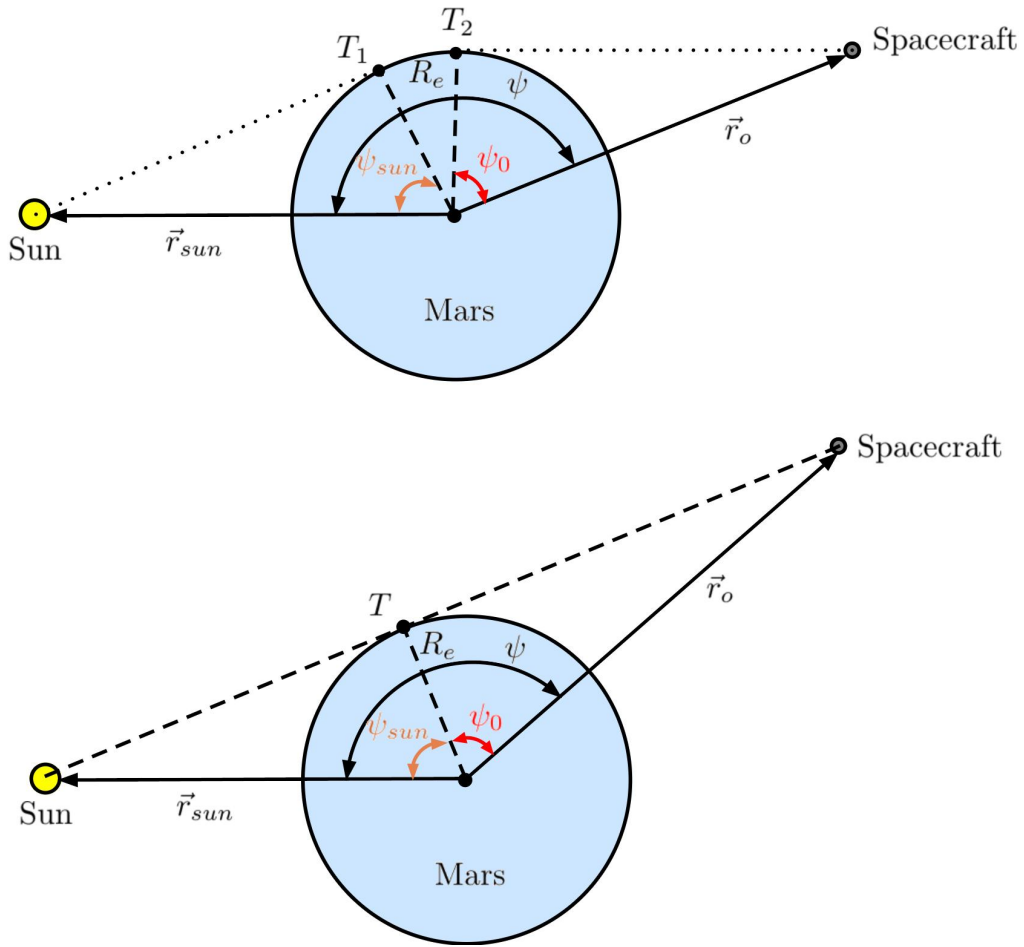
Figure 6.5: Graphical representation of the eclipse model, showing shadow conditions (upper image) and the limit case that establishes the transition between eclipse and full illumination conditions (lower image).

Finally, the position vector $\vec{r}_{sun}$ is assumed to be the vector from Mars to the Sun. This implies that, due to the small dimensions of Phobos, the eclipses that could be caused by the moon are not taken into account.

6.3.2 Implementation

The first step that has to be taken for the implementation of the solar radiation pressure model is the computation of the $\vec{r}_{sun}$ vector. This can be done by assuming that the orbit of Mars around the Sun is Keplerian. In that case, the orbit equation (defined previously in Equation 5.38) applies, and the value of the heliocentric true anomaly (denoted as θ_H) can be determined by first finding the mean anomaly and then using a *Newton-Raphson*

method to retrieve the eccentric anomaly, from where the value of θ_H follows. Once the true anomaly is known, the magnitude of $\vec{r}_{sun}$ is obtained and the vector can be expressed in the Heliocentric Perifocal frame defined in Section 4.2.3 as

$$\vec{r}_{sun}^P = ||\vec{r}_{sun}|| \begin{bmatrix} \cos\theta_H \\ \sin\theta_H \\ 0 \end{bmatrix} \tag{6.13}$$

Since the solar radiation pressure has to be expressed in the LVLH frame, the vector has to be transformed. This is done following the sequence shown below, where the corresponding rotation matrices have already been defined in Chapter 4 and the minus sign is introduced to change the direction so that it points from Mars to the Sun:

$$\vec{r}_{sun}^{LVLH} = - [R]_{MCI}^{LVLH} [R]_{EME}^{MCI} [R]_{I}^{EME} [R]_{P}^{I} \vec{r}_{sun}^P \tag{6.14}$$

With respect to the ballistic properties of the spacecraft, provisional values regarding the spacecraft mass are available in Table 1.4. However, the author has not been able to find values for the spacecraft area A_{sc}, so determining a precise mass-to-area ratio is not possible. Hence, the values provided in reference [41] have been used and the mass-to-area ratio has been considered to be equal to 40. Similarly, the C_r coefficient has been assumed to be equal to 1.5. With respect to the radiation intensity, the computed value at the initial epoch is $S = 525.625 \left(\frac{W}{m^2} \right)$, being found inside the range provided by the JPL Horizons System, which indicates that this parameter has a value of $717 \left(\frac{W}{m^2} \right)$ at perihelion and $493 \left(\frac{W}{m^2} \right)$ at aphelion.

6.4 Third-Body Gravitational Perturbation of the Sun

The last perturbation that is included in the MMX High Precision propagator, and which at the same time has the smallest magnitude of the ones being considered, is the gravitational perturbation caused by the Sun. Although the Martian system is found at an average distance of 227,940,000 km, the star is the most massive body in the Solar System and hence produces a gravitational attraction force that has to be taken into account. The reader will find in the next section a description of the model used.

6.4.1 Model

As was explained in the previous section, in the MMX High Fidelity propagator the Sun - Body position vectors used in the equations are obtained considering that the body is Mars. Hence, accounting for the gravitational attraction exerted by the Sun on the spacecraft can be done in a simple way if it is assumed that Mars exhibits a two-body orbit relative to the Sun. Therefore, the model proposed in reference [41] is introduced into the propagator, since it enables to capture the relevant effects of the perturbation. The expression for the perturbing gravitational acceleration is

$$\vec{a}_{3^{rd}sun} = -GM_{sun}\left[\frac{(\vec{r}_o - \vec{r}_{sun})}{||\vec{r}_o - \vec{r}_{sun}||^3} + \frac{\vec{r}_{sun}}{||\vec{r}_{sun}||^3}\right] \qquad (6.15)$$

where G is the gravitational constant, M_{sun} is the mass of the Sun and the vectors $\vec{r}_{sun}$ and $\vec{r}_o$ were defined in the previous section.

CHAPTER

VALIDATION OF THE MMX HIGH FIDELITY PROPAGATOR

After having presented the Equations of Motion, the reference frames and the perturbation models being used in the MMX High Fidelity Propagator, it is necessary to verify that everything has been derived and coded correctly and that the propagator does produce valid results. To that end, it was decided that several test cases would be analyzed and the results compared with those obtained with *AGEX*, a propagator developed by Lamberto Dell'Elce which was used to obtain the results available in reference [38]. The reader will now find information regarding how the *AGEX* propagator was modified to model the Mars-Phobos system and the comparison of the results obtained for the different cases.

7.1 Modifications introduced in the *AGEX* propagator

The *AGEX* propagator was originally developed with the objective of modelling the perturbed dynamics that a mission such as *AIDA* would encounter in the environment of the Didymos system, a binary asteroid composed of a primary body (Didymos) and a small moon (Didymoon). In order to do so, the perturbed restricted three body problem is considered, and the spacecraft dynamics are modelled in a Co-rotating frame (denoted as $CO - ROT$) centered at the barycenter of the system, with the Z-axis parallel to the pole of the system, the X-axis pointing outwards and the Y-axis completing the triad, as shown in Figure 7.1 below.
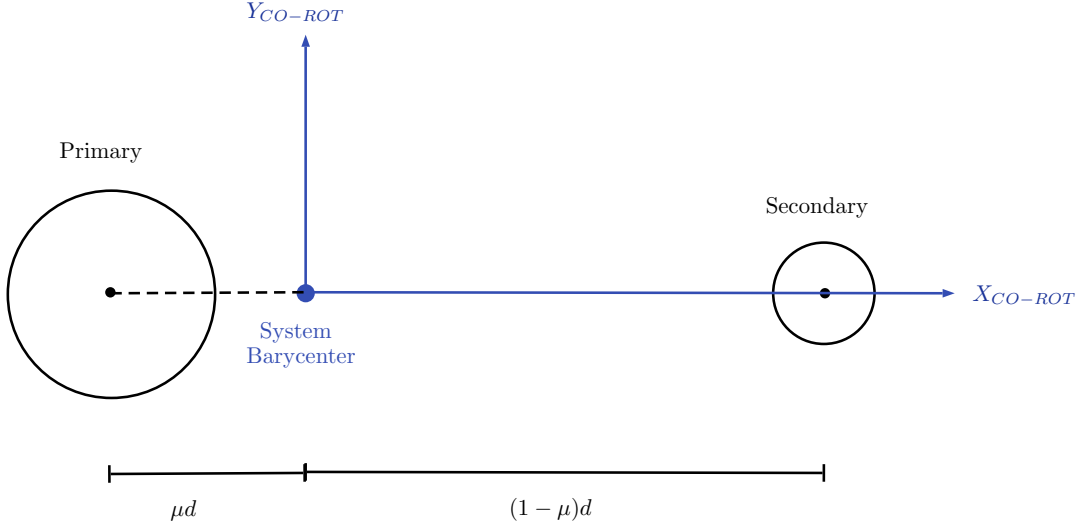
Figure 7.1: Graphical representation of the Co-rotating frame used in the AGEX propagator. The Z-axis points out of the paper.

In such frame, the spacecraft trajectory can be obtained using the following set of equations [38]

$$
\begin{aligned}
&\ddot{x} - \ddot{u}y - 2\dot{u}\dot{y} = \dot{u}^2 x - \frac{(1-\mu)(x+\mu d)}{r_1^3} - \frac{\mu[x-(1-\mu)d]}{r_2^3} + P_x \\
&\ddot{y} + \ddot{u}x + 2\dot{u}\dot{x} = \dot{u}^2 y - \frac{(1-\mu)y}{r_1^3} - \frac{\mu y}{r_2^3} + P_y \\
&\ddot{z} = -\frac{(1-\mu)z}{r_1^3} - \frac{\mu z}{r_2^3} + P_z
\end{aligned}
\tag{7.1}
$$

where u denotes the argument of latitude, d, r_1 and r_2 are the distances between the barycenters of the two bodies and between the spacecraft and each body respectively and P is the perturbation vector [38]. For the dynamics of the two bodies, *AGEX* considers a two-body model developed by McMahon and Scheeres (available in reference [47]) which assumes that the spin of the bodies is parallel to the orbital momentum and that d, u and ϕ (the libration of the secondary) are the three parameters describing their relative orbits, so that the EoMs are [38] :

$$\ddot{d} = \left(\frac{K - I_{2,z}\dot{\phi}}{I_{2,z} + \mu d^2}\right)^2 d - \frac{1}{\mu}\frac{\partial V}{\partial d}$$

$$\ddot{\phi} = 2\frac{K - I_{2,z}\dot{\phi}}{I_{2,z} + \mu d^2}\frac{\dot{d}}{d} - \left(\frac{1}{\mu d^2} + \frac{1}{I_{2,z}}\right)\frac{\partial V}{\partial \phi} \qquad (7.2)$$

$$\dot{u} = \frac{K - I_{2,z}\dot{\phi}}{I_{2,z} + \mu d^2}$$

As can be seen in Equation 7.2, the expressions depend on terms involving moments of inertia and a libration angle which are not found in the MMX High Fidelity propagator. Therefore, in order to consider the dynamics but at the same time be as close as possible to the model being used in the MMX High Fidelity propagator, it was decided that the equations of motion of both the spacecraft and the bodies were to be changed. In particular, the orbit of Phobos was simplified to use the well-known two-body orbit formulas, namely

$$d = \frac{p}{1 + e\cos\theta} \qquad (7.3)$$

$$\dot{d} = \frac{d^2}{p}e\sin\theta\,\dot{\theta} \qquad (7.4)$$

$$\ddot{d} = \frac{e}{p}\left(2d\dot{d}\sin\theta\,\dot{\theta} + d^2\cos\theta\,\dot{\theta}^2 + d^2\sin\theta\,\ddot{\theta}\right) \qquad (7.5)$$

where the first and second time derivatives of the true anomaly are the angular velocity and acceleration of the body respectively. These two variables can be obtained by means of

$$\dot{\theta} = \frac{h}{d^2} \qquad and \qquad \ddot{\theta} = \frac{-2\dot{\theta}\dot{d}}{d} \qquad (7.6)$$

where the angular momentum is constant and equal to $h = \sqrt{\mu_M p}$. With respect to the equations of motion of the spacecraft, they were modified in order to change the dependence on the argument of latitude for a dependence on the true anomaly. Also, since the MMX High Fidelity propagator uses the LVLH frame for the integration of the spacecraft trajectory, it is convenient to introduce this frame into AGEX and define the new EoMs in it. Note that the difference between the CO-ROT and LVLH frames reduces to their origins and to the direction of their Z-axes, since Z_{LVLH} is perpendicular to the orbital angular momentum

and Z_{CO-ROT} is assumed to be parallel to the pole of the primary. A procedure similar to the one found in reference [28] can be followed in order to derive the new expressions for the spacecraft EoMs in the LVLH frame, which are

$$\ddot{x} - 2\dot{\theta}\left(\dot{y} - y\frac{\dot{d}}{d}\right) - x\dot{\theta}^2 - \frac{\mu_M}{d^2} = -\frac{\mu_M}{r_1^3}\left(x + d\right) - \frac{\mu_P}{r_2^3}x + P_x$$

$$\ddot{y} + 2\dot{\theta}\left(\dot{x} - x\frac{\dot{d}}{d}\right) - y\dot{\theta}^2 = -\frac{\mu_M}{r_1^3}y - \frac{\mu_P}{r_2^3}\,y + P_y \tag{7.7}$$

$$\ddot{z} = -\frac{\mu_M}{r_1^3}z - \frac{\mu_P}{r_2^3}z + P_z$$

where all the variables have been defined previously in this section and throughout Equations 7.3 to 7.6. The expressions derived above are generic and therefore allow several cases to be analysed, from the simplest circular/elliptical restricted three body problems (CR3BP/ER3BP) to more complex models in which perturbations are included. As a result, the validation process has been carried out in several stages, complicating the dynamical environment at each step. In the next sections the reader will find the corresponding results. Please note that in this chapter, for the sake of clarity, plots related to the spacecraft will be shown in blue while those related to Phobos will be plotted in black.

7.2   Circular Restricted Three Body Problem

The simplest case to start with is the CR3BP, a restricted three body problem characterized by being unperturbed (hence $f = 0$) and by the fact that the orbit of the secondary is circular, which therefore implies that the angular velocity of Phobos is equal to its mean motion and that the angular acceleration is zero. To carry out the corresponding simulations a new set of MMX initial conditions was provided by Nicola Baresi for the CR3BP framework, from where a QSO of approximately 30×50 km was selected. In addition, the propagation time was set to be equal to 15 orbital periods of the spacecraft, which for the QSO being used corresponds to approximately 88 hours. Many plots can be obtained regarding different variables but, for simplicity, in the CR3BP case only the position differences and the Jacobi constant will be provided. Hence, Figure 7.2 below shows the norm of the error in the orbit of the spacecraft around Phobos and of the moon around Mars.
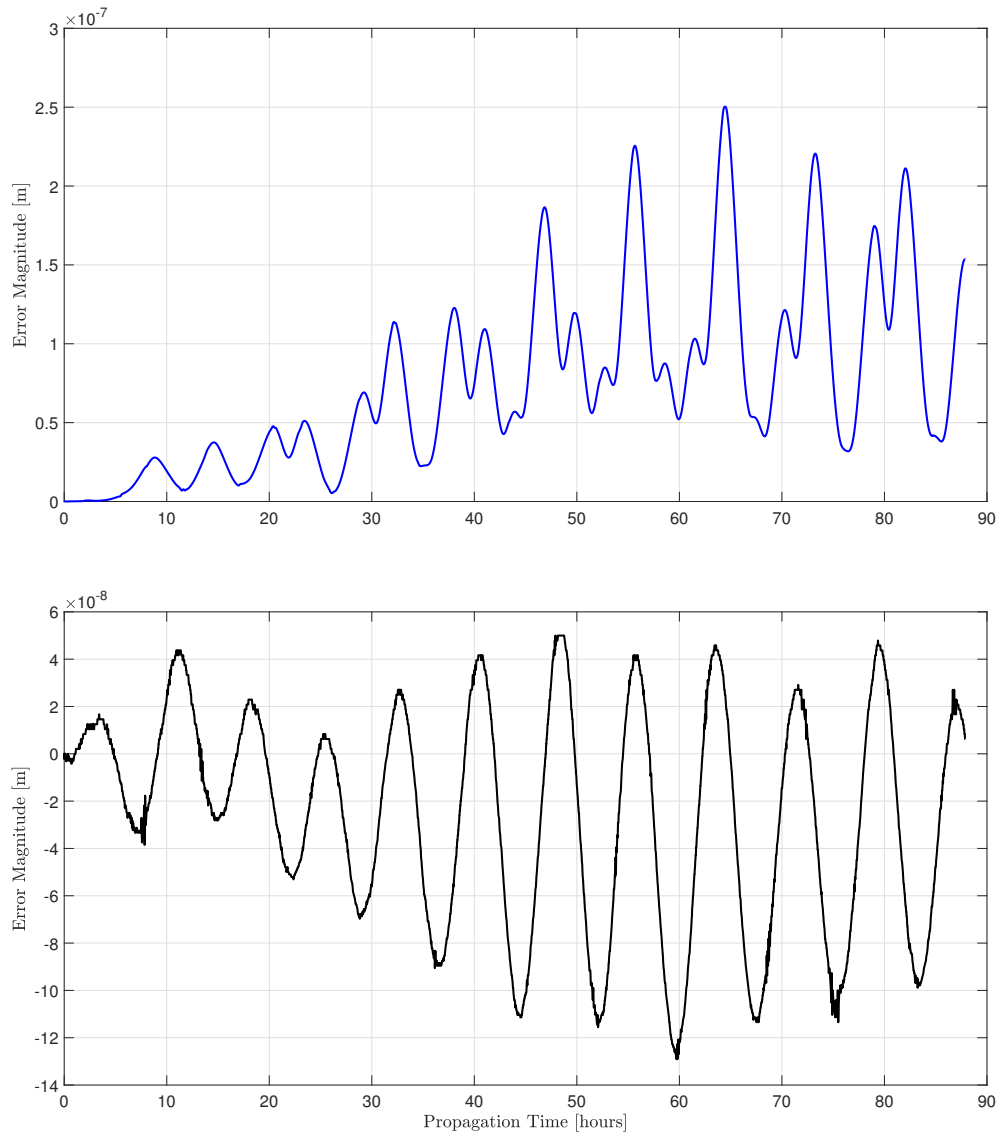
Figure 7.2: Norm, in meters, of the error in the orbits of MMX (top) and Phobos (bottom).

As can be appreciated in Figure 7.2 the accuracy desired for the propagation is satisfied in both orbits, since after 15 spacecraft orbital periods the norms of the separation are of the order of 0.3 micrometers for MMX and 60 nanometers for Phobos, meaning that the difference reduces to numerical errors. With respect to the Jacobi integral, it is known that for the CR3BP it should be conserved throughout the integration, a result which can be observed in Figure 7.3 below.

64
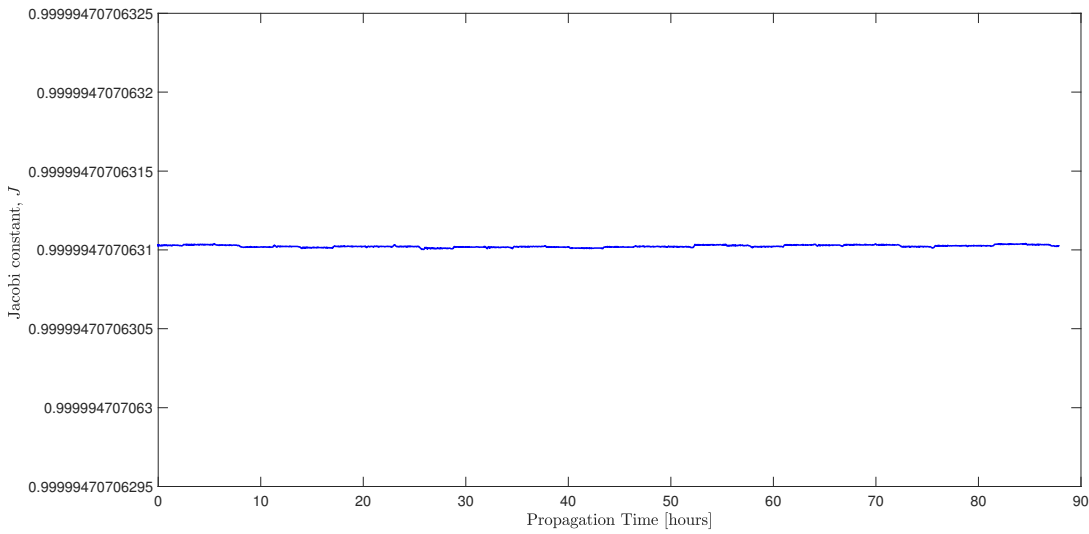
Figure 7.3: Plot of the Jacobi integral obtained in the MMX High Fidelity propagator.

7.3 Unperturbed Elliptical Restricted Three Body Problem

Having validated the CR3BP the next test case to consider is the elliptical restricted three body problem (ER3BP), where the motion of Phobos around Mars is now assumed to be an unperturbed elliptical orbit. To carry out the simulations, the 30×50 km QSO was considered and the initial true anomaly was defined to be θ_0, having been both values provided previously in Section 5.6. In addition, the integration time was defined to be equal to 10 orbital periods of Phobos around Mars. Figure 7.4 below presents the error obtained for the propagation of the spacecraft and the moon's orbit.
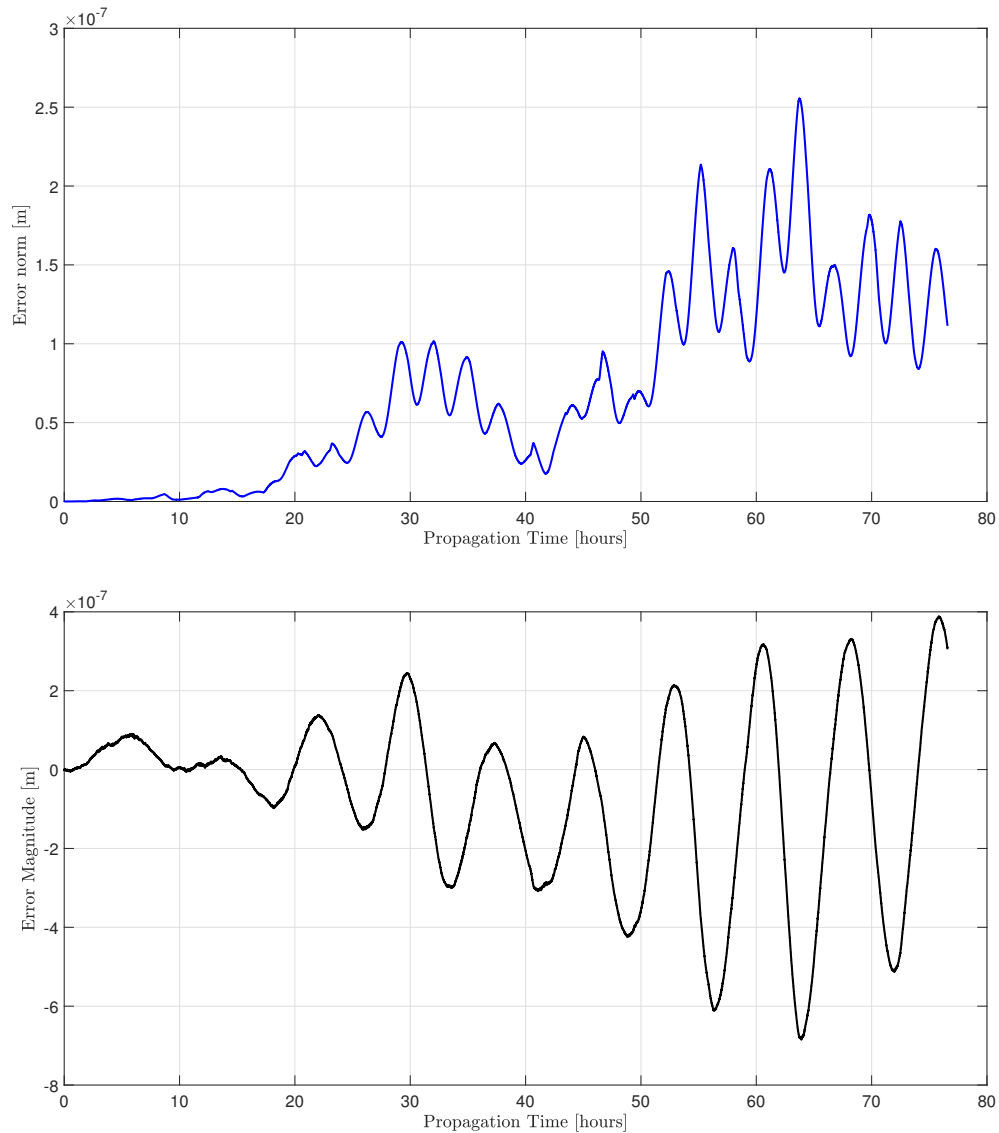
Figure 7.4: Error, in meters, in the orbits of MMX (top, in blue) and Phobos (bottom, in black) for the ER3BP case.

Similarly to the CR3BP, the error at the end of the propagation is of the order of 0.3 micrometers for MMX. In contrast, the difference in the orbit of Phobos does increase, being now of 0.4 micrometers. The reason behind this is simply that the numerical errors intrinsic to the MATLAB computations become greater when the orbit is shaped as an ellipse, since the distance between the primaries (d) and the angular velocity are no longer equal to 1 (in normalized units). In any case, the angular velocity and acceleration should satisfy that both are perpendicular to the Phobos orbital plane (hence directed in the Z_{LVLH} direction) and

66

that their magnitude is equal to that given by Equation 7.6. This result can be observed in Figure 7.5 below.
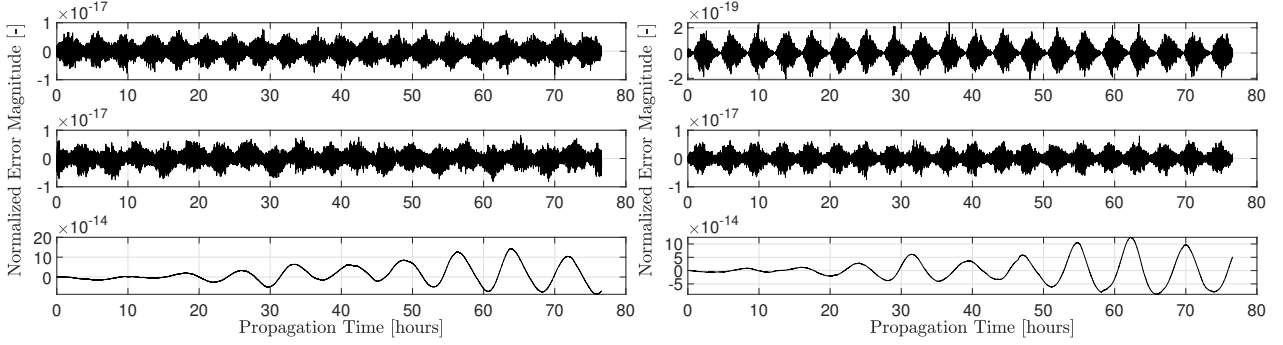
Figure 7.5: Normalized errors in the angular velocity (left plot) and angular acceleration (right plot). The components are expressed in the LVLH frame and correspond to the X direction (top), Y direction (middle) and Z direction (bottom).

In particular, in the X_{LVLH} and Y_{LVLH} directions it is clear that the errors are simply numerical, being caused by the fact that in the MMX High Fidelity propagator the vectors involved in the computations (recall Equations 5.25 and 5.27), are expressed originally in the MCI frame and have to be transformed to the LVLH, being this rotation the one inducing the differences. With respect to the components in the Z-axis, the error is very small, of the order of 10^{-14}, and it is caused by the definitions of the angular momentum and its time derivative. In *AGEX*, the former is a constant value that depends only in μ_M and p while the latter is directly set to zero, since there is no out of plane motion in the ER3BP. On the other hand, in the MMX High Fidelity propagator the values are computed at each time step as $\vec{h} = \vec{r}_p \times \dot{\vec{r}}_p$ and $\dot{\vec{h}} = \vec{r}_p \times \ddot{\vec{r}}_p$, causing a dependence on time-varying vectors which are obtained after a series of rotations and mathematical operations which induce very small errors in those terms, as can be seen in Figure 7.6 below.
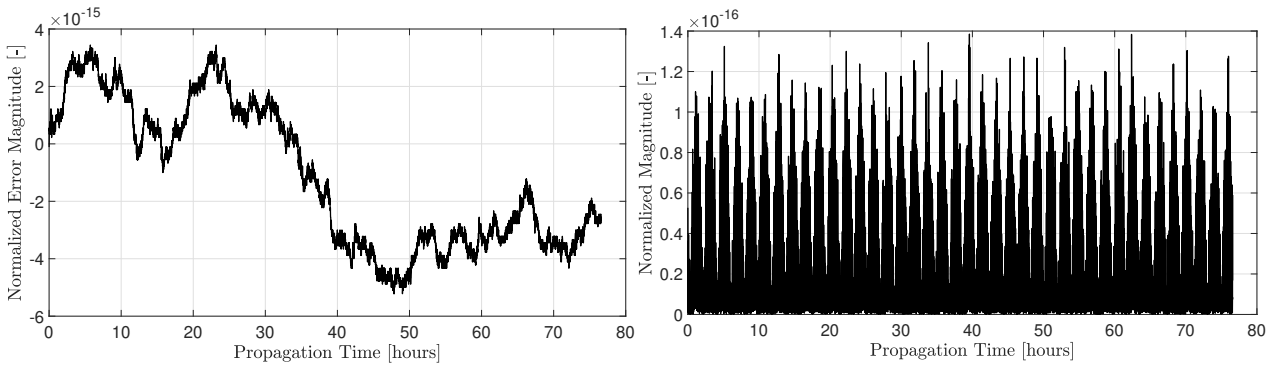
Figure 7.6: Normalized errors in the norm of the angular momentum (left) and its time derivative (right).

To further justify the idea explained above, the dynamical perturbation and its time derivative can be verified, since both appear in the expressions for the angular velocity and acceleration. For the ER3BP, both vectors should be zero and this is the case with the values obtained in the MMX High Fidelity Propagator, as can be seen in Figure 7.7 below. Hence, it can be concluded that the propagator is accurate under the ER3BP conditions.
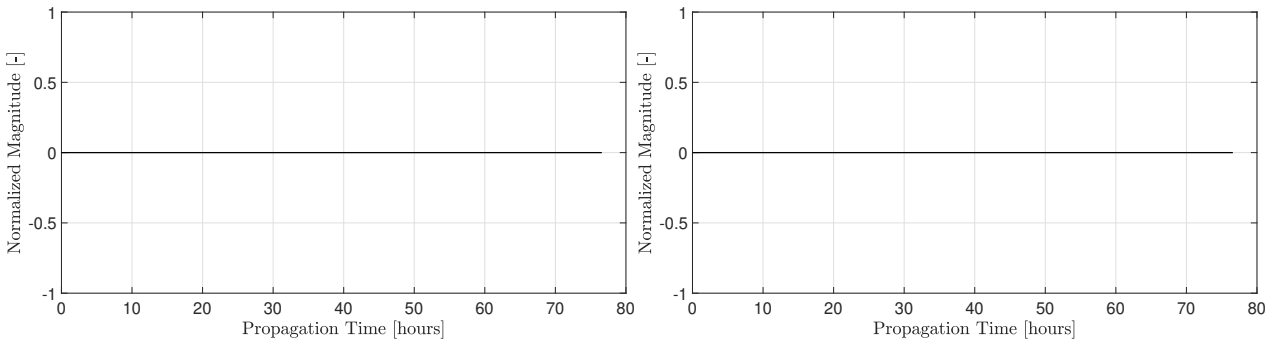
Figure 7.7: Normalized magnitude of the dynamical perturbation (left) and its time derivative (right) obtained in the MMX High Fidelity propagator for the ER3BP case.

7.4   Perturbed Elliptical Restricted Three Body Problem

Having proved that the MMX propagator yields consistent results in the unperturbed cases, the next stage in the validation process is the inclusion of the perturbations described previously in Chapter 6. First, the polyhedron model is introduced into the propagator to account for the irregular geometry of Phobos, and afterwards solar radiation pressure and gravitational attraction are taken into account.

7.4.1 Polyhedral Phobos

To obtain the results shown in this section, the propagators were provided with the same set of initial conditions as the ones used for the unperturbed ER3BP case. Similarly, the integration time was kept equal to 10 orbital periods of Phobos. However,to use the polyhedral model in *AGEX* a small adaptation had to be performed.

In particular, as the reader can find in the appendix of reference [38], the rotation matrix to express vectors in the secondary body frame (denoted as B_2 and which is considered to point in the direction of the minimum, medium and maximum moments of inertia of the tri-axial ellipsoid originally used in *AGEX*) depends on the libration angle ϕ, which here is assumed to be equal to zero. Hence, setting $\phi = 0$ causes the B_2 frame to be coincident with the CO-ROT frame, so that it points as shown in Figure 7.1. However, this causes a conflict since the spacecraft position vector has to be introduced into the polyhedral model in the PCPF frame, as explained in Section 6.2.2, implying that the rotation matrix defined in *AGEX* has to be modified. This can be done by noticing that the CO-ROT frame and the LVLH frame have parallel X and Y axes. Hence, rotating from CO-ROT to PCPF is the same as rotating from LVLH to PCPF. As a result, the modification to be introduced is simply a 180°rotation about the Z axis, as explained in Section 4.4. The results for the error in the Phobos and MMX trajectories are found in Figure 7.8 below.
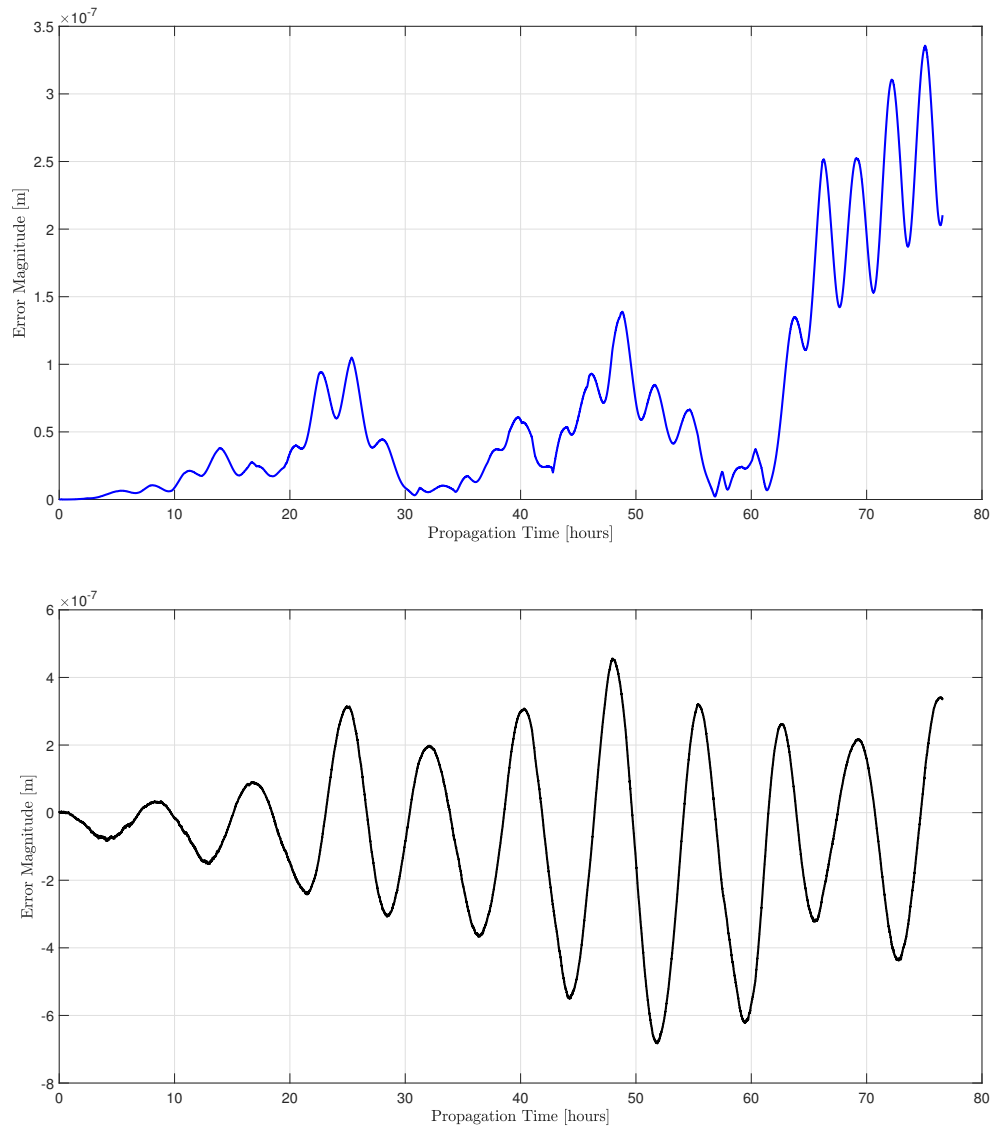
Figure 7.8: Error, in meters, for MMX (top, in blue) and Phobos (bottom, in black) for the case in which Phobos is modelled as a constant density polyhedron.

As can be appreciated in Figure 7.8, for the Phobos orbit the same error as in the ER3BP case is obtained, with the difference in the oscillatory behaviour being caused by the numerical errors intrinsic to the computation. This is indeed expected, since in this case what is being perturbed is the spacecraft trajectory and not the Phobos orbit. With respect to the trajectory of MMX, the error is approximately 0.1 micrometers during the first 60 hours of propagation, and eventually experiences a peak at the end. However, the maximum magnitude is approximately 0.34 micrometers, so the trajectory is obtained precisely. Further

verifications can be conducted by looking at the gravity acceleration that Phobos exerts on the spacecraft, shown in Figure 7.9.
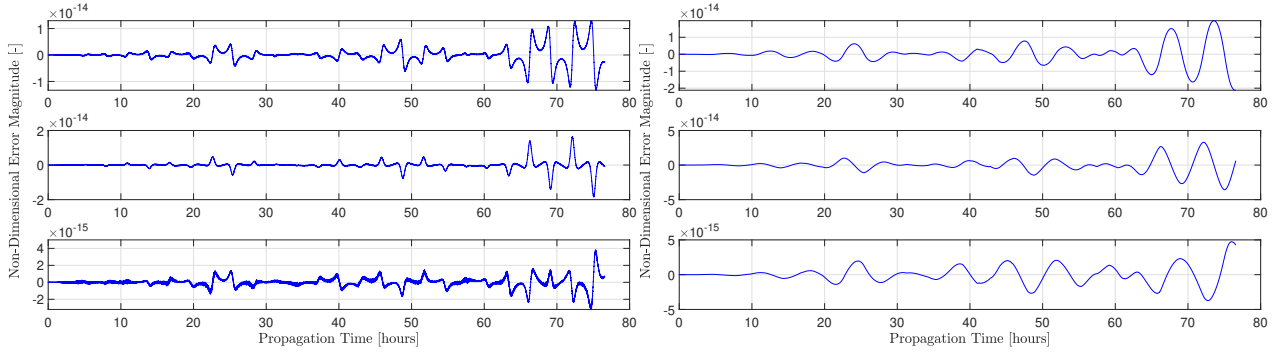
Figure 7.9: Left plot: normalized error between *AGEX* and the MMX High Fidelity propagator in the gravity acceleration caused by Phobos on the spacecraft. Right: normalized error in the Phobos to MMX vector. Top, middle and bottom represent the X,Y and Z components respectively in both graphs.

In particular, the left plot shows that the error in the gravity components is very small throughout the propagation, and by considering the right plot it can be seen that those oscillations are produced by small differences found in the Phobos to MMX vector. Furthermore, the gravity yielded by the polyhedron model can be compared with the acceleration that would be obtained if the same Phobos - MMX position vectors were used and Keplerian gravity was considered. It is found that the mean relative errors in the X,Y and Z directions expressed as a percentage are 1.48%, 2.92% and 11.94% respectively. Although the value for the percentage difference in the Z direction is considerable, it can be justified by recalling that Phobos is an oblate ellipsoid and that therefore the flattening at the poles causes a divergence with respect to the perfect sphere considered when obtaining Keplerian gravities. Figure 7.10 below shows the mentioned oblateness, where it is visible that the poles of Phobos present a divergence of up to 2.5 km from the perfect sphere. Hence, with these results it can be concluded that the polyhedron model has been correctly implemented in the MMX High Fidelity propagator.
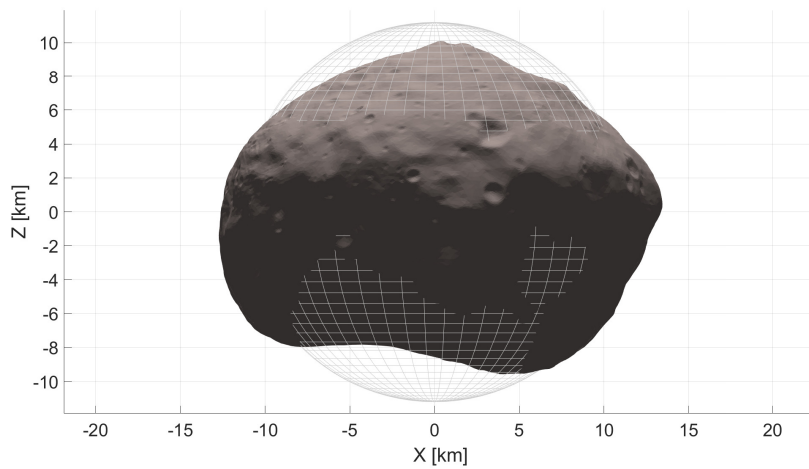
Figure 7.10: Graphical representation of the geometry and dimensions of the polyhedral Phobos compared to a perfect sphere of radius equal to the intermediate semi-major axis of the moon (11.2 km), represented in light grey.

7.4.2   Solar Radiation Pressure

The second perturbation to introduce is the solar radiation pressure. For this validation, the same initial conditions and propagation time as the ones used in the previous test case are considered. Similarly to what happened with the introduction of the polyhedron, small adaptations have to be configured in the propagators. In particular, in the MMX High Fidelity propagator the value of the radiation intensity S and of the latitude and longitude of the pole of the MCI frame must be set constant, as that is how they are considered in *AGEX*. With these changes, the error in the SRP perturbing acceleration that is obtained is shown in Figure 7.11 below, together with the value of the perturbation as obtained in the MMX High Fidelity propagator.
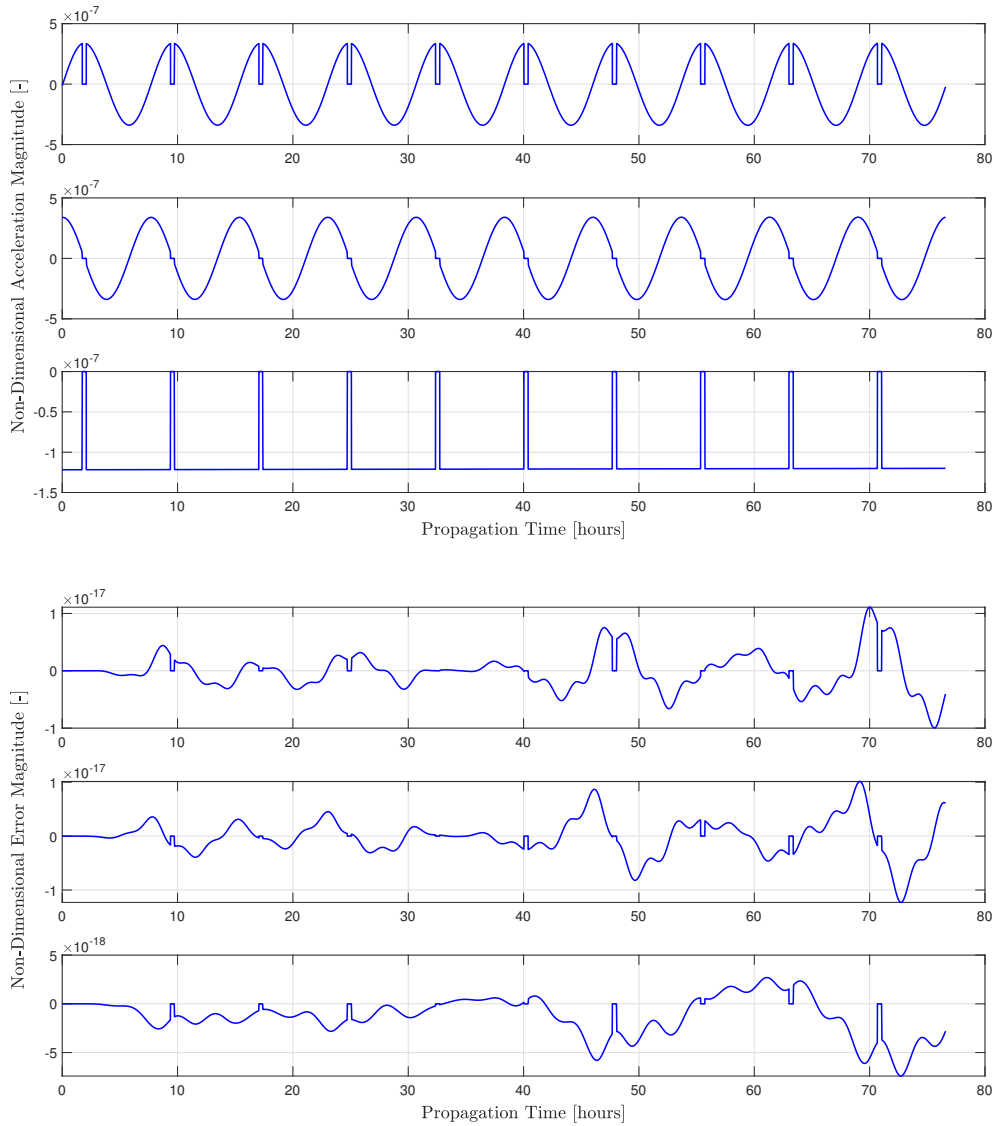
Figure 7.11: Top: Perturbing acceleration due to solar radiation as obtained in the MMX High Fidelity propagator. Bottom: Normalized error in the components of the SRP when compared with the results from AGEX.

As can be seen in Figure 7.11, the error between the values yielded by the MMX propagator and those coming from AGEX is negligible, since it is of the order of 10^{-17} in normalized units. Furthermore, the top plot shows the expected behaviour for the SRP, as the eclipses can be distinguished every 7.65 hours, which is the time corresponding to the orbital period of Phobos around Mars. The duration of the eclipses, approximately 22 minutes, is in accordance with the values found in reference [48]. The bottom plot also shows that the error

between the SRP accelerations is zero whenever eclipse conditions are found, therefore proving that the eclipse model described in Section 6.3 has been correctly implemented.

7.4.3 Solar Gravitational Perturbation

Finally, the perturbing acceleration caused by the gravitational attraction of the Sun is introduced. Using the same initial conditions, integration time and modifications as in the SRP case, the error in this perturbing acceleration is given in Figure 7.12. As the reader can observe, it is of the order of 10^{-15} in normalized units, therefore proving that the model has been correctly implemented in the propagator.
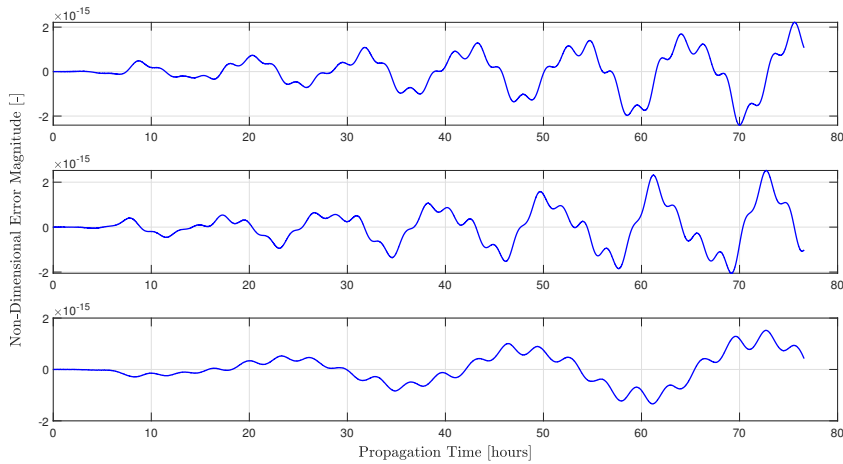
Figure 7.12: Error in the perturbing acceleration caused by the gravitational attraction of the Sun. Top plot for the X-component, middle for Y and bottom for Z.

7.5 Spherical Harmonics

Finally, the spherical harmonic model characterizing the Martian gravity is the last perturbation to be included in the propagator. Validating this acceleration cannot be done with the *AGEX* model, and hence a different alternative has to be considered. In particular, a useful approach would be to compare the orbit of Phobos around Mars with the trajectory that can be retrieved from JPL software such as Horizon's or SPICE, which are characterized by providing high precision ephemerides for bodies through the so-called *JPL Development Ephemeris*. The latter is used, since it is available in the MATLAB environment, thus facilitating the implementation. The reader can find information about the SPICE software and the functions and kernels (sets of data) used in Appendix A.

To compare the results as accurately as possible with those obtained from SPICE the complete spherical harmonics are considered, hence accounting for degree and order up to 80. Figure 7.13 below shows the evolution of the norm of the error in the Phobos position.
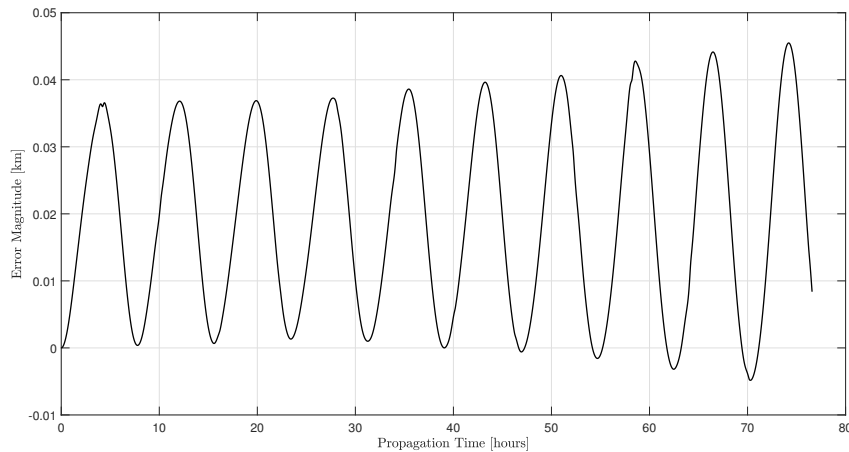
Figure 7.13: Error in the Phobos orbit between SPICE and the MMX High Fidelity propagator.

As can be appreciated, after 10 orbital periods of Phobos around Mars the maximum divergence between SPICE and the MMX High Fidelity propagator is of 0.04 km. Although the initial error is zero because the same state vector for the initial epoch is considered, the difference in the dynamical models used for obtaining the orbit of Phobos becomes evident as the propagation advances. In particular, SPICE not only considers the spherical harmonics of Mars but also takes into account the effect of all the other perturbing forces acting of Phobos, which are responsible for the mentioned drift. In any case, this result shows that the GMM3 model coefficients were organized and introduced correctly and that the Martian gravity is accurately obtained in the MMX High Fidelity Propagator.

Part III

RESULTS AND CONCLUSIONS

8

RESULTS FOR A LOW-ALTITUDE QSO

This chapter is now dedicated to the presentation and analysis of the results yielded by the MMX High Fidelity propagator for the 30 × 50 km Quasi-Satellite Orbit, which is characterized by having an orbital period of 5.803 hours. In particular, an analysis of the effect that the perturbations have on the orbit has been carried out. To do so, the elliptical three body problem values are taken as base case, and then perturbations are added gradually. Firstly, polyhedral Phobos is included, followed by SRP, solar gravity and finally the spherical harmonics of Mars.

The simulations were carried out considering a propagation time of 50 orbital periods of Phobos around Mars until spherical harmonics were introduced, when the time was reduced to 25 orbital periods due to the large computation time required for each simulation. In addition, an events function was used in order to stop the simulation if failure occurred, being this considered to take place whenever the spacecraft impacted Phobos or drifted away excessively.

8.1   Effect of non-spherical Phobos

As was shown in Figure 7.10, Phobos is an oblate body with a highly irregular shape and morphology. As a result, accounting for its non-sphericity is a must. Doing so, and comparing the results to the ER3BP case where it is considered as a perfect sphere yields valuable insight. To begin with, Figure 8.1 below presents a comparison in the position difference.
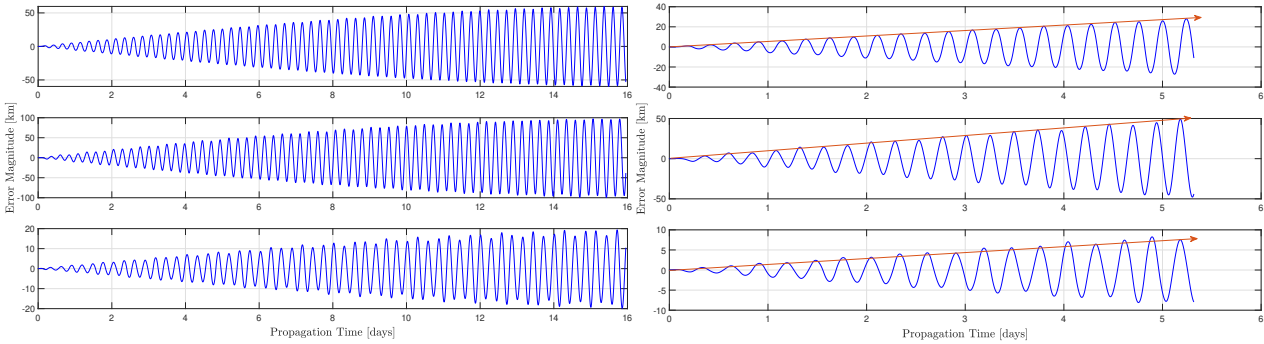
Figure 8.1: Difference in the MMX position components caused by the introduction of the polyhedral Phobos compared to when it is considered as a point mass. The left graph spans all the integration time, while the right one is a zoomed view accounting for 1/3 of that time. In each graph, the top, middle and bottom plots correspond to the X,Y and Z components respectively. The orange arrows are used to indicate rate of increase.

From Figure 8.1 one can observe how the introduction of the polyhedral Phobos causes a periodic variation in the MMX trajectory. In particular, the right plot shows that for the X and Y directions these variations have a period of approximately 5.8 - 6 hours, which corresponds with the orbital period of the spacecraft, and that the rate of increase of the oscillation is almost constant. These results vary in the case of the Z direction, where the oscillation period is of approximately 7 hours and the rate appears to change. In any case, as the propagation time increases (left graph) it can be observed that the magnitude of the oscillations grows slower than at the initial stages. Furthermore, it is noticeable that the difference produced along the Y-direction is bigger than in the X axis, with the ratio at the end of the propagation being $\Delta = \frac{\Delta Y}{\Delta X} = \frac{96.27}{58.22} = 1.654$. The variations therefore seem to correspond with the ratio between the major and minor axes of the epicycle, which is $50/30 = 1.667$.

The analysis of the effect of a polyhedral Phobos can continue by considering Figure 8.2 below, where the norm of the position vector is plotted for one third of the total propagation time with the objective of facilitating the visualization of the result.

78
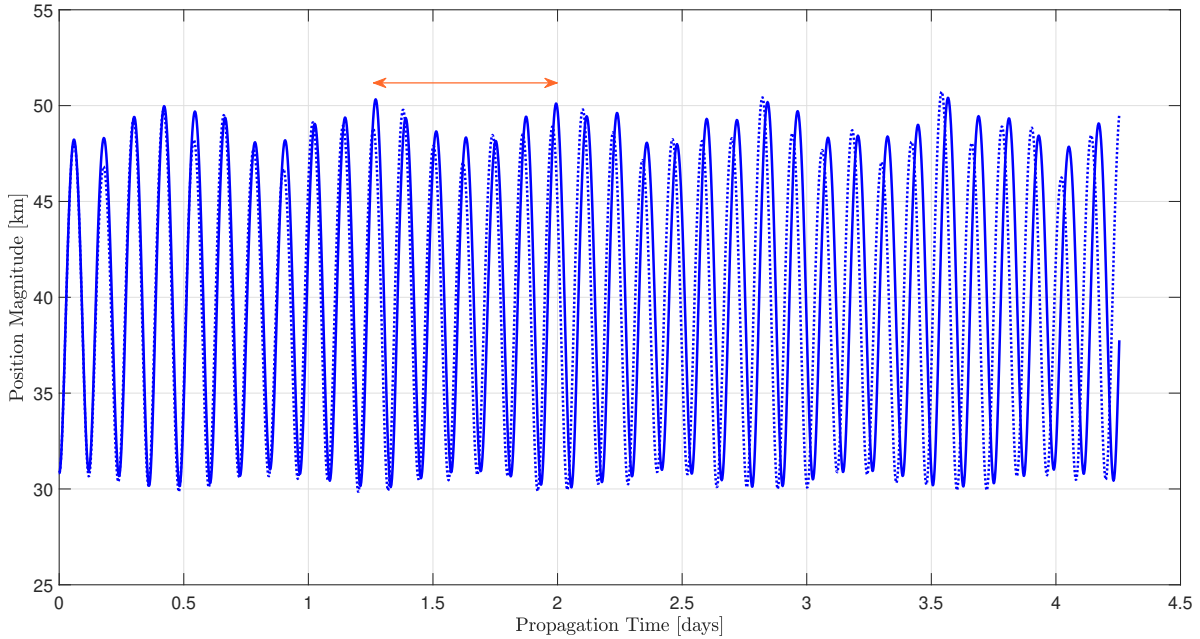
Figure 8.2: Plot of the norm of the MMX position vector in the LVLH frame. Continuous line represents the trajectory obtained with Phobos modelled as a point mass, while the dotted line corresponds to the trajectory obtained with the polyhedron.

As can be appreciated, distance to Phobos experiences big oscillations, with what appears to be periodic cycles contained in between two maximum amplitude oscillations. These cycles, as the one specified with the orange arrows, are characterized by having a period of 3 complete orbits of MMX around Phobos, so approximately occur every 17 hours. The results obtained in Figure 8.2 resemble those of reference [49], and hence it is possible that the variations observed in the magnitude of the oscillations are caused by the eccentricity of Phobos, as suggested by [49]. Similarly, the polyhedral Phobos appears to produce a "smoothing" effect on the drift of the epicycles, causing the spacecraft to be closer to the moon. In particular, the lower and upper bounds of the separation tend to be smaller for the case of a polyhedral Phobos in most of the MMX orbits. As a consequence of this, the distance covered by the spacecraft is reduced and this produces a shift in the graph which becomes very visible at the end of the propagation, where it can be seen that MMX has completed more orbits in the same amount of time. The aforementioned "smoothing" effect can also be seen in Figure 8.3 below, where it is clear that the passages of the MMX spacecraft (in red) are more contained and ordered, in contrast with the widely spread situation found if Phobos is assumed to be a point mass (in blue).

79
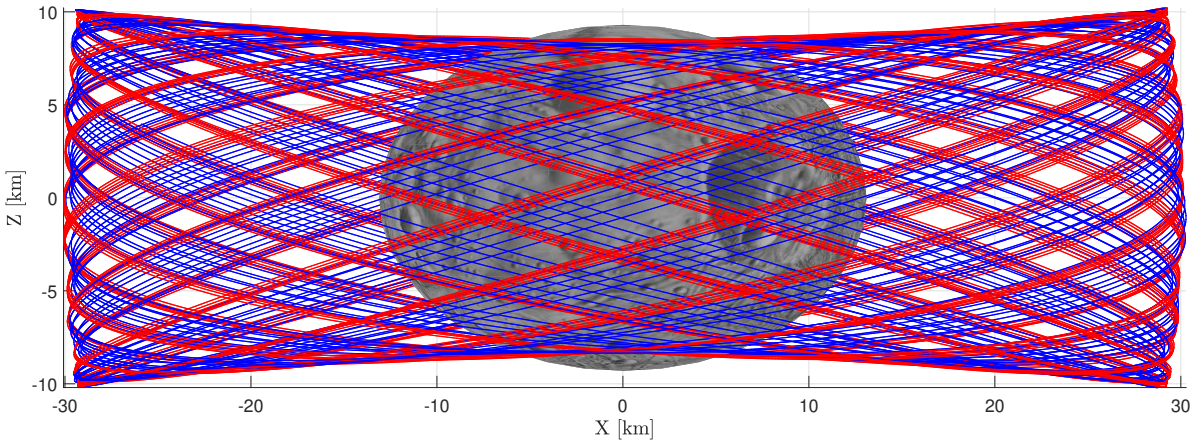
Figure 8.3: Trajectory of the MMX spacecraft as viewed perpendicular to the XZ plane of the LVLH frame. The trajectory in blue corresponds to the case in which Phobos is a point mass, while the red one is obtained with a polyhedral Phobos.

8.2 Effect of Solar Radiation Pressure

The next perturbing acceleration introduced into the propagator is the one caused by the solar radiation pressure, which is added to the previously introduced polyhedron. The effect that this term has on the MMX trajectory can be seen in Figure 8.4 below.
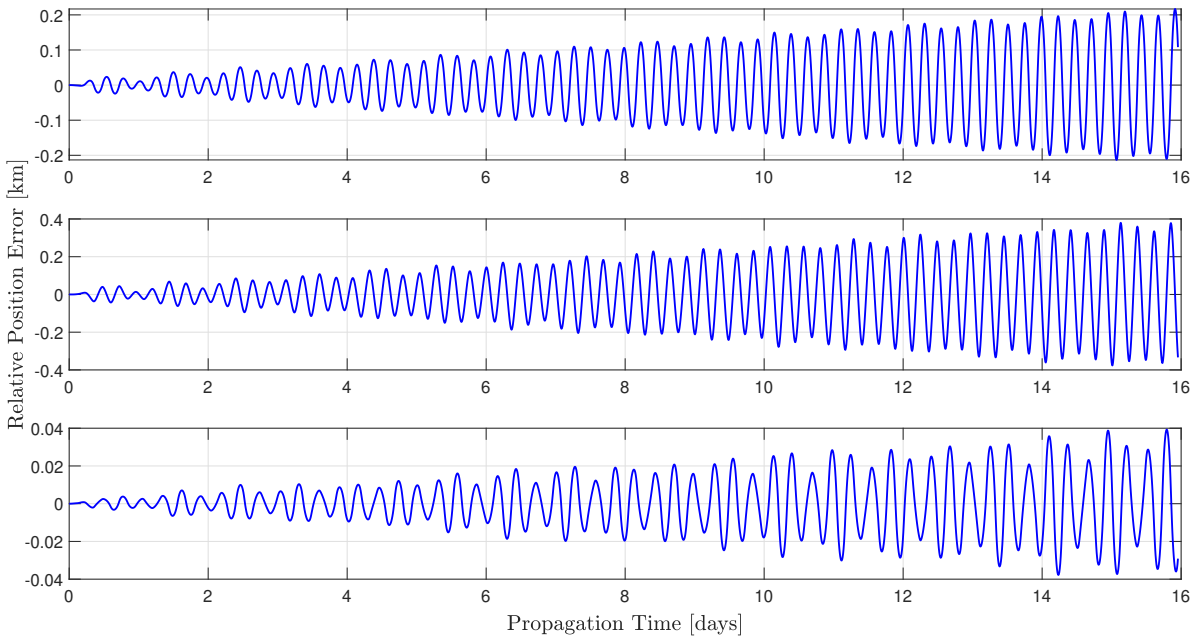
Figure 8.4: Difference in the position of the MMX spacecraft between the model accounting only for the polyhedral Phobos and the model in which SRP is also included.

As can be appreciated, the effect of SRP on the trajectory is small. After 16 days, the error is of the order of 108.11 meters in X and 333.53 meters in Y, which represents a 0.42 % and 1.6 % variation respectively when compared to the trajectory without SRP. This result is based on the fact that the magnitude of the perturbing acceleration due to SRP is very small. Mean values of the SRP acceleration components are presented in Table 8.1 below, together with the average eclipse duration.

	a_{SRPx} (m/s^2)	a_{SRPy} (m/s^2)	a_{SRPz} (m/s^2)	Eclipse duration (mins)
Magnitude	9.259×10^{-10}	2.507×10^{-10}	8.900×10^{-9}	21.86

Table 8.1: Mean values of the SRP acceleration expressed in the LVLH frame and mean eclipse duration.

8.3 Accounting for Sun gravity

Introducing the perturbing acceleration caused by the solar gravity produces an even smaller impact on the trajectory, as shown in Figure 8.4 below.

Figure 8.5: Difference in the position of the MMX spacecraft between the model accounting for non-spherical Phobos and SRP and the model in which Sun gravity is also included.

In particular, after 16 days the magnitude of the difference is of the order of 10 meters in the Y direction, and even smaller in X and Z with 5 and 1 meter respectively. Such results is

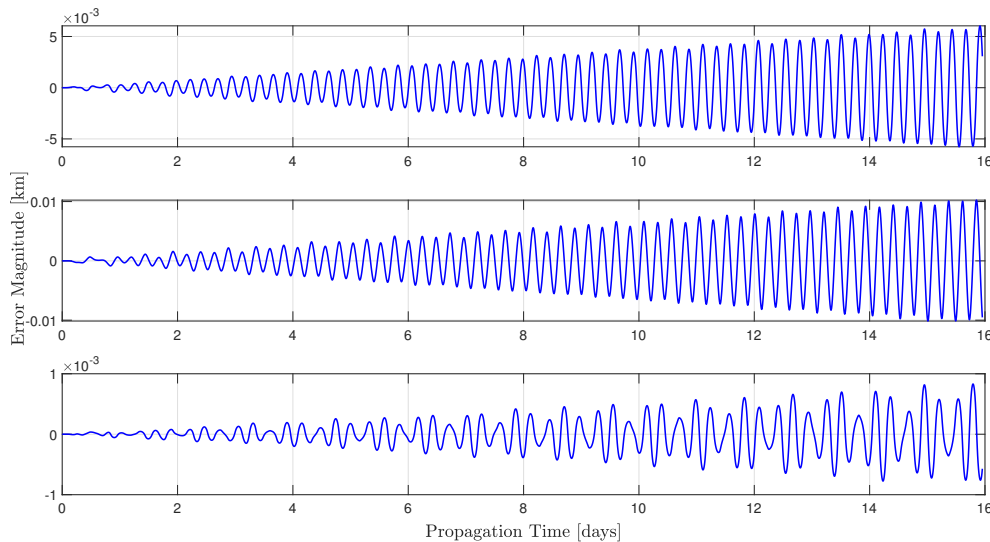indeed expected since the perturbing acceleration caused by the Solar gravity is very small. Mean values for this term are provided in Table 8.2, along with the mean distance to the Sun.

	a_{gxS} (m/s^2)	a_{gyS} (m/s^2)	a_{gzS} (m/s^2)	Mean Sun distance (km)
Magnitude	2.011×10^{-12}	3.710×10^{-12}	6.622×10^{-12}	$2.412447788182735 \times 10^8$

Table 8.2: Mean values for the solar gravity acceleration expressed in the LVLH frame and mean Mars-Sun distance.

8.4   Analysis of the effect of Mars Spherical Harmonics

The perturbations analyzed in the previous sections affected the spacecraft but not the dynamics of Phobos as it orbits Mars. The spherical harmonic model must therefore be introduced since it is expected to greatly affect the MMX trajectory, as was pointed out in Figure 3.1. Please note that hereafter the notation used to refer to the spherical harmonics model will be $SH_{D,O}$, where D corresponds to the degree and O to the order. For clarity, the notation $SH_{D,O}$ refers to the spherical harmonics model which has included all the coefficients up to degree D and order O. To refer to an specific Stokes coefficient, the notation used will be $C_{D,O}$ or $S_{D,O}$.

8.4.1   Convergence Study

Since the GMM3 model being considered includes coefficients up to degree and order 80, it is first necessary to carry out a convergence study so as to determine which orders and degrees are relevant for the analysis. Once this has been defined, a profound study can be carried out to determine the effect of those coefficients.

To that end, MMX trajectories were obtained considering different spherical harmonic combinations. In particular, the following were taken into account: $SH_{2,2}$, $SH_{3,3}$, $SH_{4,4}$, $SH_{5,5}$, $SH_{6,6}$, $SH_{7,7}$, $SH_{8,8}$, $SH_{10,10}$, $SH_{12,12}$, $SH_{15,15}$, $SH_{20,20}$, $SH_{25,25}$, $SH_{30,30}$ and $SH_{35,35}$. Greater focus was placed in the lower orders and degrees because this is the region where the differences were expected to be greater. The resulting orbits were then compared to the "reference" trajectory, which was selected to be the one found with the Perturbed ER3BP model which included polyhedral Phobos, SRP and Sun gravity (Section 8.3). Doing so, the mean relative position error (in percentage) with respect to the aforementioned reference trajectory could be obtained and plotted, showing after which of the above combinations

the error stopped experiencing important variations. The results are presented in Figure 8.6 below, with Figure 8.7 being a zoomed view to better appreciate the behaviour.
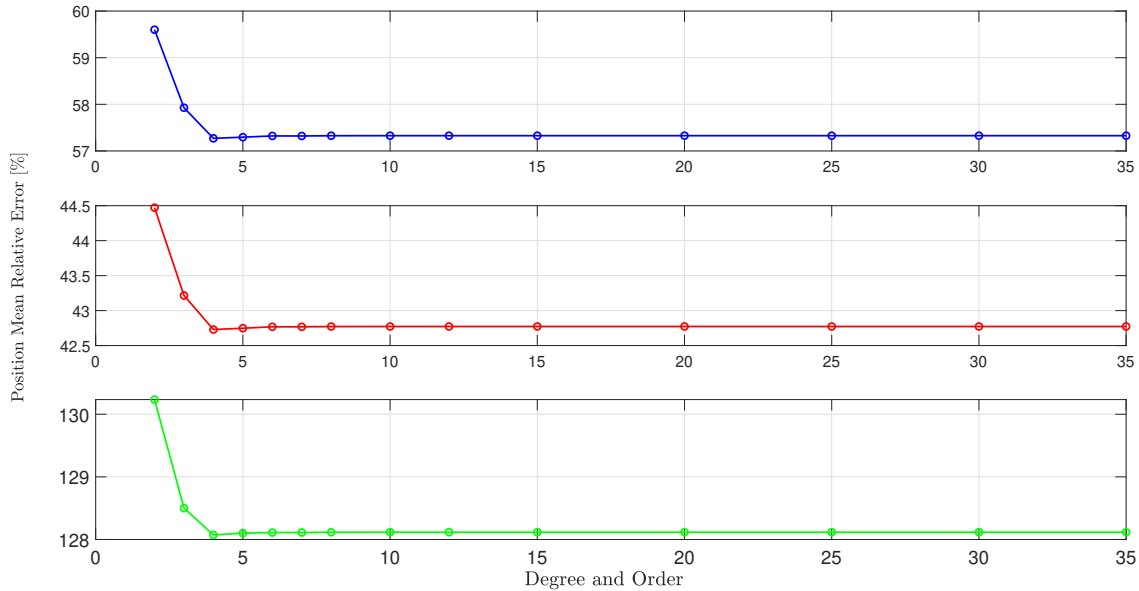
Figure 8.6: Convergence analysis for the 30 × 50 km QSO. The mean relative error in the MMX trajectory is obtained for a total of 14 different combinations of spherical harmonics which have the same order and degree (SH$_{2,2}$,SH$_{3,3}$,SH$_{4,4}$ etc). The trajectory considered as base case is the one obtained in the perturbed ER3BP of Section 8.3. Each point corresponds to the mean error between the reference trajectory and the corresponding SH trajectory. Top plot for X component, middle for Y and bottom for Z.
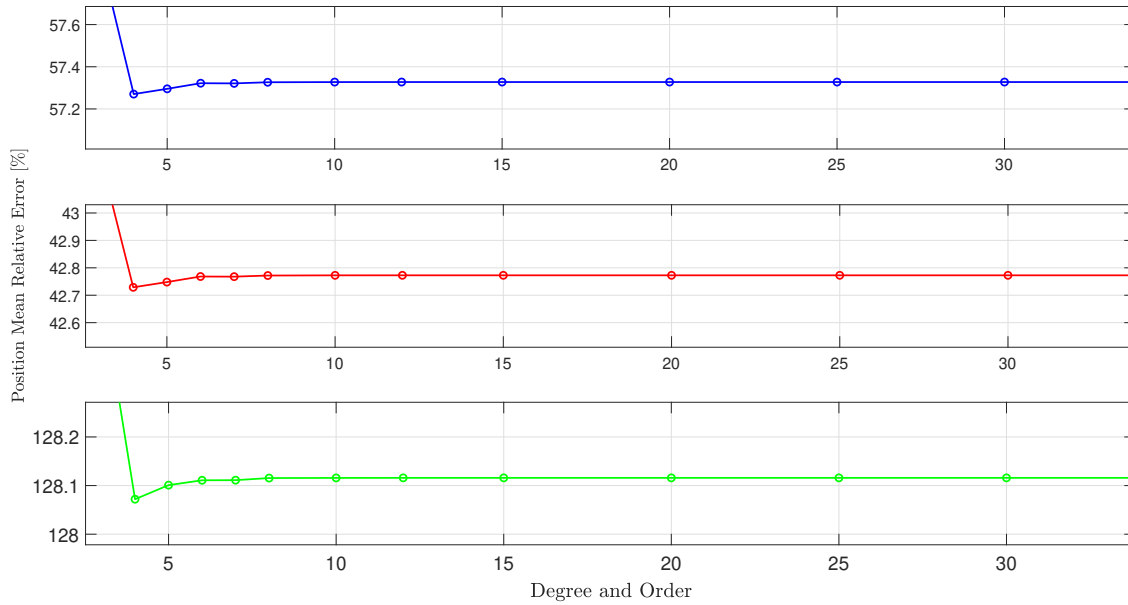
Figure 8.7: Zoomed view of the convergence analysis presented in Figure 8.6. Top for X component, middle for Y and bottom for Z.

Figure 8.6 shows that the relative error with respect to the reference trajectory experiences a big variation when the spherical harmonics are taken into account, thus confirming the hypothesis presented earlier in Figure 3.1 that the non-uniform Martian gravity field causes strong effects on the MMX trajectory. In addition, Figure 8.7 shows that the effect is, as expected, mainly caused by the lower orders and degrees. In particular, it is possible to see that after the value corresponding to $SH_{8,8}$ the error stabilizes and forms a plateau. As a result, in order to analyse the relevant effects of the Martian non-uniform gravity it appears that considering spherical harmonics up to degree and order 8 is sufficient. To ensure this claim, the relative mean error between the trajectory corresponding to $SH_{8,8}$ and the greater orders and degrees is computed for each position component, with the results being found in Figure 8.8.
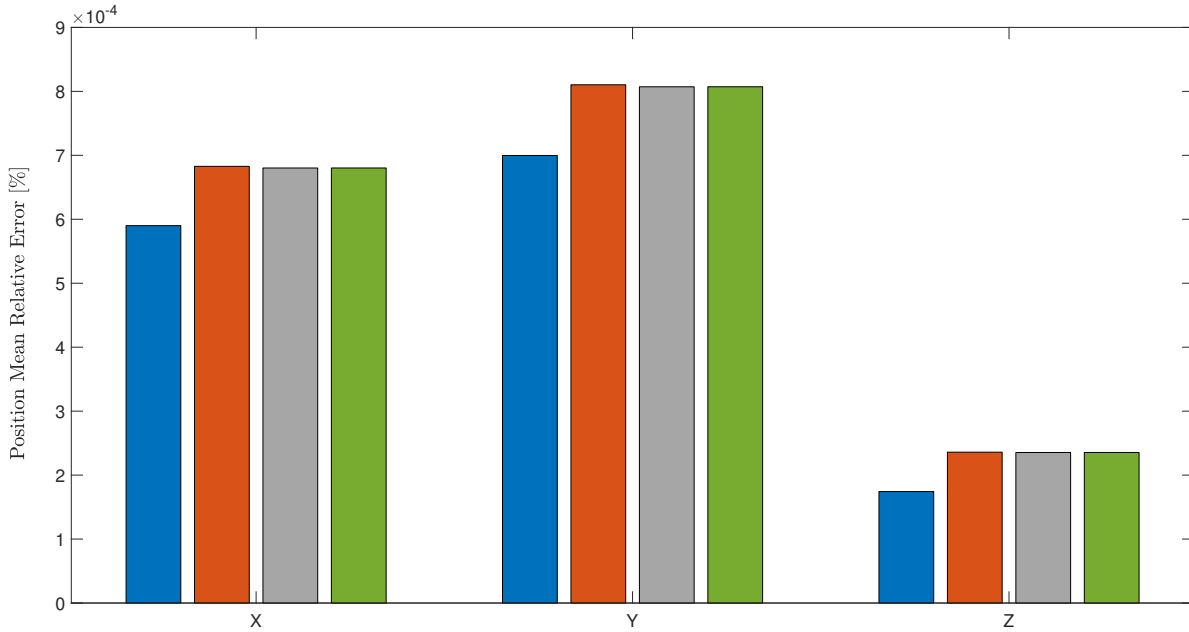
Figure 8.8: Position mean relative error in the X (left), Y (middle) and Z (right) components for the MMX trajectory. The case with degree and order 8 is taken as reference. The columns in each data set represent, from left to right, the error between $SH_{8,8}$ with $SH_{10,10}$ (in blue), $SH_{15,15}$ (in orange), $SH_{20,20}$ (in grey) and $SH_{30,30}$ (in green).

As shown in Figure 8.8, the mean relative error obtained when comparing the trajectories of $SH_{8,8}$ and $SH_{30,30}$ is, in the biggest case, equal to 0.0009 %. As a result, in the next sections a detailed analysis will be made accounting for spherical harmonics up to degree and order 8.

8.4.2   Effect of Zonal Harmonics

Similarly to what happens on Earth, Mars is an oblate planet in which the largest harmonic coefficient is $C_{2,0}$, which characterizes the equatorial bulge. However, while on Earth the $C_{2,0}$ is almost 1000 times bigger than any other coefficient, in Mars the values of some of the other first terms are also considerable and only 10 to 100 times smaller than $C_{2,0}$ [50]. Hence, this section will present the effect of the $C_{2,0}$ coefficient alone and then a comparison with the rest of zonal harmonics up to 8.

8.4.2.1 $C_{2,0}$ Coefficient

To observe the impact that the addition of the $C_{2,0}$ coefficient has, two trajectories were compared: the base case, which corresponds to the most complete perturbed ER3BP orbit

(hence including polyhedral Phobos, SRP and Sun gravity) and the same model but with the inclusion of $C_{2,0}$. The result is presented in Figure 8.9.
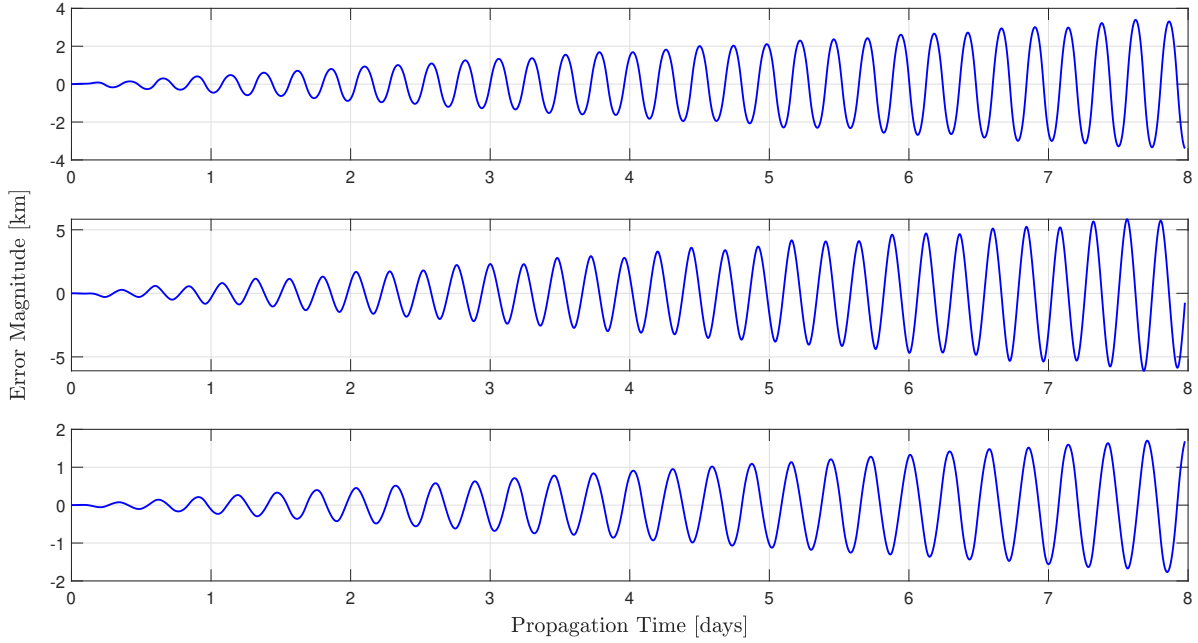
Figure 8.9: Difference in the MMX position between the complete perturbed ER3BP and the model which includes the $C_{2,0}$ coefficient. Top plot for X, middle for Y and bottom for Z.

The importance of the inclusion of spherical harmonics becomes evident since, in contrast with other perturbations such as solar radiation pressure or sun gravity, the magnitude of the variation in the spacecraft position reaches several kilometers, with the oscillations found taking place every orbital period of the spacecraft. Furthermore, the effect that $C_{2,0}$ has on the position in the Z-axis is considerable, in contrast with what happened when SRP (Figure 8.4) or Sun gravity (Figure 8.5) were added. This is an expected result, since the non-spherical gravity of Mars generates the dynamical perturbation presented in Section 5.5, which in turn affects the angular velocity and acceleration of Phobos. Changes in $\vec{\omega}$ and $\dot{\vec{\omega}}$ imply variations in the coriolis, euler and centrifugal terms of the acceleration experienced by the spacecraft, hence causing the drift observed. The magnitude of the angular velocity variation can be seen in Figure 8.10 below, where the oscillations occur every orbital period of Phobos.
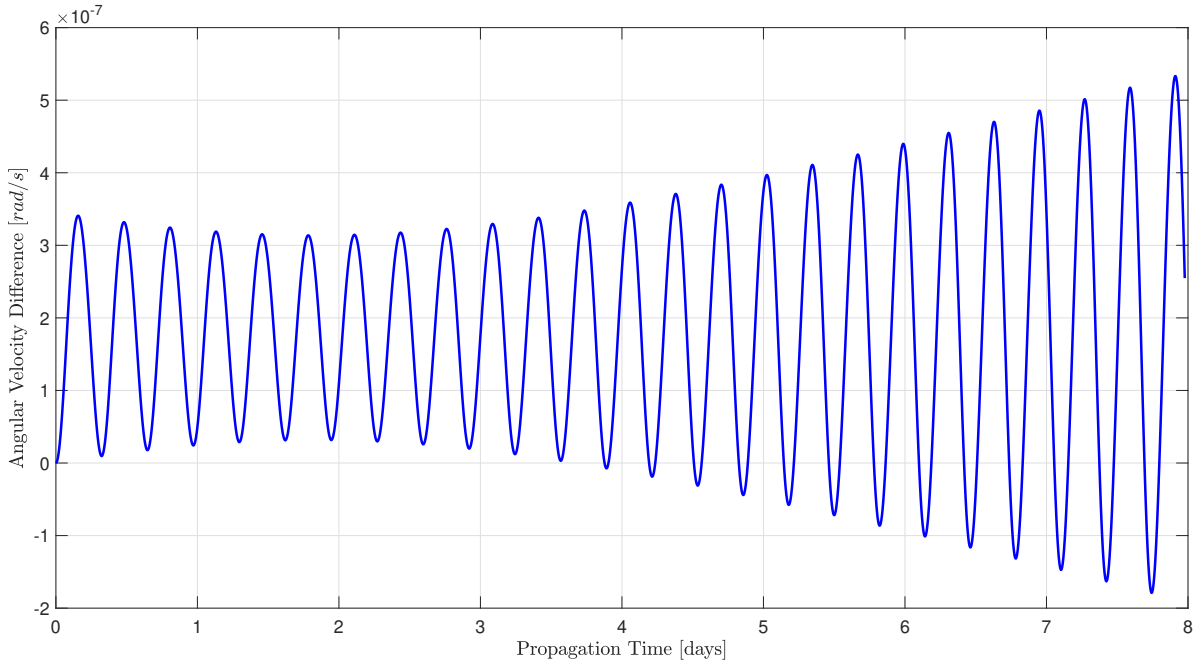
Figure 8.10: Difference in the norm of the angular velocity of Phobos between the perturbed ER3BP and the values retrieved with the introduction of $C_{2,0}$.

8.4.2.2 Rest of Zonal Harmonics

Following the analysis performed above, the rest of the zonal harmonics considered are included, reaching up to $C_{8,0}$, and the resulting orbits are compared to determine what is the individual effect of these coefficients. Doing so is not a straightforward operation due to the nature of Equation 6.3. Hence, if for example the effect of the $C_{4,0}$ coefficient wants to be studied, it is necessary to obtain the trajectory with $SH_{4,0}$ (which includes all the coefficients with order 0 and up to degree 4) and compare it to that of $SH_{3,0}$, the one immediately before. To quantify the effect that each of the zonal harmonics has, Figure 8.11 below has been obtained. Please note that, as mentioned, the values being provided represent mean difference with respect to the previous zonal harmonic coefficient and that, in the case of zonal coefficients the values for $S_{D,0}$ are all zero.
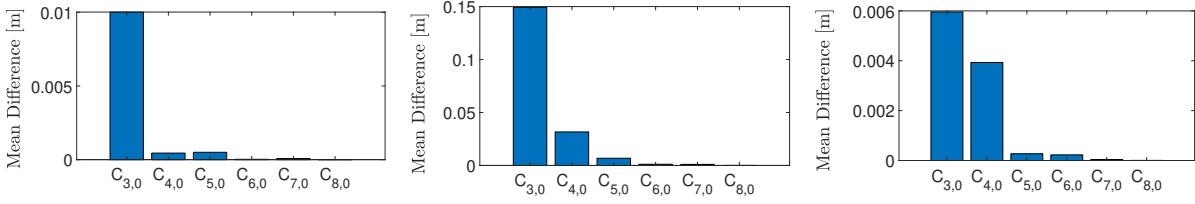
Figure 8.11: Mean difference in the MMX orbit caused by each of the zonal harmonic coefficients being considered. Left plot shows difference in the X-axis, middle in the Y and right in the Z.

The effect of each of the zonal harmonic coefficients is as expected, being most noticeable and important in the cases of $C_{3,0}$ and $C_{4,0}$. To understand how the MMX trajectory changes with respect to that obtained only considering $C_{2,0}$, Figure 8.12 below is presented.
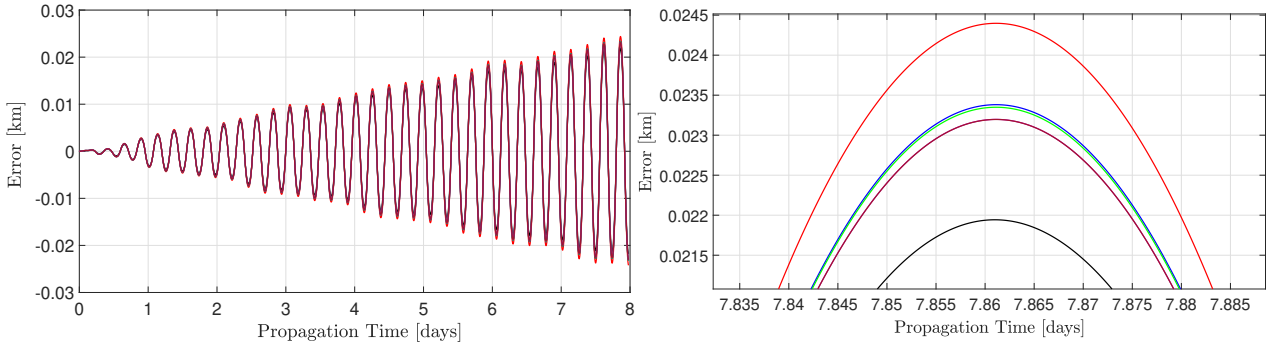
Figure 8.12: Difference in the MMX position along X in between the trajectory obtained with $C_{2,0}$ and the rest of trajectories in which bigger consecutive zonal harmonic coefficients are introduced. The right plot provides a zoomed view at the last of the oscillation peaks shown in the left graph. The color corresponds as follows: black for $C_{3,0}$, red for $C_{4,0}$, blue for $C_{5,0}$, green for $C_{6,0}$, purple for $C_{7,0}$ and brown for $C_{8,0}$.

As can be seen, the difference in between the models with respect to $C_{2,0}$ shows the same type of oscillatory behaviour, with the magnitudes experiencing a greater divergence at the peaks of the oscillations. This is a reasonable result since the mentioned oscillation peaks correspond MMX orbits and, in particular, to the apogee of the epicycles, where differences in velocity have a more visible effect on the position of the spacecraft. For the components in the Y-direction, the behaviour found is the same as the one described by Figure 8.12, so it will not be reproduced again. For the case of the Z-axis it does change as can be seen in Figure 8.13, although the magnitude of these variations is very small. Values for the maximum differences between the $C_{2,0}$ trajectory and the rest are provided in Table 8.3.
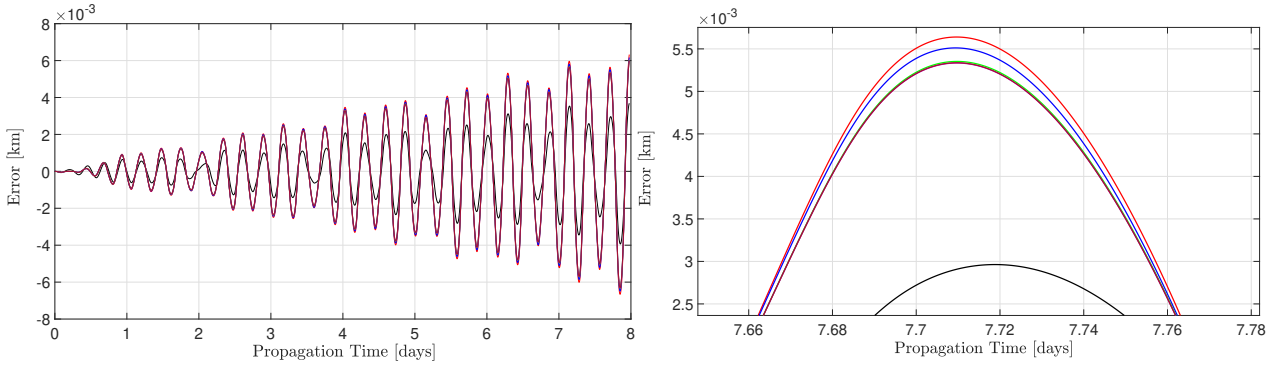
Figure 8.13: Error along Z in between the trajectory obtained with $C_{2,0}$ and the rest of orbits. The right plot provides a zoomed view at the last of the oscillation peaks shown in the left graph. The color corresponds to: black for $C_{3,0}$, red for $C_{4,0}$, blue for $C_{5,0}$, green for $C_{6,0}$, purple for $C_{7,0}$ and brown for $C_{8,0}$.

	$C_{3,0}$	$C_{4,0}$	$C_{5,0}$	$C_{6,0}$	$C_{7,0}$	$C_{8,0}$
ΔX_{max} [m]	21.94	24.40	23.38	23.35	23.21	23.22
ΔY_{max} [m]	37.51	41.79	40.05	39.99	39.73	39.74
ΔZ_{max} [m]	2.96	5.64	5.51	5.35	5.33	5.34

Table 8.3: Maximum differences in the position components of the MMX spacecraft between the orbit taken as reference which was computed using $C_{2,0}$ and the orbits obtained with the inclusion of upper zonal harmonics coefficients.

Hence, from the analysis carried out in this section it is clear that the major effects are caused by the coefficients $C_{3,0}$ and $C_{4,0}$, although this last one appears to overestimate the changes in the X and Y components, as shown in Table 8.3. After that, the rest of the coefficients have a small effect and convergence is eventually reached after $C_{7,0}$.

8.4.2.3   Sectorial Coefficients

Following the analysis carried out in the previous section, it is also possible to study the effect that sectorial coefficients have on the MMX trajectory. In particular, these coefficients represent bands of longitude and are obtained whenever the degree and order are the same. In this case, both C and S coefficients are present. To find the effect that, for example, sectorial coefficients of degree and order 3 have, the procedure followed has been to determine the MMX orbit using $SH_{3,3}$ and then find the difference with the trajectory obtained using $SH_{3,2}$, since this yields the effect of $C_{3,3}$ and $S_{3,3}$. Doing so for sectorial coefficients up to degree and order 8 yields Figure 8.14 below.

Figure 8.14: Mean difference caused by each of the sectorial coefficients being analyzed in the MMX trajectory. Left plot shows difference in the X-axis, middle in the Y and right in the Z.

As can be appreciated, the zonal coefficients of degrees and orders 2 and 3 present very important effects that must be taken into account, with those of degree and order 4 also appearing relevant. To quantify the magnitude of their effects on the MMX orbit, Table 8.4 has been obtained, where the maximum position difference introduced by each of the coefficients during a propagation time spanning 8 days (25 orbital periods of Phobos) has been computed.

	$\textbf{SH}_{2,2}$	$\textbf{SH}_{3,3}$	$\textbf{SH}_{4,4}$	$\textbf{SH}_{5,5}$	$\textbf{SH}_{6,6}$	$\textbf{SH}_{7,7}$	$\textbf{SH}_{8,8}$
ΔX_{max} [m]	109.42	182.61	20.68	2.54	1.24	0.26	0.021
ΔY_{max} [m]	190.07	316.36	35.95	4.37	2.13	0.45	0.037
ΔZ_{max} [m]	27.45	43.52	4.80	0.59	0.29	0.06	0.0047

Table 8.4: Maximum differences in the position components of the MMX spacecraft introduced by the sectorial coefficients being considered.

As provided in Table 8.4, the sectorial coefficients of degree and order 2 and 3 are responsible for important variations in the spacecraft position. This is expected, since looking at the values of the GMM3 model these sectorial coefficients are only 10 orders of magnitude smaller than $C_{2,0}$.

8.4.3 Tesseral Coefficients

Finally, the analysis can be completed by studying the tesseral coefficients of the GMM3 model, which correspond to specific regions of Mars. To that end, a similar analysis as the one conducted in the previous section for the sectorial coefficients can be carried out. Figure 8.15 below shows the mean of the position difference introduced by these coefficients.
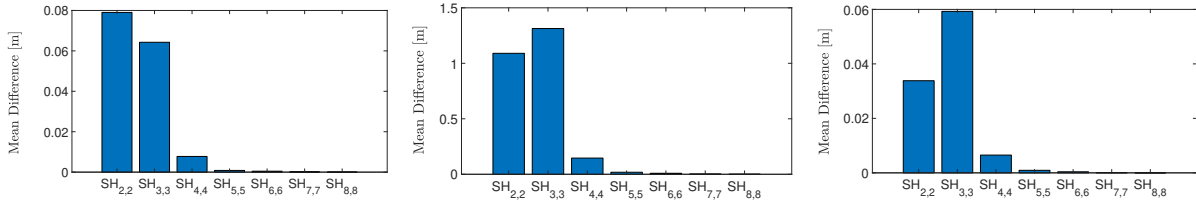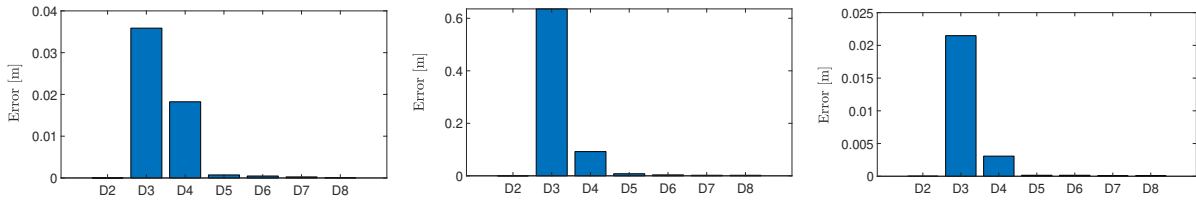
Figure 8.15: Mean difference caused by each of the tesseral coefficients being considered. Left plot shows difference in the X-axis, middle in the Y and right in the Z. Each of the columns in the plots correspond to the combined effect of the tesseral coefficients of a certain degree, specified as D.

Once again, it is visible that tesseral coefficients up to at least degree and order 4 should be taken into account. It is worth noting that the effect of $C_{2,1}$ and $S_{2,1}$ is of the order of 10^{-3} meters. Furthermore, the maximum position differences introduced by tesseral coefficients is found in Table 8.5 below. Please note that, as for Figure 8.15, the values represent the effect of all the tesseral coefficients that have the same degree. Hence, a column corresponding to $D4$ gives information about the effect caused by $C_{4,1}$, $C_{4,2}$, $C_{4,3}$ and the corresponding S coefficients.

	$D2$	$D3$	$D4$	$D5$	$D6$	$D7$	$D8$
ΔX_{max} [m]	0.00145	84.538	17.0326	1.162	0.293	0.320	0.268
ΔY_{max} [m]	0.00262	145.514	31.393	2.136	0.634	0.572	0.476
ΔZ_{max} [m]	0.000203	19.886	1.598	0.212	0.175	0.0579	0.0564

Table 8.5: Maximum differences in the position components of the MMX spacecraft introduced by the tesseral coefficients being considered, ordered by degree groups. Values have been rounded up to three significant figures after the decimal point.

8.5   Sensitivity to Injection Errors

In order for the MMX spacecraft to start orbiting Phobos, an injection maneuver will have to be performed. Ideally, such maneuver should enable the spacecraft to start orbiting the moon with the initial conditions provided in Table 5.3 but, in reality, small injection errors appear, affecting the position and/or the velocity of the spacecraft. For the case of the MMX mission, Nicola Baresi provided values for the accuracy desired, specifying that the maximum injection error in position should be of 50 meters. In the case of the velocity, an error of up to 3 cm/s is acceptable.

Therefore, an analysis was carried out to determine the effect that this injection errors

would have on the MMX orbit, with spherical harmonics being considered up to degree and order 8. No information was available regarding the injection azimuth and elevation angles, a simple approach was taken: injection errors were introduced one by one assuming they were found only in one axis of the LVLH frame. The twelve cases considered are found in Table 8.6, together with the value of the position difference with respect to the nominal trajectory, that is, the one in which no injections errors are present.

	Injection Error	Error Norm at t_f [km]
Case 1	+ 50 m in X	17.8123
Case 2	- 50 m in X	18.2195
Case 3	+ 50 m in Y	0.1106
Case 4	- 50 m in Y	0.1137
Case 5	+ 50 m in Z	2.1456
Case 6	- 50 m in Z	2.1638
Case 7	+ 3 cm/s in X	0.2692
Case 8	- 3cm/s in X	0.2400
Case 9	+ 3 cm/s in Y	46.5881
Case 10	- 3cm/s in Y	47.1144
Case 11	+ 3cm/s in Z	0.7265
Case 12	- 3cm/s in Z	0.6934

Table 8.6: Summary of cases analyzed regarding the introduction of injection errors. Values for the norm of the position difference at the end of the propagation with respect to the trajectory with no injection errors are also given. The propagation time was considered to be 25 orbits of Phobos around Mars.

The results retrieved show that whenever injection errors are found in the X-axis position components or in the Y-axis velocity components the trajectory of the spacecraft is severely modified. For Cases 1 and 2, the explanation behind such sensitivity can be found in the fact that X is the radial direction to Mars in the LVLH frame, so changes here imply modifying the Mars-MMX radial separation and hence the value of the gravity acceleration exerted by the planet. With respect to cases 9 and 10, the Y direction of the LVLH frame corresponds to the direction in which the azimuthal orbital velocity of Phobos is found. In addition, the initial position of the MMX spacecraft corresponds to the perigee of the epicycle, and hence this injection error in the velocity acts as a perigee kick, provoking the apogee of the orbit to drift away from the nominal value and causing an error which then propagates. In Figure 8.16 below this can be clearly seen by looking at the beginning of the propagation time and observing how the Y position coordinate diverges. After one spacecraft orbital period the error in Y is already 3.14 km. Similarly, the different epicycle drift along the Y axis is clearly

appreciable in Figure 8.17.
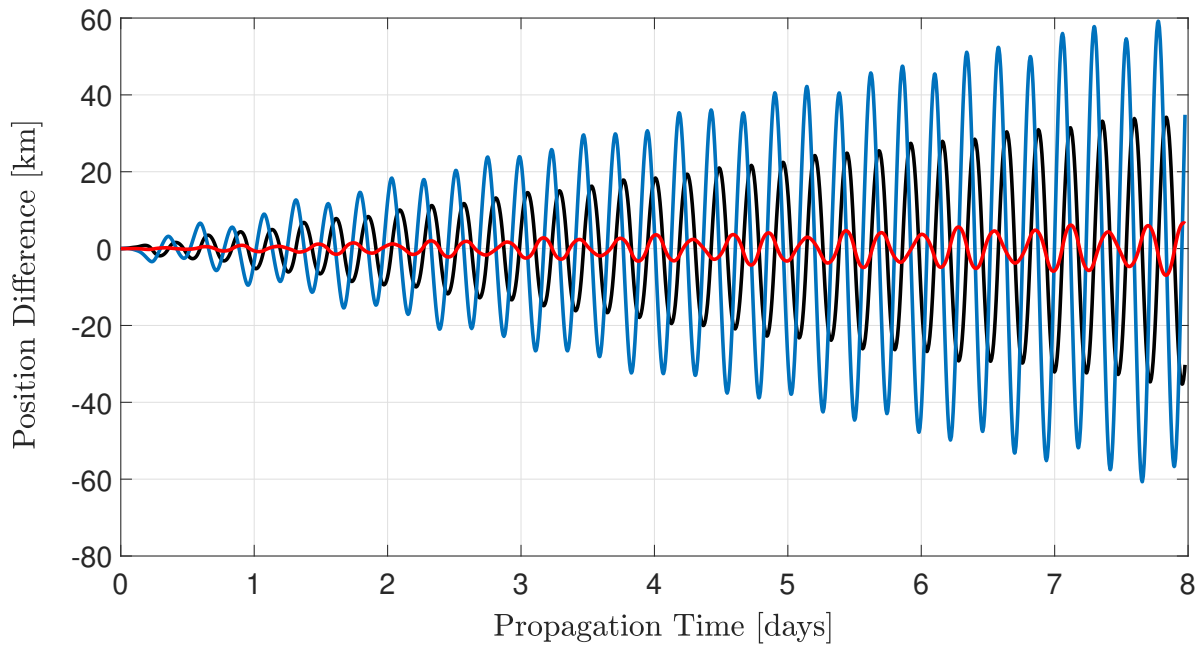
Figure 8.16: Position difference in each component caused by an injection error of 3 cm/s in the Y_{LVLH} direction. The black line is position error in X_{LVLH}, the blue line in Y_{LVLH} and the red line in Z_{LVLH}.
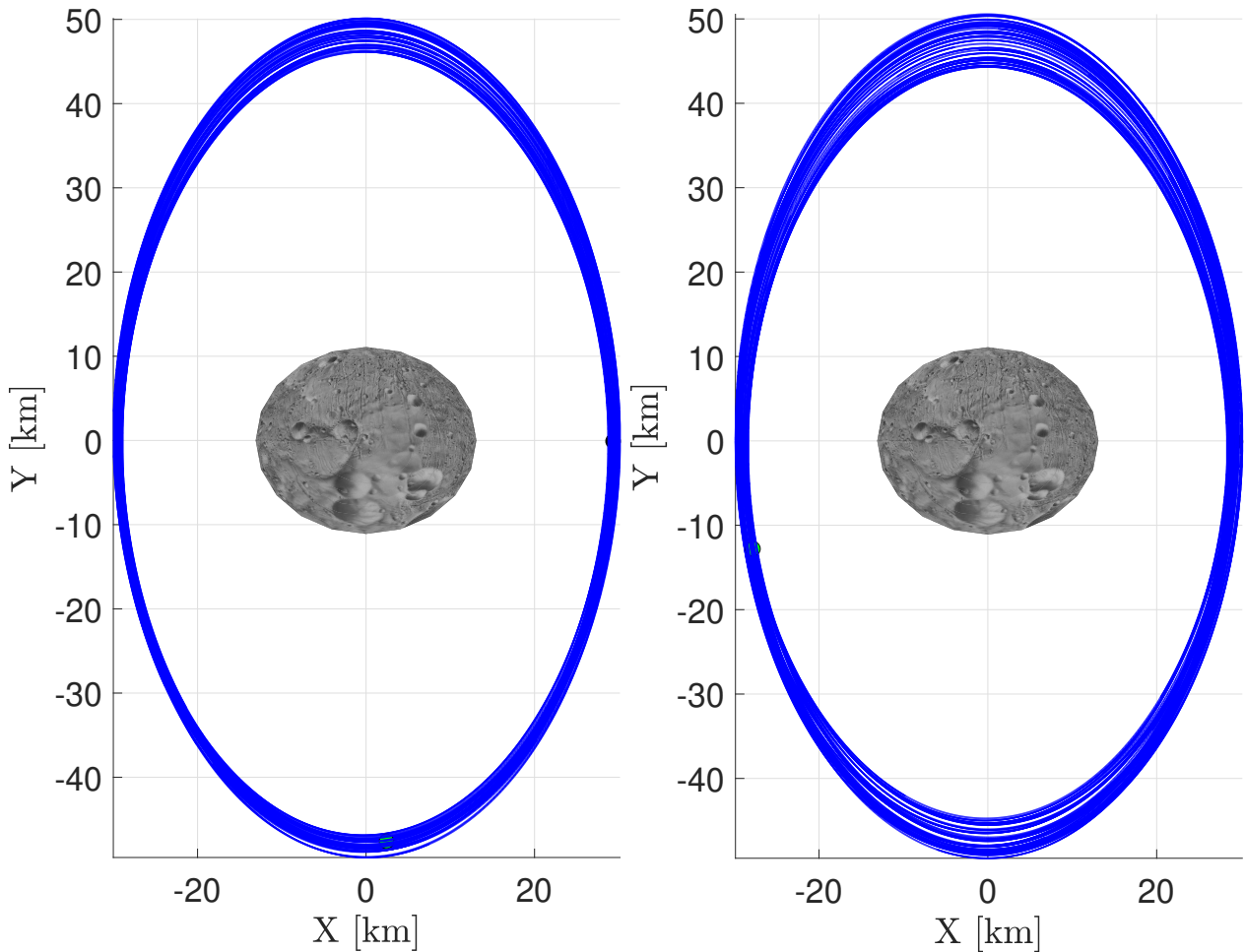
Figure 8.17: View from the Z_{LVLH} axis of the orbit obtained with nominal initial conditions (left) and of the orbit which included a 3cm/s injection error in the Y-component of the velocity (right).

Despite the differences in some of the analyzed cases being considerable, none of the orbits presented in Table 8.6 failed after 25 orbital periods of Phobos around Mars. The error in the spacecraft velocities for the cases in which the injection errors caused greater differences (cases 1,2,9 and 10) was also obtained, and is shown in Figures 8.18 and 8.19 below.
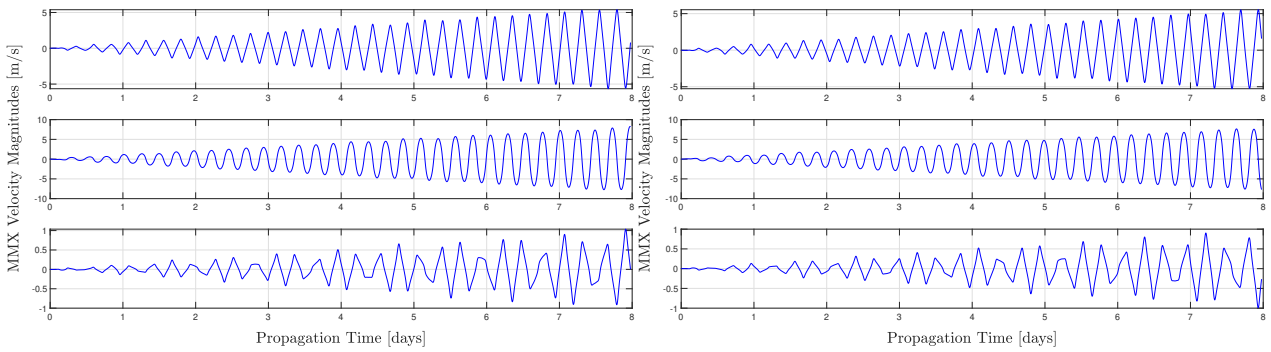
Figure 8.18: Error in the spacecraft velocities with respect to the trajectory with nominal initial conditions. Left plot for Case 1 and right for Case 2.
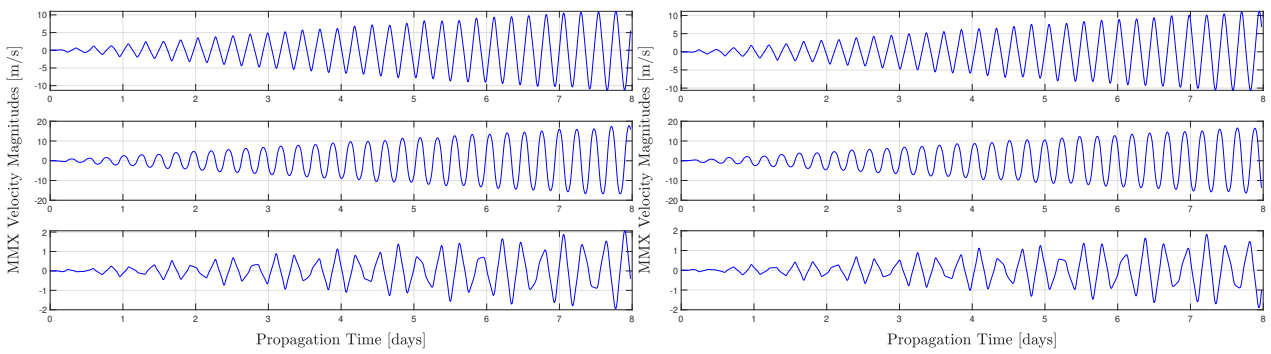
Figure 8.19: Error in the spacecraft velocities with respect to the trajectory with nominal initial conditions. Left plot for Case 9 and right for Case 10.

Although the velocity components experience considerable differences, there is no clear sign of a possible escape or crash into Phobos, since there is no sudden change in the velocity. This was verified by propagating the QSO with a 3 cm/s error in the V_y component for a total of 125 orbital periods of Phobos arounds Mars, which corresponds to almost 48 days. The orbit survived as can be seen in Figure 8.20, proving that this QSO is robust and well-suited for long term operations around Phobos.
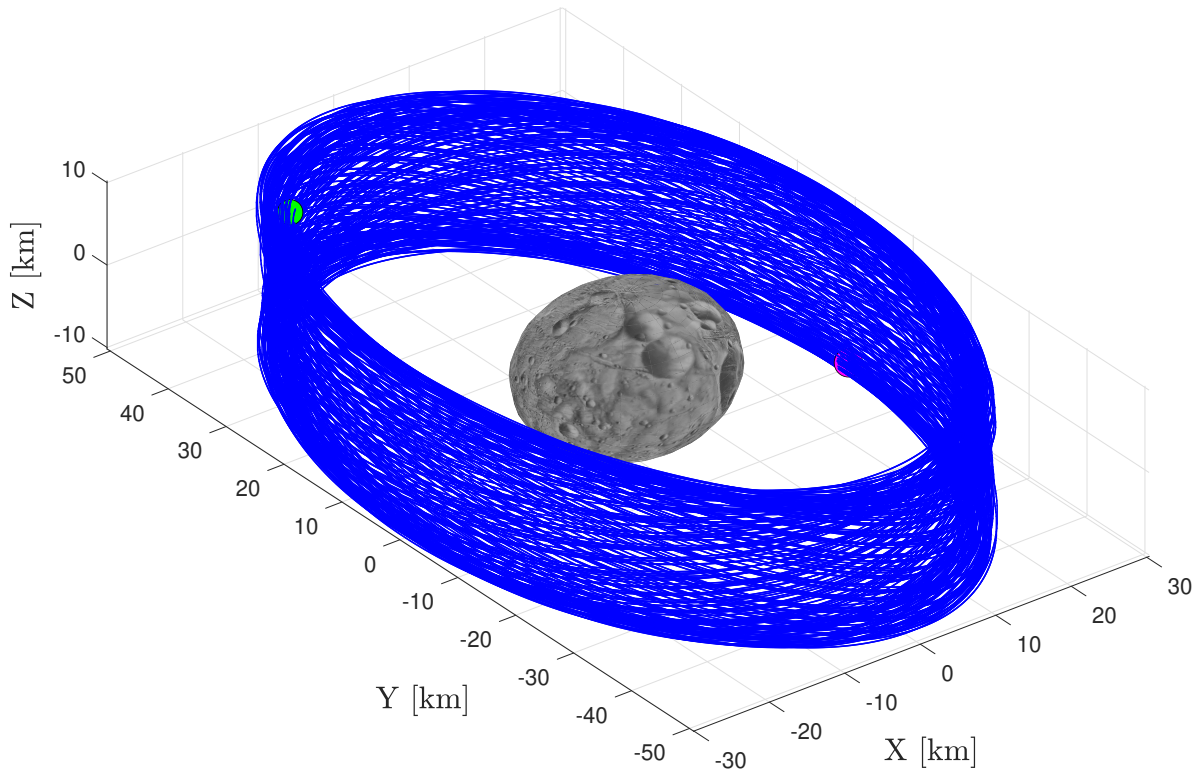
Figure 8.20: 3D plot of the MMX trajectory for the 30×50 km QSO subjected to an injection error of 3 cm/s in V_y. The propagation time spans 125 orbital periods of Phobos around Mars. The magenta and green circular markers represent initial and final position of the spacecraft respectively.

9.1 Summary and Results Overview

One of the many unanswered questions regarding the Solar System and its bodies is posed by Phobos and Deimos, the two moons of Mars. In particular, understanding their origin and evolution presents a difficult problem, since the the two main theories being considered have aspects which scientists have not been able to explain yet.

Solving the uncertainties related to this moons could be possible by means of a robotic exploration mission. As a result, the Japanese Space Agency is developing the so-called MMX project to study both moons and retrieve a sample from Phobos. Doing so implies that the spacecraft will first have to orbit around the moon, and this poses a technical challenge due to the rich dynamical environment found.

Previous studies have shown that it is possible to orbit Phobos using Quasi-Satellite Orbits, and that the perturbations which have a bigger effect on the spacecraft motion are the non-uniform gravity field of Mars, centrifugal forces and the gravitational field of Phobos. This thesis has therefore aimed to the study of the impact that these perturbations would have.

97

To that end, a perturbed relative motion problem has been considered. An orbital propagator has been developed in the MATLAB environment with the objective of integrating the equations of motion and detailed models have been used to introduce the perturbations. In particular, the gravity of Mars is taken into account by means of a spherical harmonics model which can reach degree and order 80, a constant density polyhedron has been used for Phobos and solar radiation pressure and sun gravity have been taken into account.

Before carrying out the analysis of the effect of the perturbations, the propagator developed has been verified by using several test cases. In particular, *AGEX*, a propagator developed by Lamberto Dell'Elce, has been used to compare the circular restricted three body problem, the elliptical restricted three body problem, the correct introduction of a polyhedral Phobos and the models for solar radiation pressure and gravitational attraction of the Sun. For the validation of the spherical harmonic model NASA's SPICE software has been used.

Once it had been demostrated that the MMX High Fidelity Propagator yielded accurate results, the analysis has been carried out for a low-altitude 30×50 km QSO. Results have shown that the gravitational field of Phobos is very important, and hence a precise modelling has to be used. Furthermore, after a thorough analysis of the spherical harmonics of Mars, it has been determined that the major effects on the MMX orbit are caused by the coefficients up to degree and order 4, and that in order to have a high precision propagator coefficients up to degree and order 8 must be considered. In contrast, the analysis has proven that the effects of solar radiation pressure and sun's gravity are very small.

Finally, a study has been carried out to determine the effect that injection errors could have on the stability and life of the orbit. Results have shown that the greater divergences are created by injection errors in the velocity component directed along the Y axis of the Local Vertical Local Horizontal frame. Also, injection errors in the position along X cause significant divergence. In any case, the V_y injection error case has been propagated for 48 days and no failure event has occurred, showing that the 30×50 km QSO is robust.

9.2 Future Work

This thesis performs a detailed analysis the perturbations affecting a 30 × 50 km QSO around Phobos. The results obtained open a wide variety of options and improvements which can be studied in the future. Examples of these are:

- In this work, the eccentricity of Phobos is considered to be constant and equal to 0.0151. Future works should perform a profound analysis of the effect of eccentricity variations, since it appears to be an important parameter affecting the spacecraft trajectory.

- Future models could introduce more perturbations such as the gravitational attraction of Jupiter or the Mars radiation pressure (MRP). Furthermore, a non-keplerian orbit of Mars around the Sun could be considered to obtain more accurate values for SRP and the Sun's gravity.

- The injection error analysis carried out in this thesis should be extended to more complicated and complete cases.

- Future works could also introduce a Monte-Carlo analysis of different uncertainties such as eccentricity, spacecraft ballistic properties and injection errors.

As was mentioned previously in Section 7.5, this Appendix will provide a brief description of the SPICE software, as well as the main functions and kernels used in the validation of the spherical harmonics model of Mars. For further information, the reader is referred to the NAIF JPL webpage and to the SPICE documents, available in references [51] and [52] respectively.

A.1   The SPICE software

SPICE is a software developed by the Navigation and Ancillary Information Facility (NAIF), a team established at the Jet Propulsion Laboratory (JPL), and was created with the objective of enabling scientists and engineers to design and plan the operations of space missions. The concept is based on the usage of what is known as ancillary data, which is stored in the so-called *kernel* files with which SPICE works [53].

The content of the mentioned files is no other than information regarding positions, velocities, orientations, physical parameters, reference systems and time conversions. The acronym of the software is directly related to the type of *kernel* that can be found, as those files provide information regarding **S**pacecrafts, **P**lanets, **I**nstruments, **C**ameras and **E**vents. Figure A.1 below presents an schematic summary of the types of *kernels* available and the information they contain.
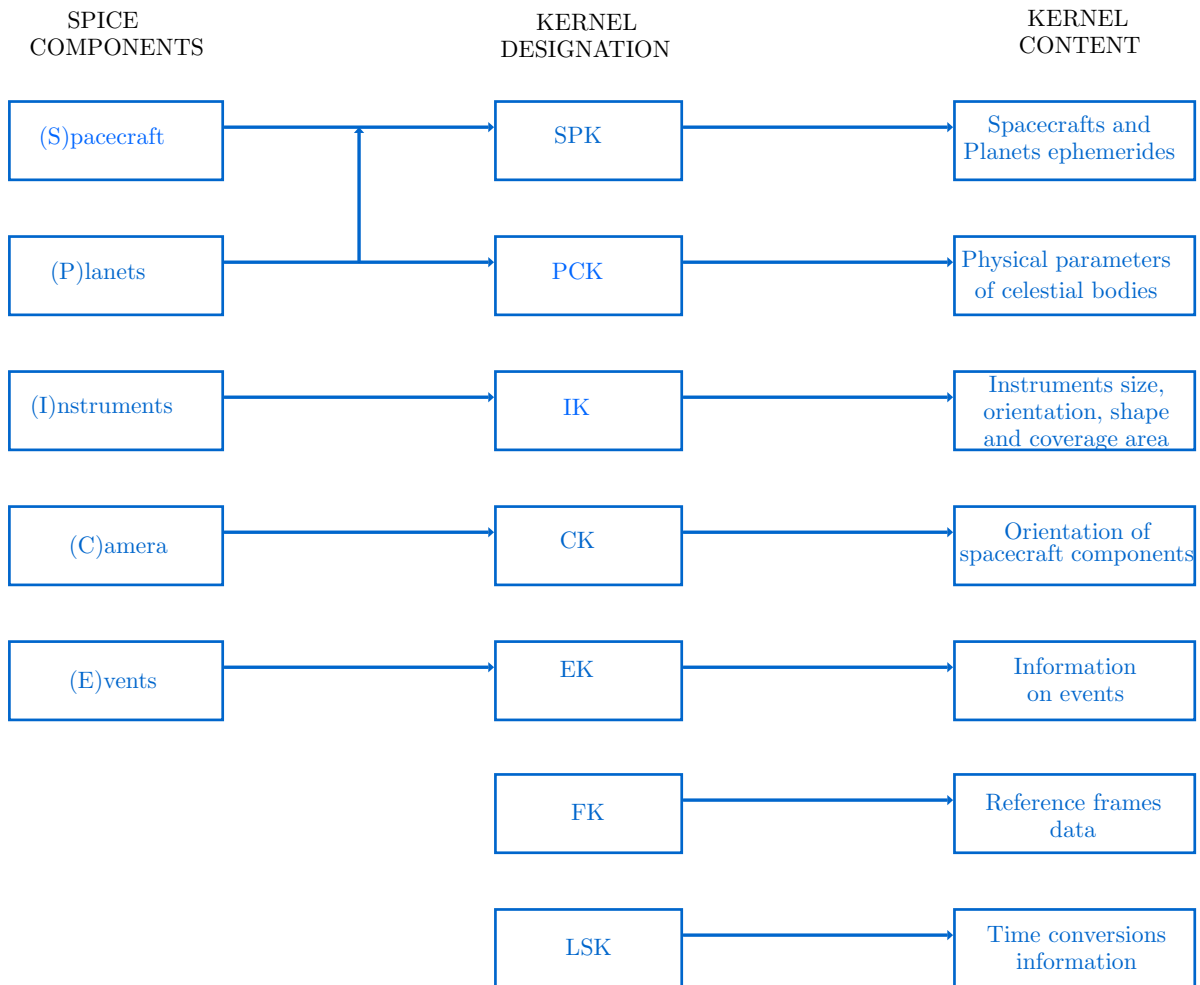
Figure A.1: Summary of the different types of existing kernels and the information that each one contains.

Both the SPICE software and the *kernel* files are free and can be downloaded from the corresponding NAIF web pages, found in references [54] and [55] respectively. For the MATLAB environment the software is known as the *Mice* Toolkit.

A.2   List of Kernels

To carry out the validation of the spherical harmonics of Mars, the following *kernel* files were used:

- *de430 bsp* : Planet ephemeris kernel containing position and velocity of celestial bodies.

- *naif0012.tls.pc* : Leapseconds kernel with information required for time conversions.

- *pck00010.tpc* : Kernel containing the physical parameters of celestial bodies.

- *gm de431.tpc* : Kernel containing gravitational information.

- *mar097.bsp* : Mars satellites kernel

A.3 List of SPICE functions

To use the files listed above, several SPICE functions had to be used. They are listed here together with a brief description of the function itself.

- *cspice bodvrd*: retrieves parameters from an specified body, such as radius, gravitational parameter, pole right ascension and declination etc.

- *cspice furnsh*: loads the downloaded kernel files into the so-called kernel pool, so that the mentioned kernels can be accesed later in the code.

- *cspice oscelt*: computes the osculating orbital elements that correspond to the state vector provided as input.

- *cspice pxform*: yields the matrix that transforms vectors from an specified frame to another at the defined epoch.

- *cspice spkezr*: retrieves the state vector of an specified target body with respect to an observing body at an specified epoch.

- *cspice str2et*: converts an specified epoch to seconds TDB past the J2000 epoch.

- *cspice unload*: unloads the specified kernel file from the kernel pool to avoid saturation.

BIBLIOGRAPHY

[1] H. Hussmann, F. Sohl., and J. Oberst, *4.2.2 Basic data of planetary bodies*. Berlin, Heidelberg: Springer Berlin Heidelberg, 2009, pp. 208–229. [Online]. Available: https://doi.org/10.1007/978-3-540-88055-4_15

[2] NASA, *Phobos: Facts and Figures*, 2019 (accessed July 24, 2019). [Online]. Available: https://web.archive.org/web/20131019162634/http://solarsystem.nasa.gov/planets/profile.cfm?Object=Mar_Phobos&Display=Facts

[3] NASA, *Deimos: Facts and Figures*, 2019 (accessed July 24, 2019). [Online]. Available: https://web.archive.org/web/20131019172735/http://solarsystem.nasa.gov/planets/profile.cfm?Object=Mar_Deimos&Display=Facts

[4] N. T. Redd, *Phobos: Facts About the Doomed Martian Moon*, 2017 (accessed July 24, 2019). [Online]. Available: https://www.space.com/20346-phobos-moon.html

[5] Y. Toukaku, *JAXA Space Science Program and International Collaboration*, 2018 (accessed July 25, 2019). [Online]. Available: http://www.essc.esf.org/fileadmin/user_upload/essc/ISAS_Program_Overview_May-2018.pdf

[6] H. D. Curtis, *Orbital Mechanics for Engineering Students*, 3rd ed. Elsevier, 2014.

[7] NASA Science, *Mars Moons*, 2017 (accessed July 24, 2019). [Online]. Available: https://solarsystem.nasa.gov/moons/mars-moons/in-depth/

[8] T. Imada, *Constructing the model of the MMX spacecraft*, 2018 (accessed July 28, 2019). [Online]. Available: http://mmx-news.isas.jaxa.jp/?p=492&lang=en

[9] P. Rosenblatt, "The origin of the Martian moons revisited," *Astronomy and Astrophysics Review*, vol. 19, pp. 1–26, 12 2011.

[10] M. Zamaro and J. Biggs, "Natural motion around the Martian moon Phobos: the dynamical substitutes of the Libration Point Orbits in an elliptic three-body problem

with gravity harmonics," *Celestial Mechanics and Dynamical Astronomy*, vol. 122, pp. 263–302, 2015.

[11] A. Genova, *Mars Gravity Field: GMM3*, 2019 (accessed August 04, 2019). [Online]. Available: https://pgda.gsfc.nasa.gov/products/57

[12] R. Hollingham, *V2: The Nazi rocket that launched the space age*, 2014 (accessed July 24, 2019). [Online]. Available: http://www.bbc.com/future/story/20140905-the-nazis-space-age-rocket

[13] NASA, *Solar System Exploration: Mars*, 2014 (accessed July 24, 2019). [Online]. Available: https://solarsystem.nasa.gov/planets/mars/in-depth/

[14] S. L. Murchie, P. C. Thomas, A. S. Rivkin, and N. L. Chabot, "Phobos and Deimos," *Asteroids*, vol. 4, pp. XX–YY, 2015.

[15] NASA, *In Depth: Phobos*, 2019 (accessed July 24, 2019). [Online]. Available: https://solarsystem.nasa.gov/moons/mars-moons/phobos/in-depth/

[16] T. C. Duxbury, A. V. Zakharov, H. Hoffmann, and E. A. Guinness, "Spacecraft exploration of Phobos and Deimos," *Planetary and Space Science*, vol. 102, pp. 9 – 17, 2014.

[17] M. Ya. Marov, V. S. Avduevsky, E. L. Akim, T. M. Eneev, R. S. Kremnev, S. D. Kulikov, K. M. Pichkhadze, G. A. Popov, and G. N. Rogovsky, "Phobos-grunt: Russian sample return mission," *Advances in Space Research*, vol. 33, no. 12, pp. 2276 – 2280, 2004.

[18] M. Wall, *Failed Russian Mars Probe Crashes Into Pacific Ocean: Reports*, 2012 (accessed July 24, 2019). [Online]. Available: https://www.space.com/14242-russia-spacecraft-phobos-grunt-crash-earth.html

[19] S. Campagnola, C. Hong Yam, Y. Tsuda, N. Ogawa, and Y. Kawakatsu, "Mission analysis for the Martian Moons Explorer (MMX) mission," *Acta Astronautica*, vol. 146, pp. 409 – 417, 2018.

[20] JAXA, *MMX: Science*, 2018 (accessed July 28, 2019). [Online]. Available: http://mmx.isas.jaxa.jp/en/science/

[21] R. Canup and J. Salmon, "Origin of Phobos and Deimos by the impact of a Vesta-to-Ceres sized body with Mars," *Science Advances*, vol. 4, no. 4, 2018.

[22] R. A. Mase, "Update to Mars Coordinate Frame Definitions," Jet Propulsion Laboratory, California Institute of Technology, Pasadena, USA, 20060034233, Tech. Rep., January 1999.

[23] L. Lin, Y. Zhao, Z. Wei, W. Yan-rong, and W. Jia-song, "Coordinate additional perturbations to mars orbiters and choice of corresponding coordinate system," *Chinese Astronomy and Astrophysics*, vol. 35, pp. 188–198, 04 2011.

[24] United States Naval Observatory and Her Majesty's Nautical Almanac Office, *Astronomical Constants*, 2018 (accessed April 24, 2020). [Online]. Available: http://asa.hmnao.com/static/files/2018/Astronomical_Constants_2018.pdf

[25] P. K. Seidelmann, B. A. Archinal, M. F. A'hearn, A. Conrad, G. J. Consolmagno, D. Hestroffer, J. L. Hilton, G. A. Krasinsky, G. Neumann, J. Oberst, P. Stooke, E. F. Tedesco, D. J. Tholen, P. C. Thomas, and I. P. Williams, "Report of the IAU/IAG Working Group on cartographic coordinates and rotational elements: 2006," *Celestial Mechanics and Dynamical Astronomy*, vol. 98, pp. 155–180, 2007.

[26] E. Joffre, M. Zamaro, N. Silva, A. Marcos, and P. Simplício, "Trajectory Design and Guidance for Landing on Phobos," *Acta Astronautica*, vol. 151, pp. 389 – 400, 2018. [Online]. Available: http://www.sciencedirect.com/science/article/pii/S0094576517303326

[27] G. Franzini and M. Innocenti, "Relative motion equations in the local-vertical local-horizon frame for rendezvous in lunar orbits," 08 2017.

[28] H. Schaub and J. L. Junkins, *Analytical Mechanics of Space Systems*, 2nd ed. American Institute of Aeronautics and Astronautics, 2009.

[29] N. Baresi, L. Dell'Elce, J. Cardoso dos Santos, and Y. Kawakatsu, "Long-term evolution of mid-altitude quasi-satellite orbits," *Nonlinear Dynamics*, vol. 99, p. 2743–2763, 01 2020. [Online]. Available: https://link.springer.com/article/10.1007/s11071-019-05344-4

[30] D. J. Scheeres and F. Marzari, "Spacecraft dynamics in the vicinity of a comet," *Journal of the Astronautical Sciences*, vol. 50, pp. 35–52, 01 2002.

[31] A. I. Veris, *Practical Astrodynamics*, 1st ed. Springer, 2018.

[32] G. Balmino, B. Moynot, and N. Valès, "Gravity field model of mars in spherical harmonics up to degree and order eighteen," *Journal of Geophysical Research:*

Solid Earth, vol. 87, no. B12, pp. 9735–9746, 1982. [Online]. Available: https://agupubs.onlinelibrary.wiley.com/doi/abs/10.1029/JB087iB12p09735

[33] A. Genova, S. Goossens, F. G. Lemoine, E. Mazarico, G. A. Neumann, D. E. Smith, and M. T. Zuber, "Seasonal and static gravity field of Mars from MGS, Mars Odyssey and MRO radio science," *Icarus*, vol. 272, pp. 228 – 245, 2016. [Online]. Available: http://www.sciencedirect.com/science/article/pii/S0019103516001287

[34] L. E. Cunningham, "On the computation of the spherical harmonic terms needed during the numerical integration of the orbital motion of an artificial satellite," *Celestial Mechanics*, vol. 2, pp. 207–216, 1969.

[35] A. Tewari, *Optimal Space Flight Navigation*, 1st ed. Birkhäuser, 2019.

[36] R. Werner and D. J. Scheeres, "Exterior gravitation of a polyhedron derived and compared with harmonic and mascon gravitation representations of asteroid 4769 Castalia," *Celestial Mechanics and Dynamical Astronomy*, vol. 65, p. 313–344, 1996.

[37] Y. Yu, *Orbital Dynamics in the Gravitational Field of Small Bodies*, 1st ed. Springer, 2016.

[38] L. Dell'Elce, N. Baresi, S.P. Naidu, L.A.M Benner, and D.J. Scheeres, "Numerical investigation of the dynamical environment of 65803 Didymos," *Advances in Space Research*, vol. 59, pp. 1304–1320, 03 2017.

[39] X. Shi, K. Willner, J. Oberst, J. Ping, and S. Ye, "Working models for the gravitational field of Phobos," *Science China Physics, Mechanics and Astronomy*, vol. 55, no. 2, pp. 358–364, Feb 2012. [Online]. Available: https://doi.org/10.1007/s11433-011-4606-4

[40] J. K. Miller and T.C. Duxbury, "The Phobos Gravity Field and Internal Properties," *Television Investigations of Phobos*, 10 1990.

[41] D. J. Scheeres, *Orbital Motion in Strongly Perturbed Environments: Applications to Asteroid, Comet and Planetary Satellite Orbiters*, 1st ed. Springer, 2012.

[42] CJ. Rodriguez-Solano, U. Hugentobler, and P. Steigenberger, "Adjustable box-wing model for solar radiation pressure impacting GPS satellites," *Advances in Space Research*, vol. 49, pp. 1113–1128, 2012.

[43] J. W. McMahon and D. J. Scheeres, "New Solar Radiation Pressure Force Model for Navigation," *Journal of Guidance, Control and Dynamics*, vol. 33(5), pp. 1418–1428, 2010.

[44] D. M. Lucchesi, "Reassessment of the error modelling of non-gravitational perturbations on LAGEOS II and their impact in the Lense-Thirring determination. Part I," *Planetary and Space Science*, vol. 49, pp. 447–463, 2001.

[45] A. Buis, *Milankovitch (Orbital) Cycles and Their Role in Earth's Climate* , 2020 (accessed May 20, 2020). [Online]. Available: https://climate.nasa.gov/news/2948/milankovitch-orbital-cycles-and-their-role-in-earths-climate/

[46] D. A. Vallado, *Fundamentals of Astrodynamics and Applications*, 4th ed. Microcosm Press, 2013.

[47] J. Mc. Mahon and D. J. Scheeres, "Dynamic Limits on Planar Libration-Orbit Coupling Around an Oblate Primary," *Celestial Mechanics and Dynamical Astronomy*, vol. 115, 05 2012.

[48] J. Clarke, "Eclipses on Mars," *Publication of the Pomona College Astronomical Society*, vol. 8, pp. 10–12, 01 1923.

[49] P. Gil and J. Schwartz, "Simulations of Quasi-Satellite Orbits Around Phobos," *Journal of Guidance Control and Dynamics*, vol. 33, pp. 901–914, 05 2010.

[50] X. Lui, H. Baoyin, and X. Ma, "Five Special Types of Orbits Around Mars," *Journal of Guidance, Control and Dynamics*, vol. 33, pp. 1294–1301, 08 2010.

[51] NAIF, *SPICE Required Reading Documents*, 2019 (accessed August 01, 2019). [Online]. Available: https://naif.jpl.nasa.gov/pub/naif/toolkit_docs/C/req/index.html

[52] NAIF, *The SPICE Toolkit*, 2019 (accessed August 01, 2019). [Online]. Available: https://naif.jpl.nasa.gov/naif/toolkit.html

[53] ——, *The SPICE Concept*, 2019 (accessed August 01, 2019). [Online]. Available: https://naif.jpl.nasa.gov/naif/about.html

[54] ——, *Toolkit: MATLAB*, 2019 (accessed August 01, 2019). [Online]. Available: https://naif.jpl.nasa.gov/naif/toolkit_MATLAB.html

[55] JPL-NAIF, *Planetary Data System: Navigation Node*, 2019 (accessed August 01, 2019). [Online]. Available: https://naif.jpl.nasa.gov/pub/naif/generic_kernels/